Università Politecnica delle Marche
Scuola di Dottorato di Ricerca in Scienze dell'Ingegneria
Corso di Dottorato in Ingegneria Industriale

Perpendicularly magnetized synthetic antiferromagnets for flexible spintronic and biomedical applications

Ph.D. Dissertation of:

Mariam Hassan

Supervisor:

Prof. Gianni Barucca

Co-Supervisor:

Dr. Gaspare Varvaro

Ph.D. Course coordinator:

Prof. G. di Nicola

XXXIII cycle - new series

Università Politecnica delle Marche
Scuola di Dottorato di Ricerca in Scienze dell'Ingegneria
Corso di Dottorato in Ingegneria Industriale

Perpendicularly magnetized synthetic antiferromagnets for flexible spintronic and biomedical applications

Ph.D. Dissertation of:

Mariam Hassan

Supervisor:

Prof. Gianni Barucca

Co-Supervisor:

Dr. Gaspare Varvaro

Ph.D. Course coordinator:

Prof. G. di Nicola

XXXIII cycle - new series

Università Politecnica delle Marche
Dipartimento di (nome del dipartimento dove la tesi e' stata sviluppata)
Via Brecce Bianche — 60131 - Ancona, Italy

Acknowledgements

I am deeply indebted to several people who have contributed in their different ways towards the completion of this thesis.

First and foremost, I would like to express my sincere and heartfelt gratitude to my supervisor, at the University of Ancona, Prof. Gianni Barucca for giving me the opportunity to do this Ph.D and to learn and grow as a researcher under his tutelage. I especially appreciate and thank him for sharing his scientific experience and knowledge and for his help in performing the TEM characterization throughout this Ph.D thesis.

I am also truly grateful to the family of SIMAU Dipartimento Scienze e Ingegneria della Materia, dell'Ambiente ed. Urbanistica at the University of Ancona including the academic staff, technicians, secretary and students for letting me belong and be one of this nice and prosperous family and to benefit from the available facilities and equipment.

I would like to also to express my profound thanks to my Co. Supervisor Dr. Gaspare Varvaro for his constant encouragement, motivation and guidance that has made my candidature a truly enriching experience. I appreciate his efforts in imparting me with his knowledge and skills at various stages of my candidature, and for offering me the opportunity to benefit from his scientific knowledge in magnetism and to be a member of the group at the Institute of Structure of Matter, CNR Rome and have access to the equipment.

I am also very thankful to Prof. Manfred Albercht and his group for offering me the honour to spend a part of my Ph.D thesis at the Institute for Physics in the University of Augsburg, Germany and to have access to his labs, especially the DC sputtering that was used to deposit the samples studied in this thesis and the VSM-SQUID utilized for the magnetic measurements.

My thanks also go to Dr. Annamaria Gerardino and Ennio Giovine for their contribution and help in the lithographic techniques, including EBL and

NSL, used in this work and for guaranteeing me the access to the clean room at the Institute for Photonics and Nanotechnologies, CNR Rome.

I would like to express my heartfelt appreciation to Dr. Sara Laureti for her endless patience who was always available to offer her help and support in any problem or difficulty I faced during my stay in Italy, as well as for sharing her scientific knowledge and her experimental skills in the part related to the lithographic techniques investigated in this thesis.

All of this would have never been possible without the love, support and inspiration of my family especially my parents and sisters. I would like to thank my father for giving me strength and my mother for her unwavering love in my life and for her continuous encouragement and emotional support.

Abstract

Although discovered about three decades ago, the peculiar properties of synthetic antiferromagnetic (SAF) thin films consisting of two ferromagnetic layers separated by a non-magnetic metal spacer have recently revived a renewed interest as potential candidates for a number of innovative and advanced applications including spintronics and biotechnology. SAFs are key component in spintronic devices and a significant attention has been recently paid on the preparation of such devises on flexible substrates, which provide wide advantages over their conventional rigid-substrate counterparts, such as the ability to bend and adjust the shape of a device, a light-weight and low costs. While the progress and development of systems with longitudinal magnetic anisotropy on non-planar substrates has been remarkable over the last few years, flexible magneto-resistive heterostructures with perpendicular magnetic anisotropy (PMA) are rather unexplored despite they allow for additional functionality and improved performance. On the other hand, for diagnostic and therapeutic applications, perpendicular magnetized SAF microdisks prepared by top-down lithographic approaches have been recently proposed as a valid alternative to the most investigated superparamagnetic particles synthetized by chemical routes as they fulfill all the key criteria required for biomedical applications while allowing a significant degree of control and tunability of the magnetic properties.

Within this context, this thesis aims at developing and studying magneto-resistive spintronic devices on flexible substrates and microdisks for biomedical applications based on SAF thin film stacks with PMA. The focus was on Co/Pd- and Co/Ni-based systems due to their strong PMA (~10^6 J/m^3) and the possibility to finely tune their magnetic properties by varying the thickness of the individual layers and the number of repetitions N of the Co/Pd(Ni) bilayer. In particular, flexible Co/Pd(Ni)-based giant magnetoresistance spin-valve thin film stacks consisting of a $[Co/Pd(Ni)]_N$

free layer and a fully compensated $[Co/Pd(Ni)]_N/Ru/[Co/Pd(Ni)]_N$ synthetic antiferromagnet reference electrode separated by a Cu spacer, were prepared by direct deposition on flexible substrates and by exploiting both wet and dry-etching transfer-and-bonding approaches. Measurements under bending conditions were also performed to investigate the robustness of the flexible spin-valves and the possibility for their integration on curved surfaces. The optimized SAF stacks were also used for the preparation of thin fil stacks consisting of multiple repeats of single $[Co/Pd]_N/Ru/[Co/Pd]_N$ SAF units with perpendicular magnetic anisotropy with the aim to fabricate free-standing SAF microdisks by using lithographic processes.

Contents

Università Politecnica delle Marche....1
Scuola di Dottorato di Ricerca in Scienze dell'Ingegneria 1
Perpendicularly magnetized synthetic antiferromagnets for flexible spintronic and biomedical applications 1
Mariam Hassan....1
Prof. Gianni Barucca 1
Dr. Gaspare Varvaro....1
Prof. G. di Nicola 1
Università Politecnica delle Marche....1
Scuola di Dottorato di Ricerca in Scienze dell'Ingegneria 1
Perpendicularly magnetized synthetic antiferromagnets for flexible spintronic and biomedical applications 1
Mariam Hassan....1
Prof. Gianni Barucca 1
Dr. Gaspare Varvaro....1
Prof. G. di Nicola 1
Università Politecnica delle Marche....1
Acknowledgements i
Abstract iv
Contents....i
List of Figures v
List of Tables.... xvii
Chapter 1. 1
Background and Outlook....1
1.1. Synthetic Antiferromagnets - Fundamentals....1
1.2. Synthetic antiferromagnets - Spintronics 6
1.2.1. Fundamentals of spintronics....6
1.2.2. Synthetic antiferromagnetic spintronics....18
1.2.3. Flexible Spintronics....20
1.3. Synthetic antiferromagnets - Biomedicine 23
1.3.1. Fundamental aspects....23

1.3.2. Synthetic antiferromagnetic microdisks 25
1.4. Outlook of the thesis 28
Chapter 2. 30
Materials, methods and characterization 30
2.1. Materials 30
2.2. Sample Fabrication 33
2.2.1. Magnetron sputtering deposition technique 34
2.2.2. Lithographic techniques 36
2.2.3. GMR spin valves on flexible substrates - Experimental conditions 40
2.2.4. PMA SAF microdisks - Experimental conditions 47
2.3. Characterization 53
2.3.1. Microstructural properties 53
2.3.2. Magnetic properties 57
2.3.3. Magneto-transport properties 62
Chapter 3. 65
Perpendicularly magnetized Co/Pd SAF-based GMR spin valves on flexible substrates 65
3.1. Co/Pd-based SAF thin film stacks 65
3.1.1. Reference Co/Pd-based SAF thin film stacks on SiO_2/Si (100) substrates 65
3.1.2. Co/Pd-based SAF thin film stacks for flexible PMA-GMR spin valves 69
3.2. PMA Co/Pd SAF-based GMR spin valves 71
3.2.1. Reference PMA-GMR spin valves on SiO_2/Si (100) substrates 72
3.2.2. Flexible GMR spin valves - Direct deposition on flexible substrates 75
3.2.3. Flexible GMR spin valves - Transfer-and-bonding strategies ... 80
3.3. Conclusions and perspectives 94
Chapter 4. 97

Perpendicularly magnetized Co/Ni SAF-based GMR spin valves on flexible substrates 97
4.1. Co/Ni-based SAF thin film stacks 97
4.1.1. Co/Ni-based SAF thin film stacks on SiO_2/Si(100) substrates ..98
4.1.2. Flexible Co/Ni-based SAF thin film stacks on Teonex® tapes 103
4.2. PMA Co/Ni SAF-based GMR spin valves 106
4.2.1. Co/Ni-based GMR spin valves on SiO_2/Si(100) substrates 106
4.2.2. Flexible Co/Ni-based GMR spin valves on Teonex® tapes 109
4.3. Conclusions and perspectives 112
Chapter 5. 114
Perpendicularly magnetized Co/Pd-based synthetic antiferromagnetic micro/nanodisks 114
5.1. Co/Pd-based Multi-SAF thin film stacks with perpendicular anisotropy 114
5.2. Conclusions and Perspectives 128
Concluding Remarks 140
References 146

List of Figures

Figure 1.1. (a) Dependence of the exchange coupling strength (Jex) on spacer-layer thickness for Co/X multilayers. (b) Periodic table of A1 (Å), the spacer-layer thickness corresponding to the position of the first peak in antiferromagnetic exchange-coupling strength as the spacer-layer thickness is increased; J1 (erg/cm2), the magnitude of the antiferromagnetic exchange-coupling strength at this first peak; ΔA1 (Å), the approximate range of spacer-layer thickness of the first antiferromagnetic region; and P (Å), the oscillation period. The most stable crystal structure of the various elements is included for reference, as well as values of the Wigner-Seitz radii [rws (Å)]. An asterisk indicates that for the elements Nb, Ta, and W, only one AF-coupled spacer-layer thickness region was observed, so it was not possible to directly determine P [adapted from Ref.6]. 3
Figure 1.2. (a) Illustrative sketch of a synthetic antiferromagnetic thin film stack with perpendicular magnetic anisotropy. (b) Schematic Illustration of the field dependent magnetization loop of PMA SAF thin film stacks. Curved arrows indicate the field sweep direction, while straight arrows are used to illustrate the mutual alignment of the magnetization in the bottom and top ferromagnetic layers as a function of the external magnetic field. 6
Figure 1.3. R(H) loops measured at 4.2 K for [Fe (3nm)/ Cr (tCr)]N multilayers with tCr equal to 1.8, 1.2 and 0.9 nm and N repetitions = 30, 35 and 60 respectively (adapted from Ref.23). 7
Figure 1.4. (a) Schematic representation of the band structure of a transition metal with strong ferromagnetic properties such as Co or Ni. (b) Equivalent circuit for the two-spin sub-bands in the “two-current” model (adapted from Ref.29). 9
Figure 1.5. Illustrative sketch of a spin valve structure with in-plane magnetic anisotropy, FL and RL stand for the free and reference layers respectively. 11
Figure 1.6. (a) Illustration of the concept of spin-transfer torque in a simple F1/NM/F2 trilayer structure. (b) Torque $m\perp$ exerted on the magnetization $M2$ of the thin magnetic layer F2, which tends to get aligned along the magnetization $M1$ when electrons flow from F1 to F2 (adapted from Ref.29). 13

Figure 1.7. (a) Conduction electrons moving perpendicular to E have their spin (s) tilted by the Rashba magnetic field (HR), exerting a torque on the localized moments (S) through the exchange coupling (Jsd) and s–d-mediated Rashba field (Hsd). (b) Scanning electron micrograph detail of the patterned Pt/Co/AlOx wire array and schematic vertical cross-section of the layer. Arrows indicates the direction of the current (I), interfacial electric field (E ∥^z) and HR. The sign of E is determined from the measured orientation of I and Hsd assuming positive polarization of the conduction electrons near the Fermi level. (c) Similarly to an external magnetic field, this interaction reduces the energy barrier for magnetization reversal in the direction perpendicular to the current flow. The three-dimensional energy landscape in the presence (absence) of current is shown in red (grey) in the inset. The plot shows the magnetization energy as a function of polar angle θ calculated for a magnetic layer with the uniaxial anisotropy easy axis parallel to ^z and current flow along ^x. Both the equilibrium magnetization direction and barrier height depend on the ratio between the effective anisotropy field (HK) and Hsd (adapted from Ref.29). 14
Figure 1.8. Array design of a MRAM device (Adapted from Ref.40). 16
Figure 1.9. Typical spin-valve structures and magnetization curves. (a) Simple spin-valve structure with a single pinned layer. (b) Spin-valve structure with synthetic antiferromagnetic type pinned layer (adapted from Ref.29). 19
Figure 1.10. Sketch diagram showing: a) nanoscale and typical materials whose dimension ranges are comparable to nanoscale; b) the top-down lithographic approach. 25
Figure 1.11. Sketch diagram showing the *M-H* hysteresis loop of: a) a superparamagnetic particle; b) a magnetic vortex microdisk; c) SAF particles suitable for biomedical applications. 27
Figure 2.1. MAE times the individual Co layer thickness versus the individual Co layer thickness of Co/Pd multilayers. The vertical axis intercept equals twice the interface anisotropy, whereas the slope gives the volume contribution. Data are taken from Ref.[176]. 32
Figure 2.2. Magnetron sputtering. The powerful magnets, connected to the cathodes, confine the plasma to the regions closest to the target (adapted from Ref.[194]). 35
Figure 2.3. UHV sputter deposition system 36

Figure 2.4. A typical EBL system, consisting of a chamber, an electron gun, a column containing all the electron optics needed to focus, scan, and turn on or turn off the electron beam. 39
Figure 2.5. (a) A Raith-Vistec EBPG 5HR used for the EBL processes and (b) reactive ion etching equipment with an ICP source. 40
Figure 2.6. Sketch diagram illustrating the [Co/Pd, Ni]-based GMR spin valve multistack with a SAF reference layer. 43
Figure 2.7. Sketch of the proposed Au-mediated *transfer-and-bond* approach. (a) PMA-GMR spin valves are DC sputtered on a SiO_2/Si (100) substrate covered with a weakly adhering Au layer; (b) a cellulose paint is spread over the film surface to improve the adhesion between the sample and the adhesive tape on which the multistack is transferred by a mechanical peel-off step (c). 47
Figure 2.8. Schematic structure of the film samples consisting of multiple repetitions (M) of single $[Co/Pd]_N/Ru/[Co/Pd]_N$ SAF units. 49
Figure 2.9. A schematic diagram illustrating the EBL process for the fabrication of microdisks by a top-down approach: 1) sputter deposition of the SAF thin film stack and mask spinning (top and bottom Au layer for functionalization), 2) EBL exposure, 3) Development to remove the exposed mask, 4) RIE to etch the unmasked film, 5) mask removal, 6) sacrificial resist layer dissolution to obtain free standing microdiscks. 50
Figure 2.10. A schematic diagram illustrating the EBL process for the fabrication of microdisks by a bottom-up approach: 1) spin-coating of resists on Si substrate, 2) EBL exposure of the resists, 3) development of the resists, 4) sputter deposition of the SAF thin film stack (top and bottom Au layer for functionalization), 5) lift-off in acetone to remove the dual resists between the SAF stacks, 6) sacrificial resist layer dissolution to obtain free standing microdisks. 52
Figure 2.11. SEM PHILIPS XL20 used for SEM characterization during this work. 54
Figure 2.12. A Philips CM200 microscope used for TEM characterization during this PhD thesis.....56
Figure 2.13. Simplified form of the vibrating sample magnetometer. (1) loudspeakers transducer, (2) conical paper cup support, (3) drinking straw, (4) reference sample, (5) sample, (6) reference coils, (7) sample coils, (8) magnet poles, (9) metal container (adapted from Ref.[213]).....59

Figure 2.14. Main components of the Model 10 EDA-Technologies VSM magnetometer. 60
Figure 2.15. Scheme of the geometric setup. 60
Figure 2.16. Layout of the VSM-SQUID. The sample is vibrated in a direction normal to the detection coils and parallel to the applied field. The detection coils are built in a second order gradiometer and are inductively coupled to the SQUID detector (adapted from Ref.[215]). 62
Figure 2.17. 4-point probe Van der Pauw method used for the measurement of magneto-transport properties in the GMR SV samples. 63
Figure 2.18. Experimental setup used for magneto-resistive measurements of flexible GMR-SVs with PMA under bending conditions. 64
Figure 3.1. (a) Out-of-plane field-dependent magnetization loops (M/M_s vs H) of $[Co/Pd]_6/Ru(t_{Ru})/[Co/Pd]_6$ thin films deposited on SiO_2/Si (100) as a function of the Ru layer thickness (t_{Ru} = 0.3, 0.4, 0.5 nm). The exchange coupling field, H_{ex}, defined as the field shift of the minor loop, is marked for the $[Co/Pd]_6$/Ru (0.4 nm)/$[Co/Pd]_6$ sample. (b) In-plane field-dependent magnetization loops (M/M_s vs H) of the $[Co/Pd]_6$/Ru (0.4 nm)/$[Co/Pd]_6$ film. All loops were acquired at room temperature. 67
Figure 3.2. Room temperature out-of-plane field-dependent magnetization loops (M/M_s vs H) of $[Pd(0.9)/Co(t_{Co})]_6/Ru(0.4)/[Co(t_{Co})/Pd(0.9)]_6$ SAF thin film stacks deposited on SiO_2/Si (100) substrates. 68
Figure 3.3. Room temperature out-of-plane field-dependent magnetization loops (M/M_s vs H) of $[Co/Pd]_N$/Ru(0.4 nm)/$[Co/Pd]_N$ thin film stacks deposited on SiO_2/Si (100) as a function of repetition number N (4, 6, 8). .69
Figure 3.4. Room temperature out-of-plane field-dependent magnetization loops (M/M_s vs H) of $[Pd(0.9)/Co(0.4)]_4/Ru(0.4)/[Co(0.4)/Pd(0.9)]_4$ SAF thin film stacks deposited on different substrates. 71
Figure 3.5. Magnetic and magneto-electric properties of PMA-GMR spin-valves deposited on SiO_2/Si (100) (reference samples). Top and bottom panels reports respectively on the room temperature out-of-plane hysteresis loops (M/M_s vs H) and the corresponding magneto-resistance (MR) response ($\Delta R/R_{low}$ vs H) as a function of Cu thickness: (a) 2 nm, (b) 3 nm and (c) 5 nm. Different colors and symbols are used for the upward and downward branches of both the hysteresis loops and MR curves to evidence the field sweep direction. The arrows reported in the top panel of figure (a) denote the mutual alignment of the magnetization in the FL, *top*-RL and *bottom*-RL at different

points in the loop; the same evolution of the magnetic configuration is observed in all the other samples. 74
Figure 3.6. Cross section TEM bright-field image of a GMR-SV thin film stack (t_{Cu} = 3 nm) on SiO_2/Si (100). 74
Figure 3.7. Co/Pd-based PMA-GMR spin valves deposited on Teonex® substrates. (a) Optical photograph of a free-standing and flexible PMA-GMR spin valve. (b-c) Room temperature out-of-plane hysteresis loops (M/M_s vs H) and corresponding magneto-resistance (MR) response ($\Delta R/R_{low}$ vs H) as a function of Cu thickness: (b) 2 nm, (c) 3 nm and (d) 5 nm. Different colors and symbols were used for the upward and downward branches of both the hysteresis loops and MR curves to show the field sweep direction. The arrows reported in top panels of the figures (b-c) denote the mutual alignment of the magnetization in the FL, *top*-RL and *bottom*-RL, depending on the external magnetic field. 77
Figure 3.8. Co/Pd-based PMA-GMR spin valves deposited on MICA substrates. (a) Optical photograph of a free-standing and flexible PMA-GMR spin valve. (b-c) Room temperature out-of-plane hysteresis loops (M/M_s vs H) and corresponding magneto-resistance (MR) response ($\Delta R/R_{low}$ vs H) as a function of Cu thickness: (b) 2 nm, (c) 3 nm and (d) 5 nm. Different colors and symbols were used for the upward and downward branches of both the hysteresis loops and MR curves to show the field sweep direction. The arrows reported in figure (b) denote the mutual alignment of the magnetization in the FL, *top*-RL and *bottom*-RL, depending on the external magnetic field; the same evolution of the magnetic configuration is observed in the sample of figure (d). 78
Figure 3.9. (a, c) Cross section TEM bright field and (b, d) SEM surface images of Co/Pd-based GMR-SV thin film stacks (t_{Cu} = 3 nm) deposited on (a, b) Teonex® tapes and (c, d) fresh cleaved MICA substrates. Inset in figure d reports on a magnification of a cleavage step. 80
Figure 3.10. Wet etching lift-off – Freshly cleaved KBr (100) sacrificial substrates. (a, b) Room temperature $M/M_s(H)$ out-of-plane magnetization loops and corresponding magneto-resistance (MR) curves ($\Delta R/R_{low}$ vs H) of GMR-SV thin film stacks on KBr (100) substrates as a function of Cu thickness: (a) 2 nm and (b) 3 nm. (c) Optical photograph of a free-standing and flexible PMA-GMR spin valve. (d) Out-of-plane $M/M_s(H)$ loops of a flexible spin-valve (Cu: 3 nm) obtained after dissolving the sacrificial layer. 81

Figure 3.11. Large area SEM images showing the surface of: (a) cleaved KBr (100) substrates; (b,c) GMR SV thin film stacks (t_{Cu} = 3 nm) deposited on fresh cleaved KBr (100) substrates (b) before and (c) after the transferring on a Kapton tape . Inset in figure c reports a magnification of the image. 82
Figure 3.12. Wet etching lift-off - PMMA sacrificial layer. Room temperature $M/M_s(H)$ out-of-plane magnetization loops and corresponding magneto-resistance ($\Delta R/R_{low}$ vs H) curves of PMA-GMR spin-valves deposited on PMMA/SiO_2/Si as a function of Cu thickness: (a) 2 nm, (b) 3 nm and (c) 3 nm. Curved arrows in the $M/M_s(H)$ loops and different colors and symbols for the upward and downward branches of both the hysteresis loops and MR curves are used to show the field sweep direction. The arrows reported in the top panel of figure (a) denote the mutual alignment of the magnetization in the FL, *top*-RL and *bottom*-RL at different points in the loop; the same evolution of the magnetic configuration is observed in all the other samples. 84
Figure 3.13. (a) Room temperature $M/M_s(H)$ out-of-plane magnetization loop of a flexible GMR spin-valve (Cu: 3 nm) obtained after dissolving the sacrificial PMMA layer. (b) Optical photograph of a free-standing and flexible PMA-GMR spin valve. 84
Figure 3.14. SEM images showing the surface of a GMR-SV thin film stack with a 3 nm thick Cu spacer deposited on PMMA/SiO_2/Si (100) substrates: (a) before and (b) (b) after the transfer-and-bonding process. 85
Figure 3.15. Magnetic and electric properties of perpendicular GMR-SVs deposited on Au/SiO_2/Si(100) before the peel-off procedure. Top and bottom panels report on the room temperature out-of-plane hysteresis loops (M/M_s vs H) and the corresponding magneto-resistance (MR) response ($\Delta R/R_{low}$ vs H) as a function of Cu layer thickness: (a) 2 nm, (b) 3 nm, and (c) 5 nm. Different colors and symbols are used to evidence the two sweep directions of the external field. The sketches reported in the top panels denote the mutual alignment of the magnetization (arrows) in the FL, *top* SAF-RL, and *bottom* SAF-RL at different points in the loop for the magnetic field sweep from positive to negative values. 86
Figure 3.16. Room temperature field-dependent resistance loops in the low-field region (-0.15 – 0.15 mT) of thin film stacks with t_{Cu} = 2nm deposited on Au/SiO_2/Si(100). Measurements were performed for two opposite magnetic configurations of the SAF obtained by saturating the sample with either a negative ($-H_{sat}$. panel a) or a positive ($+H_{sat,}$ panel b) saturation field of 1 T.

Thin arrows indicate the field swept direction, while the thick arrows illustrate the mutual alignment of the magnetization in the FL, *top*-RL, and *bottom*-RL at different points in the loop The hysteresis loop of the FL is subjected to a magnetic bias due to its interaction with the *top* SAF-RL whose sign depends on the magnetic configuration of the SAF: when its top layer points inward (outward) the shift is positive (negative).....87
Figure 3.17. TEM bright field image of a spin-valve stack (t_{Cu} = 3 nm) on Au/SiO_2/Si (100). The Volmer-Weber growth mechanism of the Au underlayer results in a wavy interface with the Ta buffer layer (gold arrow and dotted line). The ripple is then transferred to the Pd/SAF-RL (white arrow and dotted line) and SAF-RL/Cu (blue arrow and dotted line) interfaces. ..88
Figure 3.18. (a) Optical photograph of a flexible PMA-GMR spin-valve (t_{Cu} = 3 nm). (b) Corresponding room temperature out-of-plane hysteresis loops (M/M_s vs H) and magneto-resistive response ($\Delta R/R_{low}$ vs H). Different colors and symbols were used for the upward and downward to evidence the field sweep direction.....89
Figure 3.19. (a) Schematic representation of a bended system with out-of-plane magnetic anisotropy (EA: easy-axis) placed in a uniform magnetic field (H). Each region of the sample will experience a different angle with the external magnetic field, which depends on the sample curvature. (b) Geometrical definition of the bending angle $\theta^\circ = L \cdot 360/2\pi r$; r is the radius of the semi-cylindrical plastic support and L is the distance between the electrical contacts along the side of the sample parallel to the bending. 91
Figure 3.20. Representative room temperature magneto-resistive curves of flexible perpendicular GMR-SVs with t_{Cu} = 3nm: (a) without bending (θ = 0°) and (c,d) under a bending angle of (c) 115° and (d) 180°; the probing current I is injected parallelly to the curvature. Curves are normalized to the maximum $\Delta R/R_{low}$ value measured on the flat sample (θ= 0°). 91
Figure 3.21. Evolution of the (a) magnetic (M/M_s vs H) and (b) magnetoresistive ($\Delta R/R_{low}$ vs H) response of a planar flexible GMR spin valve (t_{Cu} = 3nm) as a function of the angle Φ between the external applied field H and the film normal. All measurements were performed at room temperature. (c) Evolution of the maximum of the GMR ratio normalized to the value at Φ = 0° as a function of the angle Φ, $GMR_P(\Phi)/GMR_P(0)$, as obtained from the curves in (b). The sketch illustrates the experimental configuration. 92

Figure 3.22. Experimental $GMR_B(\theta)$ ratio normalized to the value measured on the flat sample ($\theta = 0°$). (dots) compared with the values calculated from the model of Eq. 3.1 (continuous line). 94
Figure 4.1. (a) Room temperature out-of-plane field-dependent magnetization loops (M/M_s vs H) of $[Co(0.2)/Ni(0.7)]_N/Co(0.2)/Ru(0.4)/Co(0.2)[Ni(0.7)/Co(0.2)]_N$ SAF thin film stacks deposited on $Pd/Ta/SiO_2/Si$ (100) substrates as a function of the repetition number N. Room temperature out-of-plane (– ● –) and in-plane (– ○ –) field-dependent magnetization loops (M/M_s vs H) of sample $[Co(0.2)/Ni(0.7)]_6/Co(0.2)/Ru(0.4)/Co(0.2)[Ni(0.7)/Co(0.2)]_6$ that owns the largest effective magnetic anisotropy K_{eff}. 99
Figure 4.2. (a) Room temperature out-of-plane field-dependent magnetization loops (M/M_s vs H) of $[Co(0.2)/Ni(t_{Ni})]_6/Co(0.2)/Ru(0.4)/Co(0.2)[Ni(t_{Ni})/Co(0.2)]_6$ SAF thin film stacks deposited on $Pd/SiO_2/Si$ (100) substrates as a function of Ni layer thickness t_{Ni}. (b) Room temperature out-of-plane (– ● –) and in-plane (– ○ –) field-dependent magnetization loops (M/M_s vs H) of sample $[Co(0.2)/Ni(0.7)]_6/Co(0.2)/Ru(0.4)/Co(0.2)[Ni(0.7)/Co(0.2)]_6$ that owns the largest effective magnetic anisotropy K_{eff}. 100
Figure 4.3. (a) Room temperature out-of-plane field-dependent magnetization loops (M/M_s vs H) of $[Co(0.2)/Ni(0.7)]_6/Co(0.2)/Ru(0.4)/Co(0.2)[Ni(0.7)/Co(0.2)]_6$ SAF thin film stacks deposited on SiO_2/Si (100) substrates with different buffer-layers. (b) Room temperature out-of-plane (– ● –) and in-plane (– ○ –) field-dependent magnetization loops (M/M_s vs H) of the $[Co(0.2)/Ni(0.7)]_6/Co(0.2)/Ru(0.4)/Co(0.2)[Ni(0.7)/Co(0.2)]_6$ SAF thin film stack deposited on $Cu/SiO_2/Si$ (100). 102
Figure 4.4. (a, b and c) Room temperature out-of-plane field-dependent magnetization loops (M/M_s vs H) of SAF thin film stacks deposited on Teonex® tapes. (a) Effect of Ni layer thickness t_{Ni} (buffer-layer: Ta/Pd), (b) Effect of bilaye repetition number N (buffer-layer: Ta/Pd)*;* (c) Effect of buffer-layer effect; (d) Representative room temperature out-of-plane (– ● –) and in-plane (– ○ –) field-dependent magnetization loops.....104
Figure 4.5. Room temperature magnetic and magneto-electric properties of Co/Ni-based GMR-SV thin film stacks deposited on SiO_2/Si (100) substrates with different buffer-layers: (a) Ta/Pd and (b) Cu. For both samples a Cu/Ta capping layer was used. Top and bottom panels reports respectively on the

room temperature out-of-plane hysteresis loops (M/M_s vs H) and the corresponding magneto-resistance (MR) response ($\Delta R/R_{low}$ vs H). Different colors and symbols are used for the upward and downward branches of both the hysteresis loops and MR curves to evidence the field sweep direction. The arrows reported in the top panel of figure (a) denote the mutual alignment of the magnetization in the FL, *top*-RL and *bottom*-RL at different points in the loop; the same evolution of the magnetic configuration is observed in both samples. 108
Figure 4.6. Room temperature magnetic and magneto-electric properties of Co/Ni-based GMR-SV thin film stacks deposited on Pd/Ta/SiO_2/Si (100) with different capping-layers: (a) Cu/Ta and (b) Pd. Top and bottom panels report respectively on the room temperature out-of-plane hysteresis loops (M/M_s vs H) and the corresponding magneto-resistance (MR) response ($\Delta R/R_{low}$ vs H). Different colors and symbols are used for the upward and downward branches of both the hysteresis loops and MR curves to evidence the field sweep direction. The arrows reported in the top panel of figure (a) denote the mutual alignment of the magnetization in the FL, *top*-RL and *bottom*-RL at different points in the loop; the same evolution of the magnetic configuration is observed in both samples. 109
Figure 4.7. Room temperature magnetic and magneto-electric properties of Co/Ni-based GMR-SV thin film stacks deposited on flexible Teonex® tapers with different buffer-layers: (a) Pd and (b) Cu. For both samples a Cu/Ta capping layer was used. Top and bottom panels report respectively on the room temperature out-of-plane hysteresis loops (M/M_s vs H) and the corresponding magneto-resistance (MR) response ($\Delta R/R_{low}$ vs H). Different colors and symbols are used for the upward and downward branches of both the hysteresis loops and MR curves to evidence the field sweep direction. The arrows reported in the top panel of figure (a) denote the mutual alignment of the magnetization in the FL, *top*-RL and *bottom*-RL at different points in the loop; the same evolution of the magnetic configuration is observed in both samples. 111
Figure 4.8. Room temperature magnetic and magneto-electric properties of Co/Ni-based GMR-SV thin film stacks deposited on Pd/Ta/Teonex® tapes with different capping-layers: (a) Cu/Ta and (b) Pd. Top and bottom panels report respectively on the room temperature out-of-plane hysteresis loops (M/M_s vs H) and the corresponding magneto-resistance (MR) response ($\Delta R/R_{low}$ vs H). Different colors and symbols are used for the upward and

downward branches of both the hysteresis loops and MR curves to evidence the field sweep direction. The arrows reported in the top panel of figure (a) denote the mutual alignment of the magnetization in the FL, *top*-RL and *bottom*-RL at different points in the loop; the same evolution of the magnetic configuration is observed in both samples. 112
Figure 5.1. Room temperature (a) out-of-plane and (b) in-plane field-dependent magnetization loops (M/Ms vs H) of a $[Co/Pd]_4$/Ru(0.4 nm)/$[Co/Pd]_4$ SAF film deposited on Au/resist/SiO_2/Si.....115
Figure 5.2. XRR experimental data (open dots) and best fitting (continuous line) for $Co/Pd]_4$/Ru(0.4 nm)/$[Co/Pd]_4$ samples deposited on Au/resist and SiO_2/Si. 117
Figure 5.3. (a) Room temperature out-of-plane field-dependent magnetization loops of $\{[Co/Pd]_4$/Ru(0.4 nm)/$[Co/Pd]_4\}_M$ multi-stack thin films (M = 1, 3, 5, 6, 8) deposited on Au/resist/SiO_2/Si. The magnetization is normalized to the sample surface area. (b) Magnification of the AF-coupled field region of the hysteresis loop of samples with M = 1, 3 and 5. (c) Evolution of the saturation moment per unit are as a function of the repetition number M. 120
Figure 5.4. Room temperature in-plane and out-of-plane of-plane field-dependent magnetization loops (M/M_s vs H) of the $\{[Co/Pd]_4$/Ru(0.4 nm)/$[Co/Pd]_4\}_5$ film.....122
Figure 5.5. Cross-sectional TEM image of a $\{[Co/Pd]_4$/Ru(0.4 nm)/$[Co/Pd]_4\}_8$ film sample (M = 8) with Ta/Pd buffer layers separating the SAF units. The SAF multi-stack was deposited on an Au/resist underlayer. 123
Figure 5.6. (a) Multi-stack (M = 5) microdisks array (diameter: 2 μm, pitch: 4 μm); (b) room temperature field-dependent magnetization loops (M/M_s vs H). 124
Figure 5.7. SEM images of the patterned microdisks array, showing the resist sacrificial layer defects induced by the curing of the e-beam negative resist. 125
Figure 5.8. SEM images of the patterned arrays of microholes and microdisks (pitch and d ~ 1 μm), showing the microdisks' shape defects induced by the substrate rotation during sputtering: (a) Planar sample and (b) Tilted sample. 126
Figure 5.9. Room temperature field-dependent magnetization loops (M/M_s vs H) of Au/$\{$Ta/Pd/$[Pd/Co]_4$/Ru/$[Co/Pd]_4\}_M$/Au (M = 3) microdisks prepared on SiO_2/Si (100) without rotating the substrate during sputtering. 127

Figure 5.10. (a) Multi-stack ($M = 3$) microdisks array (diameter: 1 µm, pitch: 4 µm). (b) Room temperature field-dependent magnetization loops (M/M_s vs H). 127
Figure 5.11. SEM image of the microdisks obtained after dissolving the sacrificial resist. 128
Figure 5.12. Schematic illustration of the monolayer fabrication process. (a) Sketch of the in-plane drop-casting technique. (b) Sketch of the scooping transfer technique: 1) Addition of colloids to the interface via a tilted glass slide inside a Petri dish full with DI water, 2) spreading of the colloidal suspension so as to contact the surrounding water at the edge, 3 and 4) self-assembly of the particles upon addition of a small amount of surfactant and monolayer transfer by immersion of the transfer substrate and subsequent elevation under a shallow angle. 132
Figure 5.13. Self-assembly of PS colloids by drop-casting method using a colloidal dispersion of: (a) and (b) 0.2% w/w. (c) 0.4% w/w. (d) 1:4:colloids:ethanol. 134
Figure 5.14. Self-assembly of PS colloids by the scooping transfer technique using a colloidal dispersion of 1:4:colloids:ethanol: a) optical photograph of the substrate after collecting the PS monolayer of spheres and b) close-packed monolayer of PS spheres. 136
Figure 5.15. SEM image reporting on an example of the obtained spheres upon performing an Ar ion milling process to reduce the spheres' diameter. 137
Figure 5.16. Schematic illustration of the NSL process based on PS monolayers used as lenses and lift-off strategies: 1) spin-coating of photoresists on a substrate, 2) formation of a monolayer of PS spheres on top of the photoresists by scooping transfer technique, 3) UV light exposure of the photoresists covered by the monolayer of HCP microspheres 4) spheres removal by sonication, 5) development of the photoresists. 138
Figure 5.17. SEM images of (a) a two-dimensional hcp nanoholes array (440 nm hole diameter) formed inside S1811 photoresist after removing the spheres by ultrasound and developing the photoresist, (b) a cross section of the nanopattern showing the undercut obtained in the dual resists and (c) enlarged cross section of nanopatterns. 139

List of Tables

Table 2.1. Sputtering conditions of materials used in this work 42
Table 2.2. Main advantages and drawbacks of selected strategies for the fabrication of flexible electronics. 45
Table 2.3. Experimental conditions used for the resists preparation (spinning and baking). 52
Table 4.1. Calculated values of H_{ex}, H_c, M_s, J_{ex} and K_{eff} as a function of the repetition number N (t_{Ni} = 0.6 nm) of $[Co/Ni]_N$ SAF thin film stacks deposited on Pd/Ta/SiO_2/Si (100) substrates. 101
Table 4.2. Calculated values of H_{ex}, H_c, M_s, J_{ex} and K_{eff} as a function of the the Ni layer thickness t_{Ni} (N = 6) of $[Co/Ni]_N$ SAF thin film stacks deposited on Pd/Ta/SiO_2/Si (100) substrates. 101
Table 4.3. Calculated values of H_{ex}, H_c, M_s, J_{ex} and K_{eff} of $[Co/Ni]_N$ SAF thin film stacks deposited on different buffer-layers on SiO_2/Si (100) substrates. 103
Table 4.4. Calculated values of H_{ex}, H_c, M_s, J_{ex} as a function of the repetition number N (t_{Ni} = 0.6 nm) of $[Co/Ni]_N$ SAF thin film stacks deposited on Pd/Ta/Teonex tapes®. 105
Table 4.5. Calculated values of H_{ex}, H_c, M_s, J_{ex} as a function of the Ni layer thickness t_{Ni} (N = 6) of $[Co/Ni]_N$ SAF thin film stacks deposited on Pd/Ta/Teonex tapes®. 105
Table 4.6. Calculated values of H_{ex}, H_c, M_s, J_{ex} of $[Co/Ni]_N$ SAF thin film stacks deposited on different buffer-layers Teonex tapes®. 106
Table 5.1. Software simulation results of the XRR curve fitting of the SiO_2/Si and Au/resist sample. N is the layer number starting from the top surface, R is the layer repetition, SUB is the substrate, while t, σ and ρ are the software estimated values of thickness, roughness and density, respectively. 118
Table 5.2. Experimental conditions used for the resists preparation (spinning and baking). 138

Chapter 1.

Background and Outlook

1.1. Synthetic Antiferromagnets - Fundamentals

Antiferromagnets have long been considered an interesting but useless class of materials with little practical applications due to their intrinsic zero magnetic moment and the need for high magnetic fields to manipulate the antiferromagnetic order. However, after the discovery of the exchange-bias phenomenon in antiferromagnetic (AFM)/ferromagnetic (FM) heterostructures and the more recent demonstration that AFM spins may be manipulated by using spin polarized currents or electric fields, antiferromagnetic materials have acquired increasing relevance over the past years first as passive elements and, more recently, as active components to complement and replace ferromagnets in many technological applications including spintronics [1–4]. Despite the widespread use of crystal AFMs, an increasing attention has been recently paid to synthetic antiferromagnets (SAFs) consisting of two or more FM layers antiferromagnetically coupled through a non-magnetic (NM) middle spacer. Compared to crystal antiferromagnet, SAFs offer a number of advantages, including an ease tuning of the magnetic properties through the modulation of single layers features (e.g. type of material, thickness) and an ease manipulation and control of the magnetic configuration (parallel/antiparallel alignment) by using relative small and easily accessible

magnetic fields. The first evidence of the antiferromagnetic coupling in FM/NM/FM thin film multilayer stacks dates back to the seminal work of *P. Grünberg* and co-authors [5] who investigated the exchange coupling between Fe thin layers across Au and Cr interlayers. When an Au spacer is used, the Fe layers are ferromagnetically coupled and the strength of the coupling gradually reduces to zero with the increase of Au thickness from 0 to ~20 Å. For Cr interlayers of proper thickness, the authors observed an antiferromagnetic coupling of the Fe layers giving rise to an antiparallel alignment of the moments of the successive magnetic Fe layers. Since then, the interlayer exchange interaction in FM/NM/FM thin film stacks has become a subject of intense research. The decisive stimulus came from the discovery, by *S. Parkin* and co-authors [6], of the oscillating behavior of the interlayer exchange coupling in Fe/Cr/Fe and Co/Ru/Co multilayers, which results in a ferromagnetic or antiferromagnetic coupling depending on the non-magnetic spacer thickness (figure 1.1a). Furthermore, S. *Parkin* showed that this phenomenon occurs with almost any 3d, 4d, and 5d nonmagnetic transition metal (TM) thin films sandwiched between Fe, Co, Ni, or Ni alloy magnetic layers. The period of the oscillations in magnetic coupling was observed to be approximately the same (P = 9 - 11 Å) for all of these elements with the exception of Cr (figure 1.1b). Moreover, it was demonstrated that the magnitude of the coupling strength varies systematically within the transition metals, increasing from the 5d to 4d and 3d elements with the number of d electrons along the 3d, 4d, and 5d periods.

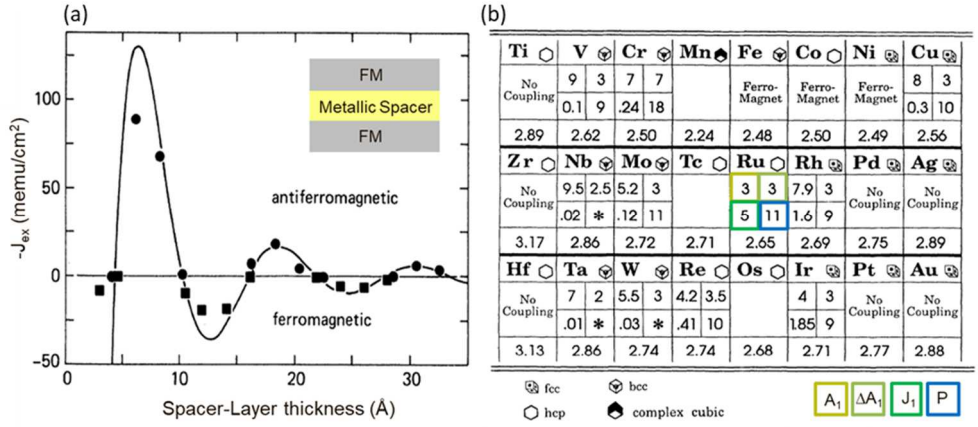

Figure 1.1. (a) Dependence of the exchange coupling strength (Jex) on spacer-layer thickness for Co/X multilayers. (b) Periodic table of A1 (Å), the spacer-layer thickness corresponding to the position of the first peak in antiferromagnetic exchange-coupling strength as the spacer-layer thickness is increased; J1 (erg/cm2), the magnitude of the antiferromagnetic exchange-coupling strength at this first peak; ΔA1 (Å), the approximate range of spacer-layer thickness of the first antiferromagnetic region; and P (Å), the oscillation period. The most stable crystal structure of the various elements is included for reference, as well as values of the Wigner-Seitz radii [rws (Å)]. An asterisk indicates that for the elements Nb, Ta, and W, only one AF-coupled spacer-layer thickness region was observed, so it was not possible to directly determine P [adapted from Ref.6].

Prior to the work of Parkin, the oscillatory indirect exchange coupling via transition metals was only addressed from studies on dilute magnetic alloys. In the *Ruderman-Kittel-Kasuya-Yosida* (RKKY) [7] model used to account for the properties of such alloys, the conduction electrons become spin polarized in the immediate neighborhood of a magnetic impurity. The spin polarization, and consequently the coupling to nearby magnetic impurities, decays with increasing distance from the magnetic impurity in an oscillatory manner. The oscillation period is given for a free-electron gas by half the Fermi wavelength, $\lambda_F/2$, of the host nonmagnetic metal, which is quite short at just ~ 1-2 atomic spacing. In contrast, the magnetic coupling through thin layers of Cr, Ru, and Cu oscillates with much longer periods, ranging from P_{Cu}

≈ 10 Å [7] and P_{Ru} ≈ 11 Å [8] to P_{Cr} ≈ 18-20 Å [8]. The transition metals do not have simple free-electron-like Fermi surfaces and the oscillation period within an RKKY-based model will be determined by the detailed topology of the Fermi surface [9,10]. In particular, P is expected to be related to peculiar wave vectors that span or nest the Fermi surface and which may give rise to large susceptibilities of the electron gas. The magnitude of such wave vectors will usually be smaller than π/λ_F, thus suggesting that the relatively long oscillation periods found for Cu, Cr, and Ru reflect the special morphology of the Fermi surfaces for each of these metals. Furthermore, in such a model, the strength of the magnetic coupling (J_{ex}) would also be determined, in large part, by the detailed Fermi surface topology [9–11]. Thus, intuitively, it would seem unlikely that either the oscillation period or the magnetic coupling strength would vary systematically among the transition metals. Therefore, one can tune the interaction from ferromagnetic — preferring parallel alignment — to antiferromagnetic — preferring antiparallel alignment — by changing the thickness of non-magnetic material between two magnetic layers. For thick spacers the interlayer exchange coupling is suppressed.

Perfect antiferromagnetic coupling in thin film heterostructures containing an even number of magnetic layers implies that in zero field the net magnetization is zero. Application of a magnetic field will tend to align the magnetic moments of the individual magnetic layers such that for fields larger than the saturation values the moments are completely aligned. The magnitude of the antiferromagnetic interlayer exchange coupling, expressed in J/m^2, is given by $J_{ex} = \mu_o H_{ex} M_s t/2a$, where H_{ex}, M_s and t are the interlayer exchange coupling field, the saturation magnetization and the thickness of the ferromagnetic layers, respectively, while a is a parameter that varies from 1 in simple sandwich structures to 2 as the number of magnetic layers becomes very large [7]. The antiferromagnetic arrangement of the magnetic layers in small magnetic fields has been confirmed by neutron-scattering experiments in a large number of systems including

polycrystalline Fe/Cr and Co/Ru multilayers [6] and single-crystal Co/Cu and Fe/Cr multilayers [12,13]. Neutron-scattering studies have also confirmed the oscillating behavior of the interlayer coupling [13].

the original works focused on SAF structures with in-plane magnetic anisotropy, a great attention has been recently devoted to systems with perpendicular magnetic anisotropy (PMA) (figure 1.2a), which are featured by an intrinsic and large uniaxial magnetic anisotropy allowing for additional functionality as well as improved performance with respect to longitudinal systems. In such structures a clear two-step behavior in the M Vs H loops can be obtained without applying any external magnetic fields during the deposition (figure 1.2b) and the antiferromagnetic coupling can be easily tuned by varying the PMA magnitude. To grow SAF with PMA, $[Co/X]_N$ multilayers (where X = Pd, Pt or Ni and N the number of repetitions) have been extensively used as building blocks [14–20] due to their large perpendicular magnetic anisotropy arising at the interface between the layers ($10^5 – 10^6$ J/m^3) [16,21,22] and the high tunability of the overall magnetic properties through the modulation of layers' thickness and number of repetitions. All these features together with the zero moment in the AFM region of the M(H) loop have made the PMA SAFs of great relevance for the development of both conventional and advanced spintronic devices for storage/processing and sensors as well as biomedical applications as described in detail in the next paragraphs.

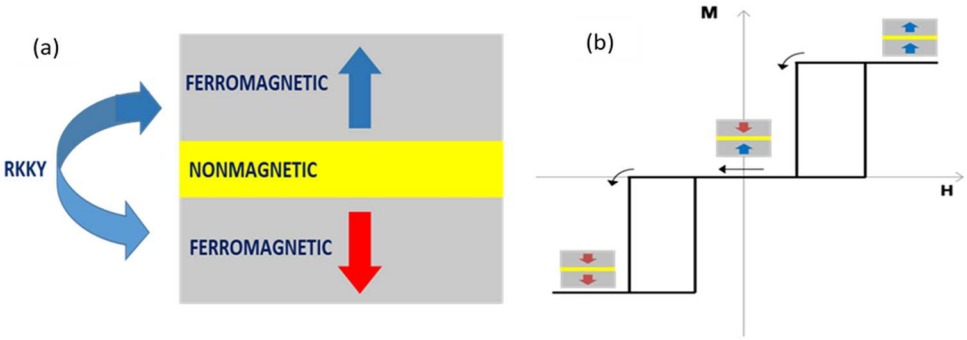

Figure 1.2. (a) Illustrative sketch of a synthetic antiferromagnetic thin film stack with perpendicular magnetic anisotropy. (b) Schematic Illustration of the field dependent magnetization loop of PMA SAF thin film stacks. Curved arrows indicate the field sweep direction, while straight arrows are used to illustrate the mutual alignment of the magnetization in the bottom and top ferromagnetic layers as a function of the external magnetic field.

1.2. Synthetic antiferromagnets - Spintronics

1.2.1. Fundamentals of spintronics

Spintronics started in the 1980's after the discovery of the giant magnetoresistance (GMR) by the groups of A. Fert [23] and P. Grünberg [24] in Fe/Cr multilayers consisting of magnetic (Fe) and non-magnetic (Cr) layers alternating along the growth direction. In zero magnetic field, the magnetization in the successive Fe layers spontaneously align in an antiparallel (*AP)* configuration due to the antiferromagnetic coupling existing between successive Fe layers across Cr spacers of proper thickness. Upon application of a magnetic field large enough to overcome the antiferromagnetic coupling, the magnetization of all Fe layers saturated in the direction of the field, resulting in a parallel (*P)* magnetic configuration. The change of the magnetic configuration from AP to P corresponds to a significant variation of the electrical resistance (80 % at 4K, 50% at 300 K)

from which the name giant magnetoresistance (figure 1.3). This result suggested that the electrons' flow through the structure depends on the electron spin and can be controlled by the relative orientation of magnetizations in adjacent layers similarly to a polarizer/analyzer optical experiment. The discovery of this *spin-dependent* effect paved the way for exploring magnetic properties of materials by means of spin-dependent transport and opened a new field of research called spin electronics or spintronics [25–28], which combines two traditional fields of physics: magnetism and electronics. The working principle is based on the spin property of the electrons, or more precisely on the spin-dependent conductivity in magnetic transition metals. The electrical current can be considered as carried in parallel by spin "up" and spin "down" electrons.

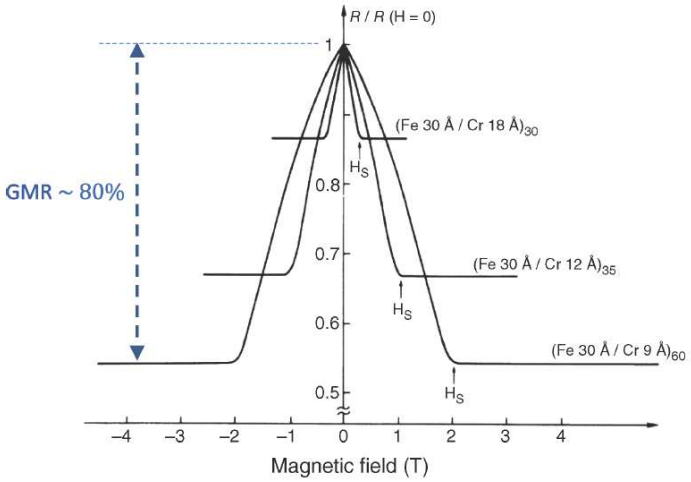

Figure 1.3. R(H) loops measured at 4.2 K for [Fe (3nm)/ Cr (tCr)]N multilayers with tCr equal to 1.8, 1.2 and 0.9 nm and N repetitions = 30, 35 and 60 respectively (adapted from Ref.23).

Accordingly, the GMR effect results from the spin-dependent scattering of conduction electrons in the bulk of the FM layers and/or at FM/NM interfaces. In ferromagnetic transition metals, such as Fe, Co, Ni and their

alloy, the two highest filled energy bands, which are the conduction bands, are occupied by 3d and 4s electrons. Each of these bands splits in two sub-bands corresponding to each spin configuration (spin angular moment of one half and minus one half) (figure 1.4a), and because of the exchange interaction among the spins, a parallel orientation is favored. By convention, the electrons with a magnetic moment aligned parallel to the local magnetization are called “spin-up” (↑) electrons, and to electrons with a magnetic moment aligned antiparallel to the local magnetization are called “spin-down” (↓) electrons. As for ferromagnetic metals, similar to a normal metal, the 4s band contains almost an equal number of spin-up and spin-down electrons. On the contrary, the 3d bands have a different energy, this offset generating an asymmetry for the number of electrons of each orientation, which is also responsible for the spontaneous magnetization. Consequently, they are also known as majority spin (↑) and minority spin (↓) electrons. In the low-temperature limit, one considers that the electron’ s spin is conserved during most scattering events. Under this assumption, transport properties associated with spin-up and spin-down electrons can be represented by two independent parallel conduction channels (figure 1.4b), and the mixing of these two conduction channels is then considered as negligible. In ferromagnetic metals, these two channels have different resistivities $\rho\uparrow$ and $\rho\downarrow$, which depend on whether the electron magnetic moment is parallel (↑) or antiparallel (↓) to the direction of the local magnetization. In a first, simple approximation, we can consider that 4s electrons, which are fully delocalized in the metal because they belong to outer electronic shells, constitute the conduction electrons that carry most of the current. In contrast, 3d electrons are more localized and responsible for the magnetic properties of the metal. The overlapping of s and d bands at the Fermi level allows current-carrying 4s electrons to be scattered on the localized 3d states, on the condition that they have the same energy and the same spin. The difference between the density of states of (↑) and (↓) 3d

electrons at the Fermi level, therefore, results in different scattering probabilities for 4s electrons with spin (↑) or (↓).

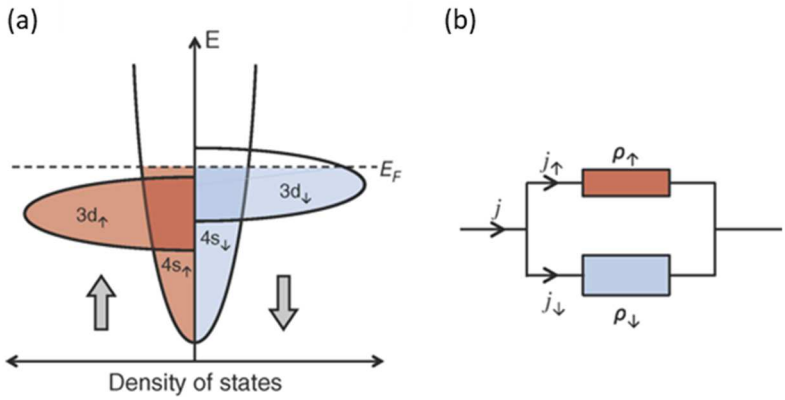

Figure 1.4. (a) Schematic representation of the band structure of a transition metal with strong ferromagnetic properties such as Co or Ni. (b) Equivalent circuit for the two-spin sub-bands in the "two-current" model (adapted from Ref.29).

Historically, the two-current model, proposed by *Mott* and then by Fert and Campbell, was developed to explain the spin-dependent resistivity in materials doped with magnetic impurities. The origin of the GMR effect is spin-dependent scattering of conduction electrons in the bulk of the FM layers and/or at FM/NM interfaces. Supposing that the conduction electrons with majority spin (spin parallel to magnetization of ferromagnetic layer) have lower probability to be scattered in the FM layers than the conduction electrons with minority spin (spin antiparallel to magnetization of ferromagnetic layer), the majority spin electrons can travel for a long distance without scattering in the parallel magnetization alignment, and, as a result, the total electric resistance of the film for the parallel alignment becomes smaller than that for the antiparallel alignment. In principle, a finite GMR effect can occur for any combinations of ferromagnetic and nonmagnetic metals and alloys. High MR ratios, however, are obtained for

certain material combinations such as Fe–Cr [30] and Co–Cu [13]. This is because the electron scatterings at Fe–Cr and Co–Cu interfaces are largely spin dependent. At Fe Cr interfaces, for example, scattering probability for minority-spin electrons is much smaller than that for majority-spin electrons because of the good matching between the Fe minority-spin band and the Cr band at the Fermi energy. At Co–Cu interfaces, on the other hand, the scattering probability is much smaller for majority spin electrons.

A second breakthrough in spintronics occurred with the discovery of the tunneling magnetoresistance (TMR) effect, which is observed in ferromagnetic materials separated by an insulating this spacer (amorphous or crystalline) and relies on the basics of quantum mechanical tunneling. As a general description, when two conducting electrodes are separated by a thin dielectric layer with a thickness ranging from a few angstroms to a few nanometers, electrons can tunnel through the dielectric layer (often referred to as the tunnel barrier) resulting in electrical conduction. The electron tunneling phenomenon arises from the wave nature of the electrons while the resulting junction electrical conductance is determined by the evanescent state of the electron wave function within the tunnel barrier. TMR-based magnetic systems are characterized by the perpendicular current-flow to the plane of the layers so that the electrons have to tunnel from one ferromagnetic layer to the other one across the thin insulating barrier. Moreover, exploiting the TMR effect allows to reach room-temperature MR ratios as high as 600 % in CoFeB/MgO/CoFeB thin film stacks [31], which is one order of magnitude larger than that reached in GMR systems (up to 55 % [32]).

Before the discovery of the GMR and TMR effects, the electron spin was neglected in mainstream charge-based electronics. In spintronic technologies, the information is carried by the electron spin, thus offering new opportunities for the development of novel devices combining standard microelectronics with spin-dependent effects arising from the interaction between spin of the carriers and the magnetic properties of the material.

Aiming to make use of the spin-transport electronics and exploit the related applications, big efforts have been carried out to benefit from the GMR and the TMR effects in a wide range of spintronic applications, particularly the spin valve (SV) and the magnetic tunneling junction (MTJ) structures. A spin valve (Figure 1.5) consists of two ferromagnetic layers separated by a non-magnetic metallic spacer (usually copper). The magnetization of the top FM layer can be easily reversed and it is called the free layer while the magnetization of the bottom FM layer (the reference layer RL) is pinned i.e., its magnetization is relatively insensitive to moderate magnetic fields [33]. Magnetic tunnel junctions look like spin valves from a magnetic point of view but a major difference is that the non-magnetic spacer consists of a very thin insulating layer.

Figure 1.5. Illustrative sketch of a spin valve structure with in-plane magnetic anisotropy, FL and RL stand for the free and reference layers respectively.

Besides the conventional way relying on an external magnetic field to control the magnetization of the free layer in magnetic heterostructures, current-induced spin-transfer torque (STT) and spin-orbit torque (SOT) phenomena provide efficient means of manipulating the magnetization, paving the way for the next generation spintronic devices. STT phenomena came after the theory of current induced magnetization switching (CIMS) that was proposed by Slonczewski [34] and Berger [35] in 1996. The theory is based on the

fact that magnetic materials have a net imbalance of spin at the Fermi level. Thus, an electrical current is not generally polarized in terms of spin. However, by driving a current through a magnetic layer, a spin-polarized current (i.e. majority of up or down spins) may be produced. Such a spin polarized current can impart some of its spin angular momentum to a second magnetic layer resulting in a torque that leads to a dynamic response of the magnetization of the second magnetic layer (figure 1.6). In spin orbit torque devices, full magnetization reversal of a single magnetic layer can be obtained without the need of a separate reference layer. Breaking of inversion symmetry is required to induce net effects on the magnetization, which is usually realized by sandwiching a ferromagnetic layer between two dissimilar layers (e.g., the Pt/Co/AlO_x heterostructure). When current flows in the structure parallel to the interfaces, in a current-in-plane configuration, a non-equilibrium spin accumulation is generated, which eventually gives rise to a torque on the magnetization via the spin transfer between *s* and *d* electrons [36]. Usually SOTs is ascribed to two different mechanisms, bulk Spin Hall effect (SHE) and interface Rashba effect, both exploiting the coupling between electron spin and orbital motion. This is the reason for the SOT name, to underline the link of these phenomena to spin-orbit interaction, which is the physical foundation of both SHE and Rashba. As an example, a current-driven SOT in a Pt/Co/AlO_x heterostructure was reported by I. Miron et al [37], and its origin is ascribed to Rashba effect in the ferromagnetic layer (figure 1.7). Electrons moving in an asymmetric crystal field potential experience a net electric field. In the electron's rest frame, this field transforms into a magnetic field, that interacts with the electron spin. Electron motion is then strictly coupled to the electron spin, so that it is possible to influence the latter by acting on the former: that is the principle on which the SOT is based.

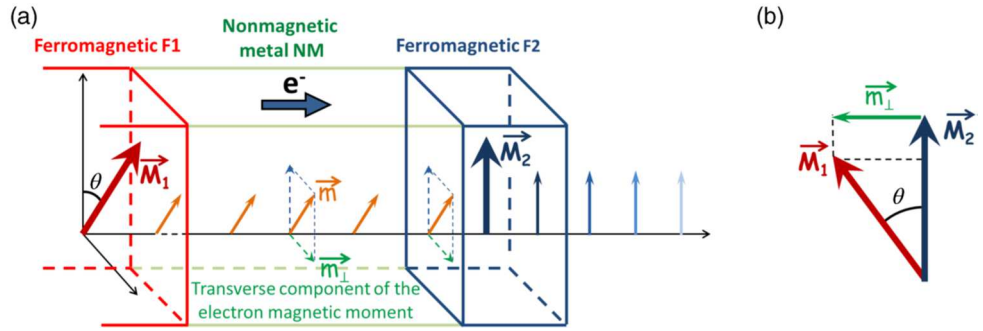

Figure 1.6. (a) Illustration of the concept of spin-transfer torque in a simple F1/NM/F2 trilayer structure. (b) Torque $\overrightarrow{m_\perp}$ exerted on the magnetization $\overrightarrow{M_2}$ of the thin magnetic layer F2, which tends to get aligned along the magnetization $\overrightarrow{M_1}$ when electrons flow from F1 to F2 (adapted from Ref.29).

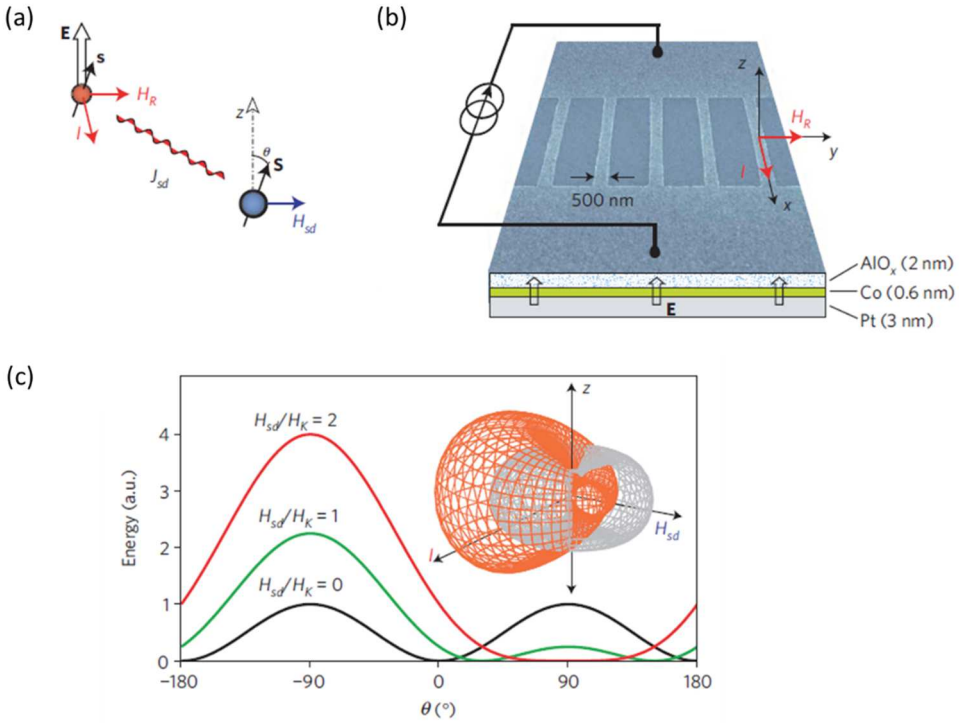

Figure 1.7. (a) Conduction electrons moving perpendicular to E have their spin (s) tilted by the Rashba magnetic field (HR), exerting a torque on the localized moments (S) through the exchange coupling (Jsd) and s–d-mediated Rashba field (Hsd). (b) Scanning electron micrograph detail of the patterned Pt/Co/AlOx wire array and schematic vertical cross-section of the layer. Arrows indicates the direction of the current (I), interfacial electric field (E ‖ˆz) and HR. The sign of E is determined from the measured orientation of I and Hsd assuming positive polarization of the conduction electrons near the Fermi level. (c) Similarly to an external magnetic field, this interaction reduces the energy barrier for magnetization reversal in the direction perpendicular to the current flow. The three-dimensional energy landscape in the presence (absence) of current is shown in red (grey) in the inset. The plot shows the magnetization energy as a function of polar angle θ calculated for a magnetic layer with the uniaxial anisotropy easy axis parallel to ˆz and current flow along ˆx. Both the equilibrium magnetization direction and barrier height depend on the ratio between the effective anisotropy field (HK) and Hsd (adapted from Ref.29).

Owing to their peculiar properties, GMR spin valves and magnetic tunnel junctions have rapidly found large-scale commercial applications as magnetic field sensors for data storage and biomolecule detection, position or proximity sensors in cars and automated industrial tools, storage elements for memory devices as well as applications in biomedicine. Magnetoresistive Random Access Memories (MRAMs) are a relatively new class of non-volatile memories, exploiting the hysteretic properties of ferromagnetic materials for data storage and the magnetoresistive effects as useful reference phenomena for data reading. Since the emergence of the MRAM concept in the mid-1980s [38,39] and the key improvement due to GMR discovery, MRAMs have attracted great attention from many big memory producers. As a matter of fact, in the quest for a "universal memory" presenting all the advantages of current technologies (DRAMs, SRAMs, flashes), MRAMs combine the high access speed of SRAMs and DRAMs and the non-volatility of Flashes. Furthermore, they present large endurance and radiation hardness. A conventional MRAM is based on a 2-dimensional array of memory cells (figure 1.8), which can be addressed individually because each cell is at the cross point of two lines (the bit line and the word line). Each cell is made of a GMR spin valve of a MTJ heterostructure, composed by two ferromagnetic layers, separated by a nonmagnetic layer. The relative direction of the magnetization in the free layer with respect to the pinned layer (parallel or antiparallel) constitutes the "bit" of information. The writing process of the bit in the cell consists in setting the magnetization of the free layer with respect to the pinned layer, parallel or antiparallel. The reading process of the bit consists in measuring the resistance of the heterostructure, whose value depends on the relative orientation of the pinned and free layers. Nowadays, the main challenge of MRAMs is increasing the storage density. The highest drawback of MRAMs is the need for high currents for writing the "bit" in the cells, and this has remained for years the bottleneck for MRAMs development. In the first implementations of MRAMs, current lines were used to write the magnetic information, but

the high energy dissipation associated with Joule heating and the poor spatial confinement of magnetic fields represented the major obstacles to the increase of memory density. This is why MRAMs have been mainly used, so far, in military and space applications where robustness and endurance are mandatory. More recently, however, there has been a renewed interest in MRAMs, essentially coming from the discovery and development of new strategies for magnetic writing, especially STT and SOT.

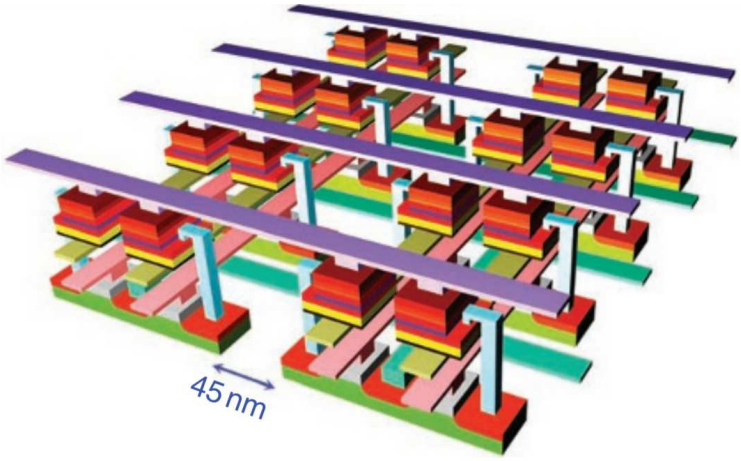

Figure 1.8. Array design of a MRAM device (Adapted from Ref.40).

In addition to magnetoresistive memories, magnetoresistive sensors are nowadays continuously gaining big interests. In the past 10 to 15 years, there has been a gradual replacement of the anisotropic magnetoresistance (AMR) effect and conventional Hall effects with GMR and TMR spintronics based magnetic effects, especially in sensor applications where higher output and signal-to-noise ratio, good thermal stability, compatibility with complementary metal oxide semiconductor (CMOS) integration, reduced cost and minimum features are required [41–43]. Major markets today include the automotive sector (angular, speed, current, position/switch sensors), industry with current and power sensors, linear and angular encoders,

scanners, and consumer electronics / smartphones (3D magnetometers/digital compasses). As an example of a linear sensor is the GMR magnetic field sensor where the magnetoresistance varies linearly with the detected magnetic field within a sensing range, thereby exhibiting a linear voltage output in the bridge structure circuit [33]. This linear change in magnetoresistance is realized by pinning the magnetization of the reference layer and controlling the magnetization direction of the free layer by the detected magnetic field, resulting in different angles of the magnetic moments between the free and reference layers under different magnetic fields [44]. In switch sensors, the magnitude of the resistance is used to sense the orientation of one magnetic layer with respect to another, that is, to indicate whether a "1" or "0" state is stored in the parallel or antiparallel alignment of the two ferromagnetic layers. The same current that is employed to read the magnetic state of the device can be used to switch it, if the current density is increased beyond a critical threshold, by transferring spin angular momentum from the reference layer to the free layer via the STT. Thus, all electrical operation is achieved, with a tunable trade-off between high speed and low power [45]. Currently, in the automotive industry, various magnetic sensor principles represent solutions used for example in ABS (anti blocking systems), drive by wire, engine management and ESP (electronic stabilization program). In the last years, a robust GMR sensor in a full Wheatstone-bridge configuration has been reported that allows the possibility to exploit the full potential of the GMR effect for automotive applications. Thus, many research studies were carried on the optimization of the output characteristics of the GMR sensor with respect to different applications in automotive and industrial environments, namely for angular position sensing and rotational speed sensing and first results of the packaged GMR sensor were presented by C. Giebeler et al in 2001[46].

1.2.2. **Synthetic antiferromagnetic spintronics**

The ferromagnetic reference layer in SVs and MTJs is generally pinned by coupling it to an antiferromagnetic layer AFM due to the exchange bias effect. This effect arises from the "unidirectional" magnetic anisotropy induced at the interface because of the exchange coupling between the two layers at the interface. However, when an antiferromagnetic pinning layer is used, the magnitude of the exchange field may be unable to completely pin the magnetization of the reference layer and a partial loss of the pinning direction may occur when the size of the heterostructure gets into the sub-micrometer range due to the presence of self-demagnetizing fields. Moreover, the use of an AFM pinned layer does not affect the stray magnetic fields produced by the reference layer, which act on the free layer inducing an offset of the center of the corresponding hysteresis loop, thus causing, to destabilize the parallel and antiparallel magnetic states in memory arrays (figure 1.9a) [47,48].

To minimize the unwanted stray fields on the free layer, spin-valve devices with a SAF reference layer were proposed [2,49]. Because the SAF trilayer forms a *flux closure* structure, most of the flux from the reference layer is absorbed in the pinned layer. This results in a suppression of the stray field and as a result induces a negligibly small offset of the free layer hysteresis loop (figure 1.9b). This structure improves both stand-off magnetic fields and the temperature of operation of the spin valve. Furthermore, for some practical memory applications like for MRAM where the enhanced magnetic stability is a critical factor, usually the magnetization direction of the top FM layer in the SAF structure is pinned by exchange bias from antiferromagnetic coupling to the bottom layer when this SAF is used as a reference layer in MTJs and SVs with an in-plane magnetic anisotropy. Added to those discussed advantages, a SAF reference layer enables to achieve SV and MTJ structures with strong PMA by using Co/X multilayers as ferromagnetic layers which are capable of guaranteeing a large tunable

uniaxial PMA through the modulation of the individual magnetic layers' thicknesses and the number of Co/X bilayers. The use of materials with PMA-SAF reference layers represents a solution to the problems arising from the size reduction of magnetic elements. The GMR amplitude has been also significantly enhanced (up to 20%) by using PMA SAF-based reference layers and by improving the overall structural quality of the stack by adding Co-rich interfacial layers [50].

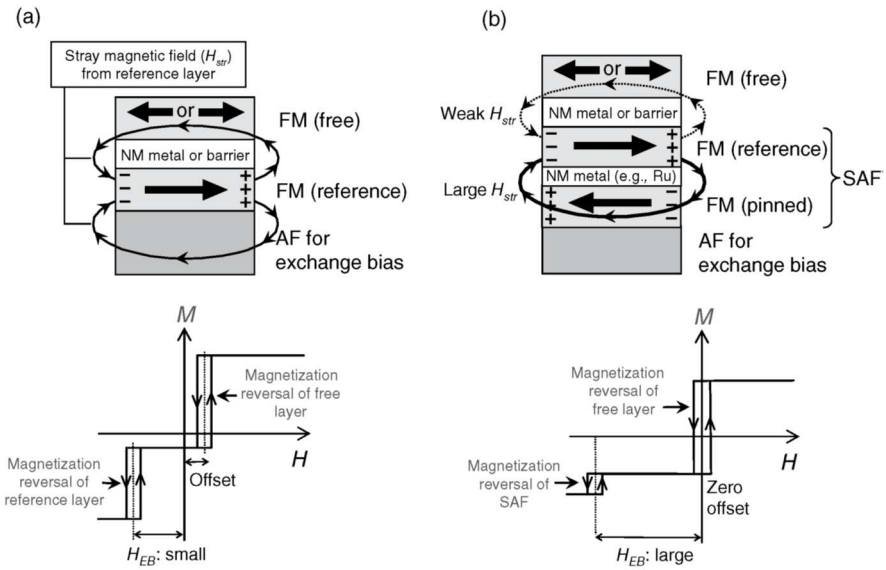

Figure 1.9. Typical spin-valve structures and magnetization curves. (a) Simple spin-valve structure with a single pinned layer. (b) Spin-valve structure with synthetic antiferromagnetic type pinned layer (adapted from Ref.29).

Although most of the work on SAFs for spintronic applications has been focused on their use as reference electrodes in GMR-SVs and MTJs, PMA-SAF thin film stacks have been demonstrated to be also of great relevance for the development of novel and advanced PMA spintronic devices exploiting the movement of domain walls [51] or the displacement and the size change of skyrmions (i.e. a topologically-protected solitons) [52–57]. In addition, a very attractive and emerging research direction, which exploits

the relatively weak AFM coupling of synthetic antiferromagnets, consists on controlling the interlayer exchange interactions by using electric fields [58–60] with the aim to develop voltage-controlled spintronic devices characterized by a much lower power consumption with respect to the most common investigated spintronic systems controlled by electrical currents. Besides, in many studies, PMA-SAFs have been employed as free layers in MTJ and SV stacks with the aim to get magnetic devices with high energy barrier values, low offset fields and a high coercivity, that are suitable for spintronic applications such as spin-torque MRAM micro-wave-assisted magnetic recording and thus enable improved stability of the parallel or antiparallel magnetic state in the free layer [61–63].

1.2.3. **Flexible Spintronics**

Flexible electronics has received a great deal of attention over the past few decades owing to its outstanding potential in many technological fields including energy, optics, sensors and information storage, among others [64–66]. Flexible devices show peculiar and exclusive features with respect to their conventional rigid-substrate counterparts. They are arbitrarily re-shapeable, bendable, elastic, light weight, unbreakable and generally require lower processing costs to be fabricated [67]. All those advantages represented the driving force for the ever-growing research in flexible electronics devices that, starting with the fabrication of the first flexible solar cell in 1960 [67], have nowadays shown all their outstanding potentialities in many technological fields. Indeed, extensive research studies have been reported on stretchable integrated circuits [68,69], bendable batteries [70,71], light-emitting diodes [72], flexible [73,74], and stretchable magnetoelectronics [75], rollable electronic displays [76,77], ultrathin transistors [78,79], solar cells [80], and paper-based electronics [81].

Two basic approaches are generally exploited for the fabrication of flexible electronics devices, i.e., i) direct deposition on flexible substrates and ii)

transfer and bonding strategies where the whole structure is first deposited by standard methods on a rigid substrate and then transferred on a flexible tape [82–85]. The direct deposition on flexible tapes is a low-cost one-step process that allows high surface coverages [86]. The most used flexible substrates are organic polymers including polyethylene terephthalate (PET), polyethylene naphthalate (PEN), polyethersulphone (PES), polyimide (PI), and polydimethylsiloxane (PDMS) [87]. These organic polymers are highly flexible, inexpensive, and compatible with the roll-to-roll processing [88]; however, they are not compatible with the fabrication of complex structures due to the high surface roughness and low thermal stability compared to rigid substrates. Other flexible substrates, including natural MICA and ultra-thin Si substrates were recently proposed to overcome these issues [89]. MICA is a natural mineral, which can be mechanically exfoliated to obtain atomically flat sheets with a good mechanical bendability for thickness below 100 µm [90]. Due to the high thermal stability of MICA (up to ~800 K for muscovite and ~1200 K for phlogopite [91]) single layer of functional oxide thin films have been successfully grown on MICA substrates based on the concept of van der Waals epitaxy [92]. However, its applicability to more complex heterostructures as well as its compatibility with industrial manufacturing processes have been not yet demonstrated. Ultra-thin Si substrates have a high flexibility for thickness below 100 µm [93] and has been recently used to obtain high quality complex heterostructures; however, the fabrication of ultra-thin Si substrates requires complex procedures involving reactive ion etching steps, thus complicating the overall fabrication process. As concerns the transfer and bonding approaches, both wet etching lift-off strategies exploiting the selective solubility of sacrificial layers and dry transfer lift-off methods based on the adhesion strength between the rigid substrate and the thin film structure, have been proposed to transfer the whole structure on a flexible tape by using fluidic self-assembling and peeling procedures [94–97]. The main advantages of these approaches are the possibility to use thermally stable crystalline and smooth substrates/layers,

the compatibility with existing microfabrication processes and the possibility to transfer the structure on arbitrary flexible tapes. The main drawbacks are the small surface area coverage due to the random damage during the transfer procedure and the high processing costs.

Aiming at widening the domain of flexible electronics, a significant effort has been recently pursued to develop spin-related electronic devices on flexible substrates [67,98]. A special attention has been paid to flexible magneto-resistive sensors with potential applications in many different sectors, including automotive, wearable electronics, soft robotics, bio-integrated electronics and functional implants [99–102]. They include among others Hall-effect sensors for large magnetic field measurements, GMR and MTJ sensors for detection of small magnetic fields (mT range or below), and magneto-impedance sensors for passive and wireless devices [99,103–109]. As concerns the GMR and MTJ heterostructures, while the progress and development of flexible systems with longitudinal magnetic anisotropy has been remarkable over the last years, magneto-resistive heterostructures with perpendicular magnetic anisotropy are rather unexplored despite they allow for additional functionality and improved performance arising from the intrinsic and large uniaxial magnetic anisotropy that guarantees higher thermal stability and low-switching current density characteristics as well as the absence of cell aspect ratio limitations in such structures. Indeed, despite the high potential of perpendicular magnetized spintronic devices, the fabrication of such heterostructures on flexible substrates is more complex as crystalline, smooth and thermally stable substrates and/or buffer layers are generally necessary, thus requiring the development of proper strategies.

1.3. Synthetic antiferromagnets - Biomedicine

1.3.1. Fundamental aspects

Mesoscale magnetic particles (from few nanometers to microns) are among the most promising materials for clinical diagnostic and therapeutic applications [110–119]. Due to their unique physical properties and their ability to interact with biological entities at the cellular and molecular level, magnetic particles have been actively investigated for labeling and manipulation of biomolecules, delivery and release of drugs, manipulation and mechanical disruption of cells, magnetic resonance imaging as well as hyperthermia (figure 1.10a). These applications require an aqueous suspension of ideally monodisperse entities with high magnetic moment at saturation, zero remanence, low field susceptibility, and sharp switching to saturation together with the ability to vary the size and the total magnetic moment. A high magnetic moment at saturation ($m_s = M_s V$, where M_s is the saturation magnetization and V the particle's volume) is required for an efficient manipulation of magnetic particles by an external magnetic field. Zero remanence and a low field susceptibility are needed to prevent particle agglomeration, while a sharp switching to saturation is required for an efficient access to the saturation state. Moreover, for specific applications, such as the mechanical disruption of cells, also a high uniaxial magnetic anisotropy is desired to make the transduction of the torque from an external magnetic field more efficient [120–128].

Among the different materials, superparamagnetic metal-oxide particles with diameters of the order of few nanometers prepared by chemical methods (*bottom-up* approach) have been largely investigated, as they have zero moment at zero field thus preventing particles' agglomeration when the external field is removed [112,116,117,129,130]. When the size of a ferromagnetic particle is reduced down to a critical radius (depending on the magnetic material properties), a magnetic single-domain state (i.e., a

particle that is in a state of uniform magnetization) is energetically more favorable. Further size reduction might lead to a superparamagnetic state where the magnetic particle is characterized by thermal instability that results in the flip of magnetization between its antiparallel magnetic easy directions, which is associated with an energy barrier ΔE_a. According to the *Néel–Brown* theory [131,132], above a certain temperature (i.e., the blocking temperature T_b) and on a given time scale, the particle magnetic moment exhibits thermally activated transitions. Below T_b, the particle's moment is blocked and unable to rotate over the barrier in the time of the measurement. Despite superparamagnetic particles having attracted a great deal of attention in view of their potential use for biomedical applications, producing large amounts of particles with controlled and homogenous size, shape, and magnetic properties is still a challenge. Moreover, due to the small size, the particles show small values of m_s and high magnetic fields are required to manipulate these particles. Enhancing the magnetic moment by increasing the particle size may lead the particle to exit the superparamagnetic regime and consequently aggregate, as expected for a system of interacting ferromagnetic particles. A possible solution is to synthetize composite systems consisting of many non-interacting superparamagnetic particles [133–135] but some limitations are still present due to the homogeneity of composite morphology (size and shape) and corresponding magnetic properties.

Recent studies have demonstrated that *top-down* approaches (figure 1.10b) based on techniques developed for micro/nanoelectronics can be used to fabricate monodisperse magnetic micro/nano-objects with rather complex structure and shape that are challenging to obtain by means of chemical synthesis [121,122,143–150,126,136–142]. In this case, a continuous film is deposited by physical vapor deposition methods (e.g., sputter deposition) onto a substrate covered with a sacrificial resist. Then arrays of magnetic entities are fabricated by combining lithographic techniques and ion-etching processes. Finally, a stable solution of free standing objects is obtained by

dissolution of the sacrificial resist and dispersion in a given solvent after proper functionalization of the surface. One outstanding practical issue of top-down approaches relates to the prospects for obtaining large quantities of micro/nano-objects with high efficiency and at reasonable cost. In this regard, different cost- and time-effective lithographic approaches have been recently developed to obtain micro/nano-structures on large areas [151–154]. In particular, it has been demonstrated that by using nanosphere or nanoimprinting lithography techniques [139,141–143,145,155], it is possible to fabricate, in a reasonable time and at low costs, arrays of micro/nano-objects on large area silicon substrates allowing massive production of particles with controlled size and physical properties.

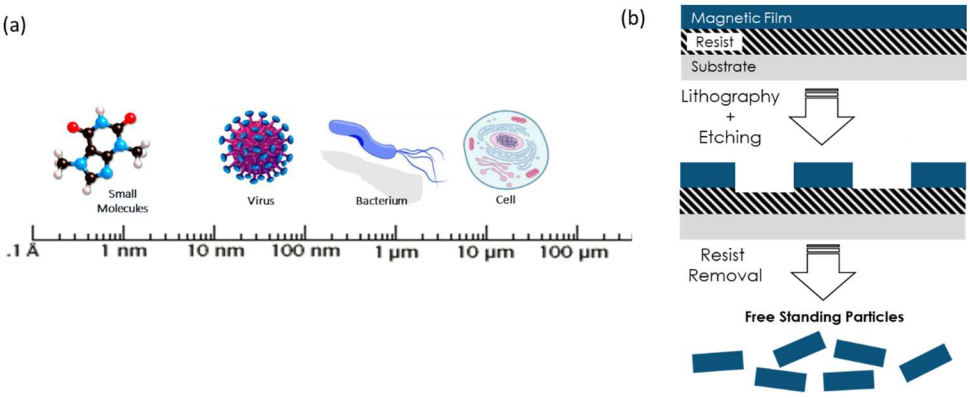

Figure 1.10. Sketch diagram showing: a) nanoscale and typical materials whose dimension ranges are comparable to nanoscale; b) the top-down lithographic approach.

1.3.2. **Synthetic antiferromagnetic microdisks**

The necessity to overcome the difficulties encountered by the use of superparamagnetic particles in many biomedical applications (figure 1.11a) [156–160] have forced the research path to focus on designing nanostructures with large magnetic moments that are not restricted to the

superparamagnetic limit. To this aim, top-down approaches have been successfully used to fabricate magnetically soft micro/nanodisks, where the physical constraints imposed by the structure size leads to the formation of a magnetic vortex state at remanence where the magnetization circulates in the plane of the disk [137–140,150] (figure 1.11b). Such a peculiar magnetic configuration gives rise to zero remanence at zero field, making this material potentially interesting for biomedical applications. However, although the monodispersity and the physical properties can be better controlled with respect to particles prepared by chemical methods, magnetic vortex microdisks still exhibit, like superparamagnetic particles, a high susceptibility at low fields that can lead to agglomeration due to small magnetic stray fields from the environment. A promising alternative is represented by employing synthetic antiferromagnetic micro/nanodisks [121,122,149,141–148] owing to the advantages that such heterostructures offers for biomedical applications including the zero remanence, low field susceptibility, and the sharp switching to saturation together with the ability to vary the total magnetic moment of these structures (figure 1.11c). Moreover, SAF micro/nanodisks offer the possibility to adjust the thickness of the magnetic layers and to modify the surface of SAF, and this allows to use small external magnetic fields which is very useful to separate and manipulate biological targets or materials linked to SAF surfaces [161].

A lot of research activity has been done to study SAF-IP disks and tune their magnetic properties by investigating the effect of nonmagnetic spacers, magnetic layers as well as their thicknesses on the interlayer magnetic interactions with the aim to achieve zero remanence, zero field susceptibilities and high saturation magnetizations as required for biomedical applications [141,162]. In this regard, IP-SAFs consisting of $Co_{90}Fe_{10}$ ferromagnetic layers separated by Ru spacer were studied by Hu et al. who investigated the effect of $Co_{90}Fe_{10}$ and Ru thicknesses on the magnetic properties of the SAF [141]. They claimed that they were able to prepare SAF-IP nanoparticles with a saturation magnetization of 850 emu/cm^3 which is

around 2.5 times higher than that of the iron oxide nanoparticles (340 emu/cm^3) used for biomedical applications. In another study, SAF nanodisks with in-plane magnetic anisotropy consisting of Au/$Ni_{80}Fe_{20}$/Au/$Ni_{80}Fe_{20}$/Au were also prepared and studied for MRI contrast agents [162]. The authors were able to fabricate SAF nanodisks that showed a very low magnetic remanence and high magnetization, making them perfectly suitednfor biomedical applications.

While most studies are focused on SAF micro/nanodisks with in-plane magnetic anisotropy [141–145], few recent works reported on micro/nanodisks with perpendicular magnetic anisotropy [121,122,146–149]. Large PMA values together with the zero remanence and the m_s tunability is a unique combination that cannot be achieved in particles prepared by chemical methods, thus making PMA-SAF microdisks of particular interest for all the biomedical applications relying on the transduction of a mechanical force through the particles under an external magnetic field. Recently, it has been shown that perpendicularly magnetized FeCoB/Pt/Ru/Pt/FeCoB SAF microdisks are characterized by zero remanence, low field susceptibility, a distinct switching field to full magnetization and a precise tunability, making them ideal for tailoring specific biomedical applications.

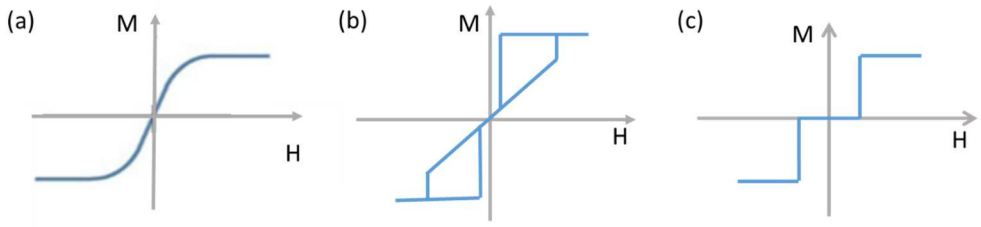

Figure 1.11. Sketch diagram showing the *M-H* hysteresis loop of: a) a superparamagnetic particle; b) a magnetic vortex microdisk; c) SAF particles suitable for biomedical applications.

1.4. Outlook of the thesis

To further contribute to the above innovative and promising research fields, the thesis aims at designing, preparing and systematically investigating the magnetic, morphological and magneto-resistive properties of thin film stacks based on SAFs with perpendicular magnetic anisotropy for flexible spintronics and biomedical applications. The focus was on Co/Pd- and Co/Ni-based systems owing to the large PMA of Co-based multilayers (up to ~$8 \cdot 10^6$ J/m^3 [22]), the high tunability of their magnetic properties through the modulation of the individual layers' thickness and number of bilayer repetitions [163,164] together with the possibility to virtually obtain such structures on any substrates. Co/Pd is a widely-used building block of stable and PMA-GMR spin valves. Co/Ni is a less studied system that has recently attracted a great deal of attention in many spintronics applications due to the additional advantages it offers, particularly the low cost of Ni compared to Pd, its low damping [17,165–167] and high spin polarization [168], added to the advantage that both Co and Ni are magnetic. Aiming at widening the domain of flexible spintronics, different approaches including the direct deposition on different flexible substrates as well as dry and wet etching transfer-and-bonding strategies were developed and compared to obtain PMA [Co/Pd]-based GMR spin valves, consisting of a fully compensated $[Co/Pd]_N/Ru/[Co/Pd]_N$ synthetic antiferromagnet (SAF) reference layer and a $[Co/Pd]_N$ free layer. Besides endowing the family of flexible electronics with PMA magneto-resistive heterostructures, the complexity of the structure, whose properties are strongly affected by the quality of the interfaces, makes such a system a perfect candidate to test and demonstrate the potential of the proposed strategies. The best strategy was then used to prepare flexible PMA [Co/Ni]-based GMR spin valves, consisting of a fully compensated $[Co/Ni]_N/Ru/[Co/Ni]_N$ synthetic antiferromagnet (SAF) reference electrode and a $[Co/Ni]_N$ free layer. The last part of the thesis is dedicated to the preparation and study of microdisks for biomedical

applications using top-down strategy combining electron beam lithography (EBL) and Ar ion milling processes. The microdisks consisted of multiple repeats of single $[Co/Pd]_N/Ru/[Co/Pd]_N$ SAF units with perpendicular magnetic anisotropy. The high PMA of Co/Pd is supposed to be beneficial for all the biomedical applications relying on the material's magnetic anisotropy such as the mechanical destruction of cells [121]. Moreover, the resulting greater thermal stability of the Co/Pd system [169] might allow smaller disks to be fabricated without compromising the overall magnetic properties due to thermal effects.

It is worth mentioning that the samples studied in this PhD thesis were prepared in collaboration with Prof. M. Albercht at the University of Augsburg (Germany). Magnetic measurements were performed within the supervision of G. Varvaro from the Institute of Structure of Matter at the National Research Council (Rome, Italy). TEM analysis was performed with Prof. G. Barucca in the Polytechnic University of Marche (Ancona, Italy). The magnetoresistive measurements were done at the Polytechnic University of Milano in collaboration with Dr. C. Rinaldi and F. Fagiani. The lithographic approaches and lift-off techniques were done in collaboration with A. Gerardino and E. Giovine at the Institute for Photonics and Nanotechnologies of the National Research Council (Roma).

Chapter 2.

Materials, methods and characterization

2.1. Materials

SAF and GMR-SV thin film stacks with perpendicular magnetic anisotropy (PMA) were obtained by using $[Co/X]_N$ multilayers (where X = Pd, Ni and *N* the number of bilayers) were used as building blocks due to their large perpendicular magnetic anisotropy arising at the interface between the layers ($10^5 – 10^6$ J/m^3) [1–3]. This type of magnetic anisotropy, named interface or surface anisotropy, was predicted in 1954 by Néel [170] as a result of the lower symmetry at the surface or interface and was first observed experimentally in 1968 by *Gradmann* and *Müller* [171] on ultrathin NiFe films on Cu(111). For NiFe film thickness as lower as 1.8 monolayers, the system develops a perpendicular magnetic anisotropy whose magnitude scaled with the reciprocal of the film thickness. For multilayers, PMA was first observed in 1985 by *Carcia et al* in the Co/Pd systems [172] and later on in several other Co-based multilayers: Co/Pt [173], Co/Au [174], Co/Ru [175] and Co/Ir [176] as well as Co/Ni [177].

In such multilayer systems, the (effective) magnetic anisotropy energy K (Jm^{-3}) could be phenomenologically separated in a volume contribution K_v (Jm^{-3}) and a contribution from the interfaces K_s (Jm^{-2}) and approximately obeyed the relation:

$$K = K_{eff} = K_v + 2K_s/t \qquad (2.1)$$

This relation just represents a weighted average of the magnetic anisotropy energy (MAE) of the interface atoms and the inner atoms of a magnetic layer of thickness t. The relation is presented under the convention that K_s/d (with d the thickness of a monolayer) represents the difference between the anisotropy of the interface atoms with respect to the inner or bulk atoms. Also the layer is assumed to be bounded by two identical interfaces accounting for the pre-factor 2. Equation (2.1) is commonly used in experimental studies, and the determination of K_v and K_s can be obtained by a plot of the product K_{eff} t versus t. Figure 2.1 shows a typical example of such a plot for Co/Pd multilayers [176]. Here, and in the following, a positive K_{eff} describes the case of a preferred direction of the magnetization perpendicular to the layer plane. The negative slope indicates a negative volume anisotropy K_v, favouring in-plane magnetization, while the intercept at zero Co thickness indicates a positive interface anisotropy K_s, favoring perpendicular magnetization. Below a certain thickness $t_\perp$ (= $-2K_s/K_v$, in this case 13 Å) the interface anisotropy contribution outweighs the volume contribution, resulting in a perpendicularly magnetized system. In other words, the strong demagnetizing fields which are created when tilting the magnetization out of the film plane and which are usually responsible for the orientation of the magnetization parallel to the film plane, are overcome. The volume energy corresponding to these demagnetizing fields form the major contribution to K_v in most cases.

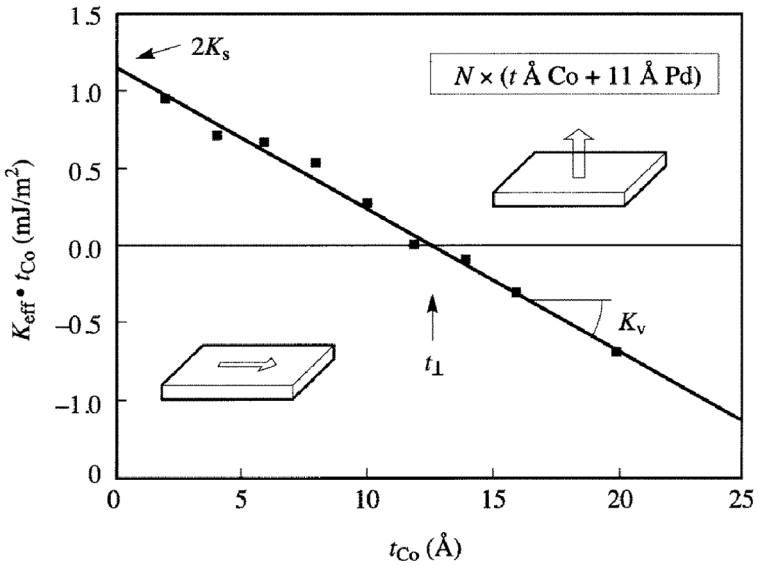

Figure 2.1. MAE times the individual Co layer thickness versus the individual Co layer thickness of Co/Pd multilayers. The vertical axis intercept equals twice the interface anisotropy, whereas the slope gives the volume contribution. Data are taken from Ref.[176].

The large perpendicular magnetic anisotropy of $[Co/X]_N$ multilayers (where X = Pd, Pt, Ni, ...) together with the high tunability of the overall magnetic properties through the modulation of layers' thickness and number of repetitions has made these multilayer fundamental building blocks of SVs and MTJs with perpendicular magnetic anisotropy. Among them, Co/Pd and Co/Pt multilayers represent well-known and widely-used materials, particularly [Co/Pd]-based systems are attractive as they are expected to exhibit a higher and more stable GMR, with high perpendicular anisotropy due to the thinner Pd thicknesses as compared to a [Co/Pt] system [178]. Moreover, the use of certain buffer layers is also capable in some cases of tuning the PMA. In SAF structures based on Co/Pd or Co/Pt multilayers, an appropriate buffer layer (usually Pt or Pd) is essential to obtain large PMA values [179]. For instance, Co/Pt multilayers grown on Ru exhibit weaker PMA anisotropy than when grown on Pt or Pd. Furthermore, in some studies, a Ta

and Ta/Pd buffer layer was used to induce a (111) crystallographic texture, and thus obtain large perpendicular magnetic anisotropy in Co/Pd and Co/Pt multilayers [180,181]. A lot of studies were carried out to investigate the magnetic properties of Co/Pt and Co/Pd systems including the saturation magnetization and the effective magnetic anisotropy energy. For $[Co/Pt]_N$ multilayers [182], K_{eff} was found to vary between $0.5x10^6$ and $1.5x10^6$ KJm^{-3} while M_s varied from 600 to 1500 KAm^{-1}. For Co/Pd system [183183], M_s changed between 500 and 1000 KAm^{-1} while K_{eff} from $5x10^5$ to $8x10^5$ KJm^{-3}.

Co/Ni multilayers formed of two magnetic components offer additional advantages over Co/Pd or Co/Pt multilayers, including the low cost of Ni compared to Pt and Pd, the low damping [17,165–167] and high spin polarization [168]. To promote the PMA in Co/Ni multilayers an fcc (111) oriented nonmagnetic underlayer, such as Cu, Au and Ti, is generally exploited [184–187]. M_s of Co/Ni system is about 600 kAm^{-1} while K_{eff} is about 240 kJm^{-3} [16,188]. Co/Ni have attracted a great deal of attention for STT applications due to its large PMA which makes devices require small switching currents and acquire high thermal stability. More recently, Co/Ni multilayers were demonstrated to be a promising candidate for SOT devices to control and manipulate the magnetization, relying on current-induced switching of the magnetization in systems with strong spin-orbit interactions [189]. In such systems, a heavy metal such as Pd, Pt, Ta or W can be spin-orbit coupled to the ferromagnetic layer, thus generating a pure spin current to exert strong torques on the magnetic layer [190,191].

2.2. Sample Fabrication

All multilayered thin film stacks were deposited by magnetron sputtering at the laboratories of Prof. M. Albrecht of the University of Augsburg (Germany). Lithographic processes were optimized in collaboration with Drs. A. Gerardino and E. Giovine at the CNR - IFN to fabricate PMA-SAF microdisks.

2.2.1. **Magnetron sputtering deposition technique**

Magnetron sputtering is a well-established technology to grow high-quality thin films and multi-layered heterostructures. Sputtering is a vacuum process performed by applying a high voltage across a low-pressure Argon to create plasma, as shown in figure 2.2. The cathodes in magnetron sputtering use powerful magnets to confine the plasma to the region closest to the target. This leads to the condensed ion-space ratio, increased collision rate, and thus improved deposition rate. Electrically accelerated high energy ions (usually from an inert gas) bombard a target material, dislodging and ejecting material which then condenses onto a substrate to form a thin layer [192]. Because of the high ion energies (typically several 10 eV), almost all metals and metallic alloys can be readily sputtered at a relatively high deposition rate (10 Å s^{-1}). The large thickness homogeneity over several cm's makes sputtering also a flexible, frequently employed, industrial fabrication technique. Whilst the higher deposition energies lead to flat multilayers with few grain boundaries or pinholes on a µm scale, this must be weighed against the inter-diffusion created at the interfaces (nm scale). Sputter process parameters such as sputter pressure, sputtering energy and inert gas element can be varied to modify the structure [193].

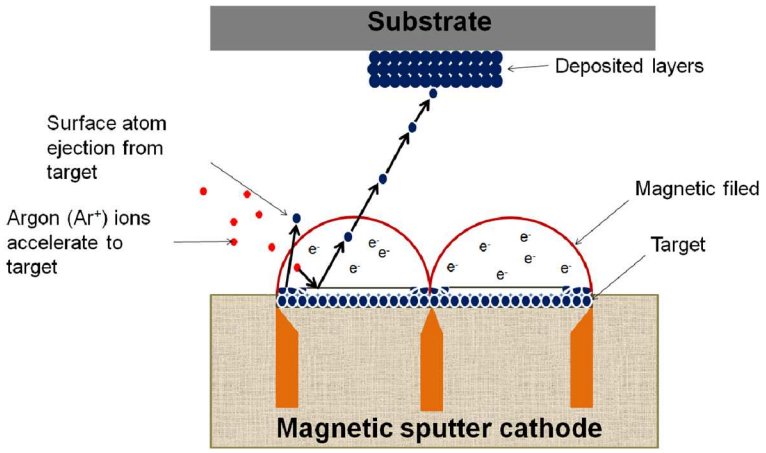

Figure 2.2. Magnetron sputtering. The powerful magnets, connected to the cathodes, confine the plasma to the regions closest to the target (adapted from Ref.[194]).

The samples studied in this PhD thesis were deposited by using a BESTEC magnetron sputtering system (Figure 2.3). The sputtering chamber (700 mm diameter, 850 height) is equipped with eight 2-inch magnetrons with easy changeable magnetic system for use with ferromagnetic or non-ferromagnetic target materials and a rotating sample holder to improve sample uniformity. Different sample sizes from 4-inch wafer down to 10mm x 10mm samples can be handled (using different kind of sample adapters). A thickness sensor setup with manual translation stage for sputter rate check before deposition is also available in addition to an ion source for sample pre-cleaning and mild etching and a residual gas analysis installed at the sputtering chamber. The equipment is also characterized by a fully motorized 2 axes sample manipulator with integrated motorized wedge shutter, DC bias potential option and maximal sample temperature above 800°C. All sources can be driven with DC or RF generators. Each source has its own gas inlet close to the target and source shutter included. Typically, full software control incl. automatic deposition process. A load-lock chamber (200 mm diameter, 300 mm height) with a carousel of 5 sample holder and

with a pressure as low as 6.0×10^{-7} Torr is used to minimize the gap time to break the high vacuum and hence to secure the main chamber vacuum and to fast the deposition processes (up to 10 runs per days at room temperature). A base pressure as low as 5.0×10^{-9} Torr is achieved in the main chamber, thus allowing to grow thin film multistacks with minimal interfacial oxidation and H_2O contamination, which is necessary in engineering magnetoresistive stacks with improved GMR.

Figure 2.3. UHV sputter deposition system

2.2.2. **Lithographic techniques**

Lithographic techniques including electron beam lithography (EBL) and the ion etching process were used for the preparation of PMA-SAF microdisks.

As explained in detail in the next sections, electron beam lithography was used both in the top-down and bottom-up approaches to expose the resist and create pre-patterned arrays of circular dots. Reactive ion etching processes were used in the top-down approach, in combination with EBL, to etch the magnetic film and obtain an array of microdisks.

Electron beam lithography EBL

Electron beam lithography (EBL) is one of the key fabrication techniques that allows creating patterns at the micro and nanoscale. EBL is characterized by its ability to register accurately over small areas of a wafer and by its lower defect densities. The main drawbacks of electron beam lithography are low throughput and high capital cost. The development of EBL tools started in the late 1960s [195] by changing the design of scanning electron microscopes (SEMs). It is a method of exposing an electron sensitive resist using a highly focused e–beam where a pattern can be transferred from a computer design to a pattern generator in order to expose the desired pattern. The e–beam is scanned in a raster fashion to transfer the desired pattern by using an exciting signal applied to deflection coils. The use of e–beam lithography combined with an electron sensitive resist ensures higher spatial resolution in the exposure step of lithography. The e–beam modifies the electronic structure of the resist via ionization; thus, areas exposed or not exposed, according to the tone of the resist, are removed by developing.

As shown in figure 2.4, an EBL apparatus is schematically made up of a chamber, an electron gun, and a column. Columns and chambers are maintained in high vacuum by a suitable set of pumps. The column contains all the electron optical elements needed to create a beam of electrons, to accelerate it to the working voltage, to turn it on and off, to focus, and to deflect it as required by the pattern to be written. The samples are normally loaded via a load-lock into the main chamber and are typically placed on an interferometric stage for accurate positioning of the working piece. The

computing system, the pattern generator, the operator interface, and all the electronics needed to control and operate the machine are not shown in figure 2.4.
The EBL system used in this study is a Raith-Vistec EBPG 5HR working at 100kV (spot diameter 8 nm; positioning accuracy 20nm) (figure 2.5a).

Reactive Ion Etching

Reactive Ion Etching (RIE) is a synergistic process between chemically active species and energetic ion bombardment where radiofrequency (RF) discharge-excited species (radicals, ions) etch substrate or thin films in a low-pressure chamber. It is faster than both pure physical ion bombardment and spontaneous chemical etching. Because ion bombardment is directional, RIE has anisotropic character, with reduced lateral etch rate and vertical (or nearly vertical) sidewalls. RIE is essential when narrow lines or channels are needed, or when high aspect ratio structures need to be fabricated [196]. Generally, reactive ion etching processes are used in combination with other lithographic techniques to obtain micro/nano-patterned arrays by film/substrate erosion.

This equipment used in this PhD thesis is a reactive ion etching with an inductively coupled plasma source (ICP). The main difference with a conventional RIE is the separation between the source producing the excited gas (plasma) and the sample bias, realized with a conventional planar diode configuration. The gases used in this system are: CF_4, SF_6, CHF_3, O_2, Ar. The source can produce plasma densities much higher (a factor 100) with respect to the conventional configuration and this leads to a higher etching rate. Materials that can be etched in the system are: silicon, silicon oxide, silicon nitride, titanium, niobium. In particular, an Argon-ion-milling based process was used in our study with a power of 300 W and bias of 400 V for tens of seconds.

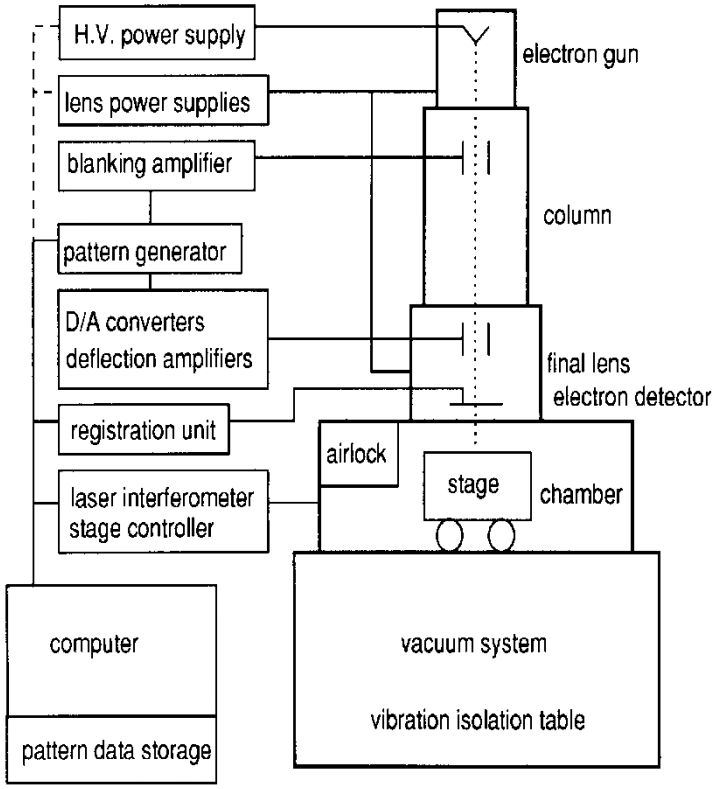

Figure 2.4. A typical EBL system, consisting of a chamber, an electron gun, a column containing all the electron optics needed to focus, scan, and turn on or turn off the electron beam.

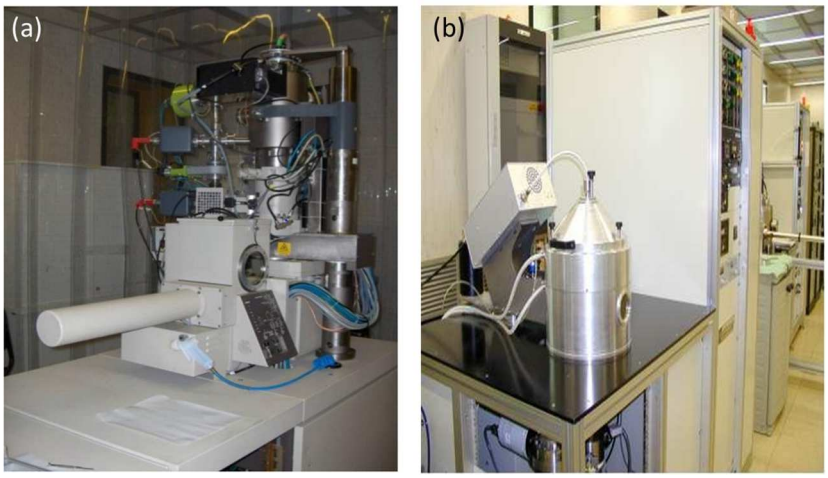

Figure 2.5. (a) A Raith-Vistec EBPG 5HR used for the EBL processes and (b) reactive ion etching equipment with an ICP source.

2.2.3. GMR spin valves on flexible substrates - Experimental conditions

All samples were DC sputter deposited at room temperature and at an Ar working pressure of 3.5 μbar by using metallic targets of the individual components. The targets were pre-sputtered to remove surface contaminants and ensure uniform deposition of material. The deposition rates of each material were set to the values reported in table 2.1 to promote the growth of high quality thin film multistacks with smooth interfaces. Reference samples were first grown on conventional thermally oxidized Si (100) substrate. The layer stack sequence and properties (i.e. type of underlayer, single layers' thickness, bilayer repetition N) were varied with the aim to ensure (i) a PMA along the full layer stack, (ii) a strong and compensated antiferromagnetic coupling in the SAF structure, and (iii) two stable parallel/antiparallel magnetization configurations in the spin-valve system.

As concerns the Co/Pd-based systems, $[Co/Pd]_N/Ru/[Co/Pd]_N$ synthetic antiferromagnetic thin film stacks were deposited changing the Co layer thickness (from 0.3 to 0.4 nm), the number of bilayers N (from 4 to 8) and the Ru spacer thickness (from 0.3 to 0.5 nm, i.e. around the first peak of oscillation), while the Pd thickness was set to 0.9 nm as widely reported in the literature [18,197,198]. The optimized SAF thin film stack was combined to a Co/Pd multilayer (the free layer) through a Cu spacer with a variable thickness ranging from 2 to 5 nm to prepare GMR-SVs with perpendicular magnetic anisotropy (figure 2.6). For all the samples, a Ta(3)/Pd(2.1) buffer layer (thicknesses in nm) was used to improve the adhesion and induce a (111) crystallographic texture, which is required to obtain large perpendicular magnetic anisotropy [180,181]. A Pd(2.1) capping layer was deposited on top to prevent the free layer oxidation. Moreover, the Ru spacer was sandwiched between the Co layers with the aim to increase the exchange coupling [199].

Table 2.1. Sputtering conditions of materials used in this work

Samples	Sputtered Material	Deposition Rate nm/s	Power (W)
Co/Pd-based samples	Ta	0.03	40
	Pd	0.04	26
	Co	0.025	52
	Au	0.067	24
	Ru	0.03	48
	Cu	0.035	25
Co/Ni-based samples	Ta	0.03	40
	Pd	0.04	26
	Co	0.025	52
	Ni	0.02	35
	Ru	0.025	49
	Cu	0.04	29
	Pt	0.05	37

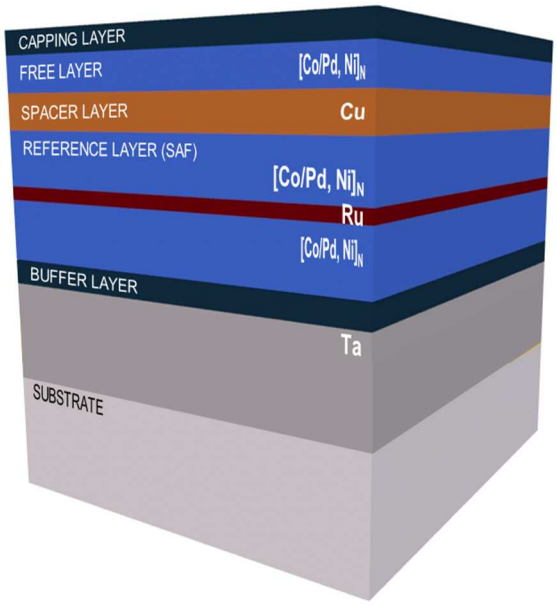

Figure 2.6. Sketch diagram illustrating the [Co/Pd, Ni]-based GMR spin valve multistack with a SAF reference layer.

Co/Ni-based thin film SAF stacks with a $[Co/Ni]_N/Ru/[Co/Ni]_N$ structure were grown on different buffer layers (Ta/Pd, Cu) by varying the number of bilayers N (from 4 to 6) and the Ni layer thickness (from 0.5 to 0.8 nm). The Ru thickness was selected on the basis of the results obtained for the Co/Pd system, while the Co layer thickness was set to 0.2 nm as widely reported in the literature [16,17,200]. The optimized SAF thin film stack was combined with a Co/Ni multilayer (the free layer) through a Cu spacer with thickness of 3 nm to prepare GMR-SVs with perpendicular magnetic anisotropy (figure 2.6). The effect of different buffer (Ta/Pd, Cu) and capping (Pd, Cu/Ta) layers on the SVs properties was also investigated. After optimizing the material properties of the reference samples on rigid SiO_2/Si (100) substrates, flexible

SAF and GMR-SV thin film stacks with perpendicular magnetic anisotropy were obtained by direct deposition on flexible substrates and by using transfer-and-bonding approaches. In the direct deposition strategies, flexible Teonex® tapes and freshly-cleaved muscovite MICA sheets were used to deposit the multistacks on. Muscovite mica is a widely used material because of its transparency, heat resistance and especially its flatness. On the other hand, Teonex® tapes, consisting of a PEN foil with a flattening coating offer a unique combination of excellent dimensional stability, low moisture pickup, good solvent resistance, high clarity and very good surface smoothness (average roughness < 0.7 nm). This combination makes Teonex® a promising substrate for subsequent vacuum and other coating processes, leading to the potential use of this material as a flexible substrate for device manufacture. As concern the transfer and bonding approaches, three different strategies were investigated: (i) w*et etching lift-off* via a polymethylmethacrylate (PMMA) sacrificial polymer layers, (ii) w*et etching lift-off* using KBr (100) sacrificial substrates and (iii) *dry etching lift-off* exploiting the low adhesion of Au metal under layers. The main characteristics as well as the advantages and drawbacks, as inferred from the data reported in the literature, are summarized in table 2.2, while the details of each strategy are discussed below.

Table 2.2. Main advantages and drawbacks of selected strategies for the fabrication of flexible electronics.

	Advantages	Drawbacks
Direct deposition on flexible substrates		
MICA	– Low cost one-step fabrication processes – High processing temperatures (up to ∼1200 K for fluorophlogopite mica) – Van der Waals epitaxial growth	– Lower mechanical flexibility compared to polymer tapes
Teonex® tape PEN films with a flattening coating (R_a < 0.7 nm)	– Low cost one-step fabrication processes – Large surface area coverage	– Amorphous substrate – Low processing temperatures (< 550 K)
Transfer & Bonding		
Wet etching lift-off		
Sacrificial salt substrates KBr (100)	– Crystalline material – High processing temperatures (up to ~ 1000 K) – Arbitrary flexible tapes can be used	– Small surface area coverage – Complex and costly fabrication processes
Sacrificial polymer layers Polymethylmethacrylate (PMMA)	– Arbitrary flexible tapes can be used – Lower fabrication costs compared to salt substrates	– Complex fabrication processes – Amorphous material – Low processing temperature (< 460 K)
Dry etching lift-off		
Low adhesion metal layers Au on SiO_2/Si(100)	– Crystalline material – High processing temperatures – Arbitrary flexible tapes can be used	– Small surface area coverage – Complex fabrication processes

- *Direct deposition on flexible mica substrates.* Flexible muscovite MICA sheets were obtained from natural muscovite (Nilaco Corporation) by gently separating the natural layers in the MICA using a thin double edged razor blade. Freshly cleaved MICA sheets were immediately introduced in the vacuum chamber to avoid any surface contamination.
- *Direct deposition on flexible Teonex® tapes*. Teonex® flexible tapes consisting of a 125 µm thick polyethylene naphthalate (PEN) film covered with a flattening coating (surface roughness R_a < 0. 7 nm) were purchased from *Teijin* corporation and used as it.
- *Wet etching lift-off - PMMA sacrificial layers*. Polymethylmethacrylate (PMMA) sacrificial layers were spin coated on a thermally oxidized Si (100) substrates. After depositing the multistacks, a Kapton adhesive tape was attached to the sample surface and the whole structure was then immersed in an acetone bath for a few seconds to allow the dissolution of the PMMA sacrificial layer. In the final step, the Si/SiO_2 rigid substrate is gently separated by using a tweezer.
- *Wet etching lift-off - KBr (100) sacrificial substrates*. KBr substrates were obtained by cleavage of KBr (100) single crystal cubes (MSE Supplies) using a thin double edged razor blade. Freshly cleaved KBr substrates were immediately introduced in the vacuum chamber to avoid any surface modification due to the absorption of water. After depositing the multistacks, a Kapton adhesive tape was attached to the sample surface and the whole structure was then immersed in a water bath to dissolve the KBr substrate and finally obtain the flexible GMR spin valve.
- *Dry etching lift-off - low adhesion Au metal buffer layers*. 10 nm thick Au buffer layers were deposited on thermally oxidized Si substrates prior the deposition of the multi-stack. Owing to the low adhesion of Au on SiO_2 [201,202], the multi-stacks were easily peeled and transferred from the substrate to a flexible tape by using a commercial adhesive polyester tape (3M 396). To favor the peeling process, a cellulose acetate butyrate-based

paint was spread over the surface sample to allow a better adhesion between the film and the tape (figures 2.7).

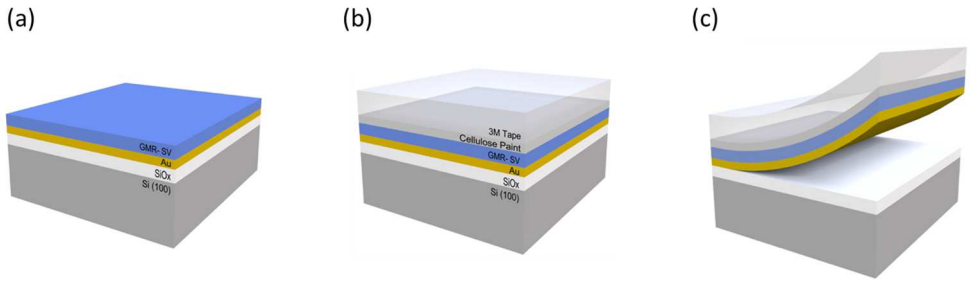

Figure 2.7. Sketch of the proposed Au-mediated *transfer-and-bond* approach. (a) PMA-GMR spin valves are DC sputtered on a SiO_2/Si (100) substrate covered with a weakly adhering Au layer; (b) a cellulose paint is spread over the film surface to improve the adhesion between the sample and the adhesive tape on which the multistack is transferred by a mechanical peel-off step (c).

2.2.4. **PMA SAF microdisks - Experimental conditions**

Co/Pd-based SAF microdisks were prepared by using both top-down and bottom-up EBL strategies. In the top-down approach, continuous Co/Pd-SAF thin film stacks were first deposited on a proper substrate and a combination of EBL and ion etching processes were used for the fabrication of the microdisks. In the bottom-up approach, pre-patterned substrates consisting of arrays of microholes were first prepared combining EBL and lift-off strategies, then, the Co/Pd-SAF thin film stacks were deposited inside the holes and the microdisks were finally obtained exploiting lift-off processes. The activity was mainly focused on the study and optimization of the properties of the continuous thin film stacks consisting of multiple repetitions of single PMA-SAF units grown on a sacrificial resist layer previously spin-coated on SiO_2/Si (100) substrates, which allows for the preparation of free-standing disks after its dissolution. Thin film stacks were

sandwiched between Au layers, which can be easily functionalized with biological molecules. After optimizing the properties of the continuous films on a resist layers, microdisks were prepared by using both EBL bottom-up and top-down approaches.

EBL top-down approach

$\{Ta/Pd/[Pd/Co]_N/Ru/[Co/Pd]_N\}_M$ thin films consisting of multiple repeats (M = 1, 3, 5, 6, 8) of single $[Co/Pd]_N/Ru/[Co/Pd]_N$ SAF units (Figure 2.8) were deposited at room temperature onto a sacrificial optical resist layer (AZ5214, thickness: 1.5 mm) previously spin-coated at 3000 rpm on a thermally oxidized Si(100) wafer. A Ta(3 nm)/Pd(2.1 nm) buffer layer was used either to improve the adhesion and the surface morphology or to induce the (111) crystallographic orientation, which is required to obtain large perpendicular magnetic anisotropy [203,204]. To decouple consecutive units, the Ta(3 nm)/Pd(2.1 nm) buffer layer was also included for each repeated single SAF stack [205]. However, as the presence of non-magnetic spacers, for a given volume, reduces the effective magnetic moment of the system, differently to previous papers, N values larger than one were explored in order to ensure a high magnetic moment of the single SAF unit and limit the number of the non-magnetic spacers. To demonstrate the possibility of further surface functionalization, a 10 nm Au layer was deposited both on the bottom (i.e., after the resist) and on the top of the layer stack. All samples were sputter-deposited at room temperature at an Ar pressure of 3.5 μbar. The deposition rates of each material used are the same as reported in table 2.1.

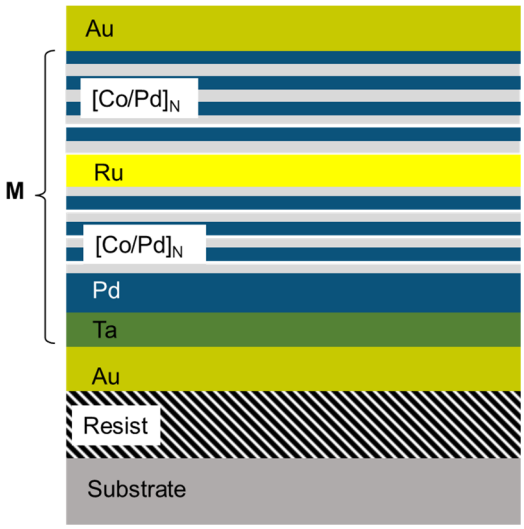

Figure 2.8. Schematic structure of the film samples consisting of multiple repetitions (M) of single $[Co/Pd]_N/Ru/[Co/Pd]_N$ SAF units.

After optimizing the thin film stack, PMA-SAF microdisks were prepared by spin-coating a negative ARN7700 mask resist on top of the film stack then exposing it using EBL at 100 KV to create patterned circular dots with a diameter of 2 µm each and a pitch of 4 µm. After exposure, the resist was developed to etch the exposed regions. Finally, Ar ion milling at 300 W power and a bias of 400 V for about 140 seconds was performed to do the lift-off process by etching the magnetic film and thus obtain an array of microdisks (area up to 5 × 5 mm^2). As the final step, a free standing micordisks can be obtained by dissolving the sacrificial resist layer in acetone. The process is illustrated in figure 2.9.

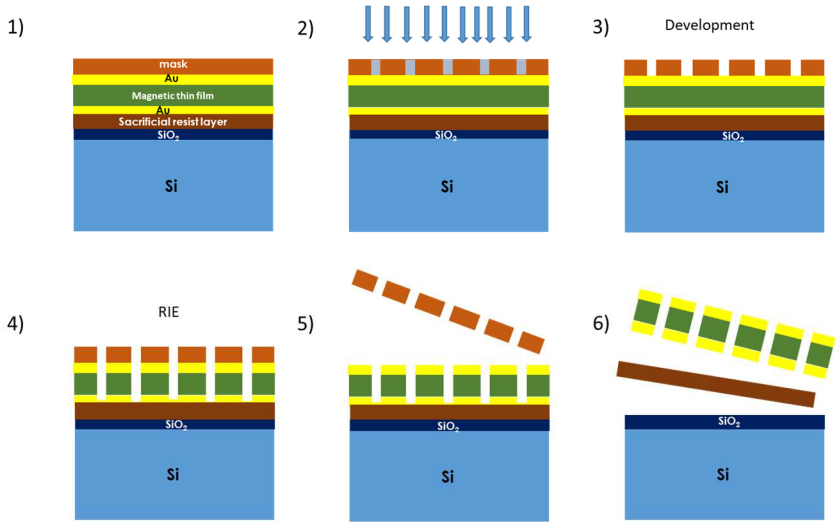

Figure 2.9. A schematic diagram illustrating the EBL process for the fabrication of microdisks by a top-down approach: 1) sputter deposition of the SAF thin film stack and mask spinning (top and bottom Au layer for functionalization), 2) EBL exposure, 3) Development to remove the exposed mask, 4) RIE to etch the unmasked film, 5) mask removal, 6) sacrificial resist layer dissolution to obtain free standing microdiscks.

EBL bottom-up approach

As an alternative to top-down approaches, pre-patterned substrates consisting of an array of microholes were prepared by combining EBL and lift-off strategies, to deposit the Au/{Ta/Pd/$[Pd/Co]_N$/Ru/$[Co/Pd]_N\}_M$/Au (M = 1, 3 and 5) SAF thin film stacks inside. To this aim, a PMMA 669.06/COP 8.5 EL6/LOR B (7B) resists' stack consisting of three different resist layers with distinct functions was spin-coated and baked on Si substrates under the conditions reported in table 2.3. LOR B (Lift-off resist B which is based on polydimethylglutarimide PMGI) was used as a sacrificial resist layer while the dual resists COP (Cyclo Olefin Polymer) and PMMA (Poly methyl methacrylate) were used to get a better undercut which is essential to

achieve a good lift-off [206]. It is worth mentioning that the LOR B sacrificial layer is expected to have similar surface properties of the AZ5214 optical resist, thus affecting in a simlar way the properties of the multi-stacks deposited on top. Arrays of circular dots with pitches of 1 and 4 µm and dot diameter of 1 µm were then created on the resists by exposing them using EBL. The resists were then developed and etched in MIBK (Methyl isobutyl ketone): IPA = 3:1; thus; creating patterned hole arrays with pitches of 1 and 4 µm and hole diameter of 1 µm. After depositing the Multi-SAF stacks on the pre-patterned substrates, the microdisks arrays were obtained by performing lift-off in acetone to remove the PMMA with the continuous film on top. As the final step, free standing micordisks can be obtained by dissolving the sacrificial resist LOR B in PG remover (an NMP-Nmethylpyrrolidone based solvent). The process is schematically illustrated in figure 2.10.

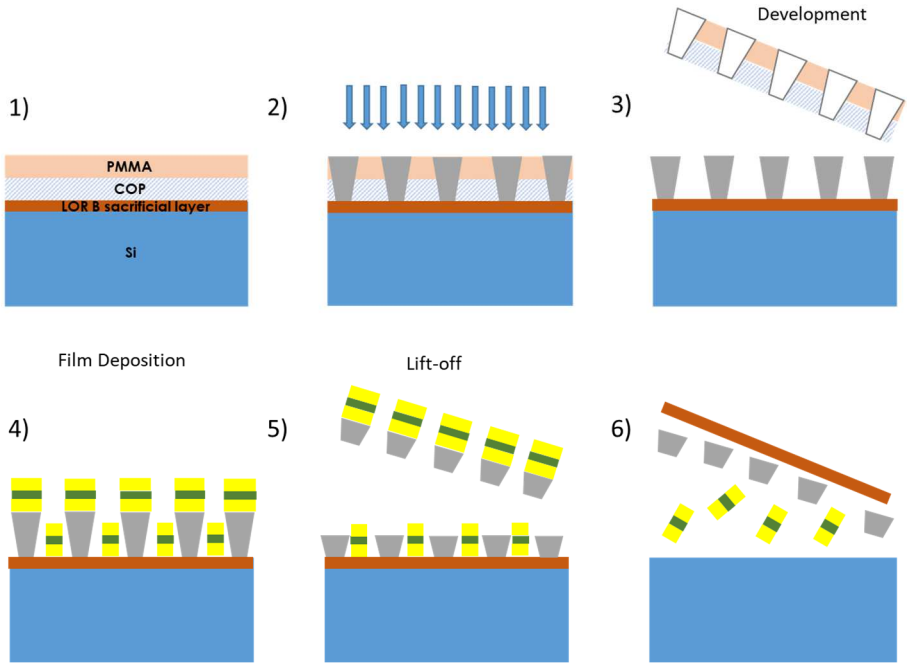

Figure 2.10. A schematic diagram illustrating the EBL process for the fabrication of microdisks by a bottom-up approach: 1) spin-coating of resists on Si substrate, 2) EBL exposure of the resists, 3) development of the resists, 4) sputter deposition of the SAF thin film stack (top and bottom Au layer for functionalization), 5) lift-off in acetone to remove the dual resists between the SAF stacks, 6) sacrificial resist layer dissolution to obtain free standing microdisks.

Table 2.3. Experimental conditions used for the resists preparation (spinning and baking).

Resist name	Spinning speed (rpm)	Time of spinning (s)	Baking temperature (°C)	Baking time (min)
LOR B (7B)	4000	45	170	5
PMMA 669.06	3000	60	170	5
COP 8.5 EL6	3000	60	170	5

2.3. Characterization

2.3.1. Microstructural properties

Microstructural and morphological investigations were performed by Scanning (SEM) and Transmission (TEM) Electron Microscopy at the Department of Materials, Environmental Sciences and Urban Planning (SIMAU) - Università Politecnica delle Marche.

SEM Microscopy

Scanning electron microscope (SEM) is one of the most versatile instruments available for the examination and analysis of the surficial morphology of a sample in a large range of dimensions (from cm to nm) using secondary electrons, and of the surficial chemical composition using backscattered electrons [207]. SEM is a powerful tool that utilizes the extremely small wavelengths of accelerated electrons to reduce the electron beam at the sample surface and so to resolve features down to the nanometer scale. When an accelerated electron beam strikes a sample, several signals including secondary electrons, backscattered electrons, transmitted electrons, X-rays, Auger electrons and cathodoluminescence are generated; thus allowing to obtain information on the topography, morphology, composition and crystallography. In general, a SEM is very close to the typical EBL system. The main difference between a SEM and an EBL is that in an EBL the beam is scanned onto the sample following the instructions coming from the pattern generator, while in a SEM the beam is raster scanned over the sample so that secondary electrons are collected to form an image. In this work a SEM PHILIPS XL20 (maximum voltage 30 KV) microscope was used to image the magnetoresistive structures deposited by DC sputtering through the detection of secondary electrons (figure 2.11). The instrumentation allows the observation of the three-dimensional

topography of the sample with the possibility of obtaining compositional information and images. All kinds of samples can be observed as long as they are stable under vacuum and conductive or made conductive with appropriate preparation techniques.

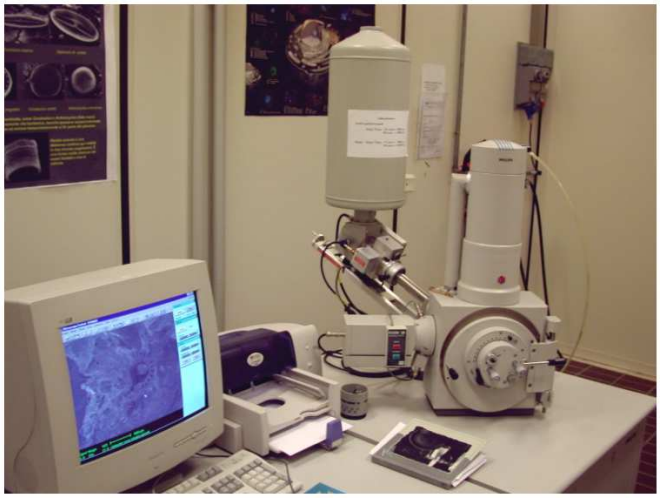

Figure 2.11. SEM PHILIPS XL20 used for SEM characterization during this work.

TEM Microscopy

Transmission electron microscopy (TEM) is a technique useful in obtaining morphological and structural information which are not limited to the samples surface [208]. TEM allows to investigate the inner structure of the materials at atomic resolution as well as to investigate the presence of lattice defects (precipitates, dislocations, twins, etc.) that could be detrimental for specific applications. The crystallographic structure of samples can be investigated by using electron diffraction analysis which combined with imaging formation allows to obtain very localized information.

A TEM consists of an electron gun able to produce a high energy electron beam. Electrons are the analog of photons inside an optical microscope, they are used to illuminate the sample and to obtain a magnified image by using

magnetic lenses instead of glass lenses. In particular, condenser lenses direct the electron beam on the sample obtaining a uniform “illumination” (parallel electron beam), and an objective lens forms the image of the sample on the image plane and the diffraction pattern in the back focal plane. Intermediate lenses are used to obtain a magnified image of the image plane or of the back focal plane that determine whether an image or a diffraction pattern is formed on the final screen. The image of the sample is formed by taking the electrons passing through the sample, so the sample must be very thin to be electrons transparent. If only the forward transmitted electrons (no scattering inside the sample) are used to form the sample image, a bright field image is obtained, if instead only one of the diffracted beams (scattered electrons) is used a dark field image is achieved. By using a selecting area diaphragm, one part of the sample may be selected and only the diffraction pattern coming for that specific region can be imaged. If the aperture is small enough the diffraction pattern from a single crystal may be obtained. By using selected area diffraction (SAED), it is possible to obtain the crystalline structure and symmetry of the lattice in a crystalline sample.

The multilayer structure, interfacial microstructure and selected area diffraction (SAED) pattern of the deposited films were characterized in this work using a Philips CM200 microscope (200 kV) (figure 2.12). The instrument allows the observation of the internal structure of the samples even in high resolution conditions and with the possibility of performing localized compositional analyzes. All types of samples can be observed as long as they are stable under vacuum and transparent to the electrons of the incident beam or made transparent by appropriate thinning techniques: TEM samples were prepared using a conventional thinning procedure consisting of mechanical polishing by grinding papers, diamond pastes, and a dimple grinder. Final thinning was carried out by an ion beam system (Gatan PIPS) using Ar ions at 5 kV.

Figure 2.12. A Philips CM200 microscope used for TEM characterization during this PhD thesis.

X-Ray Reflectivity

Investigation techniques based on X-ray scattering are largely used for material characterization at the nanoscale [209,210]. X-rays are electromagnetic waves with a wavelength of around one angstrom (10^{-10} m), hence particularly useful for investigating structures such as atoms, molecules, and crystals. As X-rays are scattered by single electrons, atoms, molecules, and crystals, penetration inside matter depends on the material density as well as on the angle (θ) that the incident X-ray beam forms with the sample surface. At grazing incidence (θ = 0.4°–5°), penetration is limited to near-surface regions so that the surface structure of materials can be easily investigated.

To investigate surface roughness of our multilayer system, X-ray reflectivity (XRR) was used in this thesis. As XRR is based on radiation reflection at surfaces and interfaces, the technique estimates the roughness, thickness, and density of a single layer or multiple layers independently of

sample crystallinity. A Leptos software was used to estimate values like the thickness (t), roughness (σ) and density (ρ) values of each layer from the XRR data fitting.

2.3.2. **Magnetic properties**

Room temperature magnetization *M* vs magnetic field H (*M-H*) loops were measured by using both superconductive interference device – vibrating sample magnetometer (SQUID-VSM, LOT-Quantum Design, MPMS3) and VSM (Microsense, Model 10) with the magnetic field applied either along the film normal or along the film plane.

The VSM Magnetometer

The Vibrating Sample Magnetometer (VSM) is the basic instrument for characterizing magnetic materials. Since its invention [211,212], it has become the workhorse in both laboratory and production environments for measuring the basic magnetic properties of materials as a function of magnetic field and temperature.

The basic instrument is shown in figure 2.13. The sample (5) is vibrated perpendicularly to the applied field by the loudspeaker assembly (1), (2) and (4). The oscillating magnetic field of the vibrating sample induces a voltage in the stationary detection coils (7), and from measurements of this voltage the magnetic properties of the sample are deduced. A second voltage is induced in a similar stationary set of reference coils (6) by a reference sample (4) which may be a small permanent magnet or an electromagnet. Since the sample and the reference are driven synchronously by a common member, the phase and the amplitude of the resulting voltages are directly related. The known portion of the voltage from (6) phased to balance the voltage from (7), is then proportional to the magnetic moment of the sample. By this procedure, the measurements can be made insensitive to

changes of vibration amplitude, vibration frequency, small magnetic field instability, and amplifier gain.

Our experimental apparatus is a Model 10 Microsense VSM magnetometer (Figure 2.14). It is equipped with a rotating (from 0 to 360 ^{o}) electromagnet that can generate a maximum field of 20 KOe, measured by a Hall-effect device in a computer-controlled feedback loop. The minimum detectable signal is about 20 μemu. The magnetic signal is detected by 8 coils, forming 4 pairs of two coils each (figure 2.15). A pair of coils consists of two coils mounted one above the other. Two pairs of coils facing (parallel to) each other are connected together to measure the signal in one direction. The other two pairs, which are mounted orthogonal (at 90 ^{o}C) to the first two pairs, measure the magnetic signal in the direction perpendicular to the first direction.

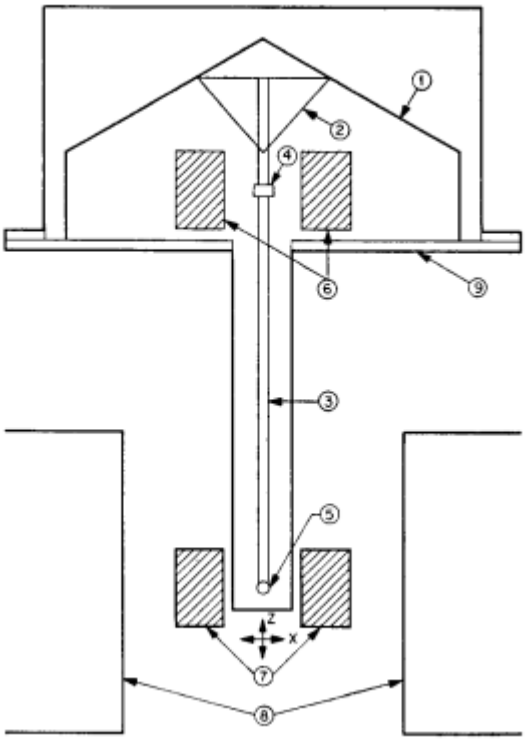

Figure 2.13. Simplified form of the vibrating sample magnetometer. (1) loudspeakers transducer, (2) conical paper cup support, (3) drinking straw, (4) reference sample, (5) sample, (6) reference coils, (7) sample coils, (8) magnet poles, (9) metal container (adapted from Ref.[213]).

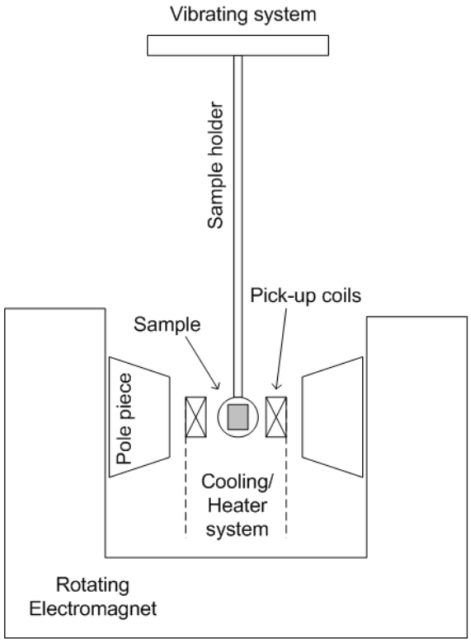

Figure 2.14. Main components of the Model 10 EDA-Technologies VSM magnetometer.

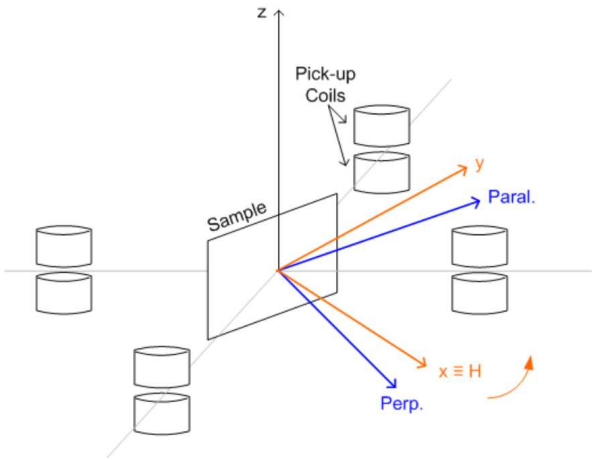

Figure 2.15. Scheme of the geometric setup.

The sample to be measured is attached (using clean double-sided tape or vacuum grease) to the small flat disk at one end of the Pyrex sample holder. The other end of the sample holder is inserted into the vibrator. Variable temperatures, ranging from 100 K to 780 K are achieved in a continuous fashion (single system) and without the need to switch from a cryostat to a high-temperature module. A computer workstation is equipped with a LabView software which allows the user to calibrate the system, control the operation of the VSM and collect and analyze the resulting data.

The SQUID-VSM Magnetometry

A part of the magnetic measurements was performed at the Institute of Physics, University of Augsburg (Germany), in the labs of Prof. M. Albercht, using a SQUID-VSM. In the SQUID-VSM the magnetic moment is measured by vibrating the sample in the z-direction. In figure 2.16 the layout of the apparatus is shown. Recalling the basis of a VSM, the VSM works by vertically vibrating the sample. If it has a magnetic moment this will cause a flux in the detection coils. The induced current is proportional to the magnetic moment of the sample. Four pick up coils are used in a so-called second-order gradiometer (which removes the zeroth and first spatial derivative of the magnetic field) to improve the sensitivity of the technique. The coils are inductively coupled to a SQUID sensor, which allows for a very sensitive measurement of the variation of the current in the coils and so of the magnetization of the sample. The SQUID consists of one superconducting ring with two insulating interruptions. These are the Josephson junctions which cause a "weak link" in the ring implying that the ring will remain superconducting only for currents below some critical I_c. The magnetic flux in the ring is quantized by Φ_0. When a flux is induced in the ring a screening current is generated in order to keep the total flux a multiple of Φ_0. By increasing the applied flux, the screening current and thus the voltage of the system will oscillate. Counting the number of oscillations indicates how

many quanta have been added. As Φ_0 is very small the applied flux can be measured very precisely [214].

In our setup, a MPMS SQUID VSM from LOT-Quantum Design including an oven module is used. In this VSM magnetic moments could be determined with an accuracy of 2 x 10^{-8} emu and temperatures up to 1000 K could be reached. Magnetic fields up to 7 T could be applied.

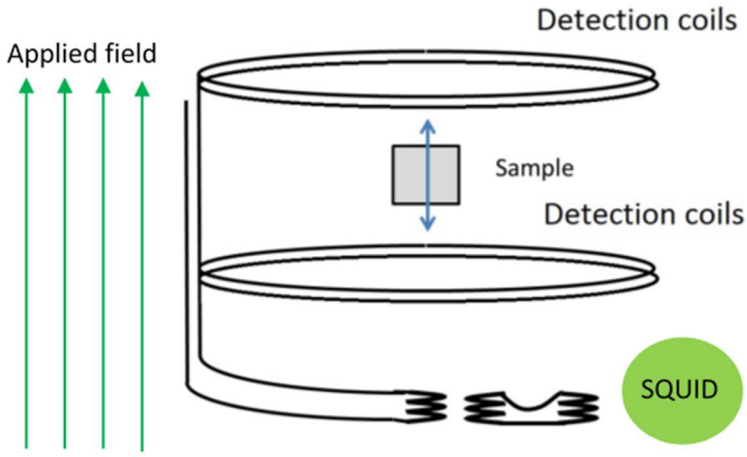

Figure 2.16. Layout of the VSM-SQUID. The sample is vibrated in a direction normal to the detection coils and parallel to the applied field. The detection coils are built in a second order gradiometer and are inductively coupled to the SQUID detector (adapted from Ref.[215]).

2.3.3. **Magneto-transport properties**

Magneto-transport properties of the spin valve thin films were performed at room temperature, in collaboration with Dr. C. Rinaldi and Dr. F. Fagiani of the Polytechnic University of Milano, employing the Van der Pauw method (VDP) [216]. The Van Der Pauw method is a pervasive technique to measure the resistance of planar homogeneous samples with four contacts placed on its periphery, without patterning. Measurements were performed

on square-shaped samples at the four contacts (*1*,*2*,*3*,*4*) made by silver paste on top of the surface at each corner of the sample. The currents in the order of 10 mA were injected using a Keithley 6221 current source in a couple of contacts along one side of the sample (e.g. from *1* to *2*) while the voltages were measured by a Keithley 2182A nanovoltmeter between the opposite contacts (e.g. *3* and *4, see the sketch of figure 2.17)*. We adopted the "full" VDP method, measuring current-voltage characteristics automatically at four different source-measure configurations (12-43, 23-14, 34-21, 41-32) to compensate for possible asymmetries and non-idealities. This was achieved using a custom-designed switching network board, following the scheme of Ref. [217]. Noteworthy, the homogeneity of our samples and the repeatability of the result have been widely tested by measuring at least two samples for each kind of heterostructure, and verifying the uniformity by comparing different sample sizes/spacing between the four contacts (from 2x2 cm down to 2x2 mm). The magnetic field was provided by a standard dipole electromagnet by GMW Associates. For measurements under bending conditions, samples were mounted on a semi-cylindrical plastic support with the proper radius of curvature (see figure 2.18).

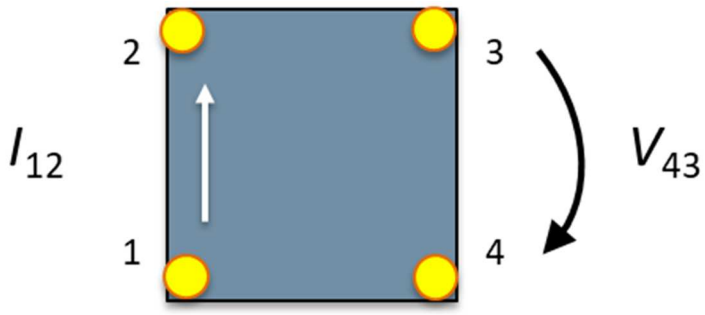

Figure 2.17. 4-point probe Van der Pauw method used for the measurement of magneto-transport properties in the GMR SV samples.

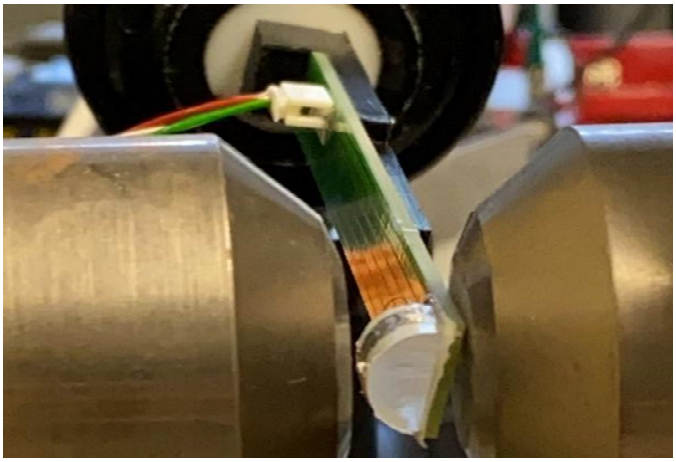

Figure 2.18. Experimental setup used for magneto-resistive measurements of flexible GMR-SVs with PMA under bending conditions.

Chapter 3.

Perpendicularly magnetized Co/Pd SAF-based GMR spin valves on flexible substrates

This chapter reports on flexible Co/Pd-based GMR spin-valve thin films with perpendicular magnetic anisotropy consisting of a $[Co/Pd]_N$ free layer and a fully compensated $[Co/Pd]_N/Ru/[Co/Pd]_N$ synthetic antiferromagnet reference layer (SAF-RL) separated by a Cu spacer. Different strategies including transfer-and-bonding approaches exploiting wet and dry lift-off methods and direct deposition on flexible substrates were investigated. Magnetic, magneto-resistive and morphological properties as well as measurements under bending conditions were performed.

3.1. Co/Pd-based SAF thin film stacks

3.1.1. Reference Co/Pd-based SAF thin film stacks on SiO_2/Si (100) substrates

$[Pd/Co]_N/Ru/[Co/Pd]_N$ thin film stacks with variable Co layer thickness (t_{Co}), bilayer repetition number (N) and Ru spacer thickness (t_{Ru}) were sputtered on SiO_2/Si (100) substrates in order to optimize the magnetic properties of the SAF building block. The Pd thickness was set to 0.9 nm throughout this study.

To maximize the antiferromagnetic coupling, t_{Co} and N were set to 0.4 nm and 6, respectively, while the thickness of the Ru spacer was varied from

0.3 nm to 0.5 nm, i.e. around the first peak of the oscillation where we expect the strongest antiferromagnetic coupling [6], which would result in a wider AF-coupled plateau and, as a consequence, in a higher stability of the systems against external magnetic fields. Figure 3.1a shows room temperature out-of-plane field-dependent magnetization loops of $[Co/Pd]_6/Ru/[Co/Pd]_6$ thin film stacks as a function of the Ru layer thickness (t_{Ru}). A squared hysteresis loop with a single reversal step is observed for t_{Ru} = 0.3 nm, thus indicating ferromagnetic coupling between the two Co/Pd multilayers. By increasing t_{Ru} up to 0.4 nm, the formation of a fully compensated SAF stack is achieved. The SAF stack exhibits clear PMA as confirmed by comparing out-of-plane (Figure 3.1a) and in-plane (Figure 3.1b) *M-H* loops. The interlayer exchange coupling energy density J_{ex} was determined from $J_{ex} = \mu_o H_{ex} M_s t/2$ [15,218,219], where t is the total thickness of the Co/Pd multilayers, M_s is the saturation magnetization (~680 kA/m), and H_{ex} is the exchange coupling field defined as the field shift of the minor loop (~0.15 T, refer to figure 3.1a). A strong antiferromagnetic coupling with J_{ex} = 0.80·mJ/m^2 was calculated. Further increase of the Ru layer-thickness up to 0.5 nm leads to a reduction of J_{ex} ~0.50 mJ/m^2, which is in agreement with previous results on similar systems [6,15,220].

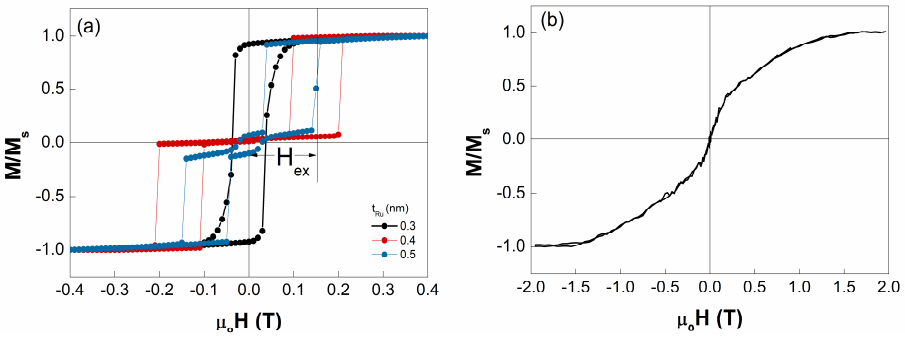

Figure 3.1. (a) Out-of-plane field-dependent magnetization loops (M/M_s vs H) of $[Co/Pd]_6/Ru(t_{Ru})/[Co/Pd]_6$ thin films deposited on SiO_2/Si (100) as a function of the Ru layer thickness (t_{Ru} = 0.3, 0.4, 0.5 nm). The exchange coupling field, H_{ex}, defined as the field shift of the minor loop, is marked for the $[Co/Pd]_6$/Ru (0.4 nm)/$[Co/Pd]_6$ sample. (b) In-plane field-dependent magnetization loops (M/M_s vs H) of the $[Co/Pd]_6$/Ru (0.4 nm)/$[Co/Pd]_6$ film. All loops were acquired at room temperature.

To explore the effect of Co layer thickness, t_{Ru} was set to 0.4 nm to maximize the antiferromagnetic coupling and t_{Co} was varied from 0.3 to 0.4 nm. Figure 3.2 shows the room temperature out-of-plane field-dependent magnetization loops of $[Co/Pd]_6/Ru/[Co/Pd]_6$ as a function of t_{Co}. All the samples show two well defined minor loops corresponding to the individual reversal of the $[Co/Pd]_6$ ferromagnetic layers separated by a wide antiferromagnetic-coupled field region with an almost zero moment in the whole field range. Reducing t_{Co} from 0.4 to 0.3 nm does not affect the saturation magnetization, which is around 680 kA/m for all the samples, while leads to a decrease of both the interlayer exchange coupling field H_{ex} (from ~160 mT to ~140 mT) and the exchange energy J_{ex} (from ~0.8 mJ/m^2 to ~0.7 mJ/m^2), and an increase of the coercivity H_c of the minor loop (from ~90 mT to ~50 mT). The reduction of the magnetostatic energy [221] and the possible increase of the magnetic anisotropy [164] while reducing the Co thickness may explain the observed increase of the minor loop coercivity and the narrowing of the AF region [199].

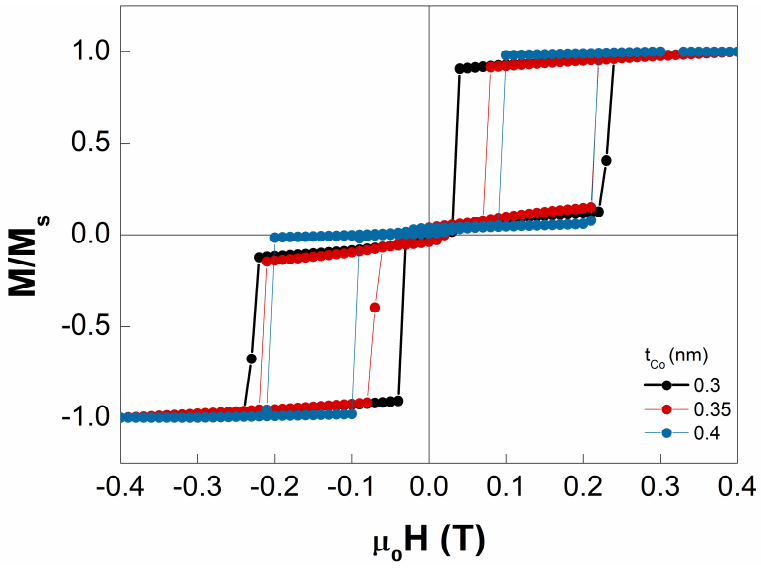

Figure 3.2. Room temperature out-of-plane field-dependent magnetization loops (M/M_s vs H) of $[Pd(0.9)/Co(t_{Co})]_6/Ru(0.4)/[Co(t_{Co})/Pd(0.9)]_6$ SAF thin film stacks deposited on SiO_2/Si (100) substrates.

In the final step, the effect of the bilayers number N was investigated. The Co and Ru layers' thicknesses were both set to 0.4 nm with the aim to get a large PMA together with a wide AF plateau (Figure 3.3). Changing the number of bilayers N does not significantly affect the J_{ex} value, which slightly increases from 0.82 mJ/m^2 to 0.85 mJ/m^2 as N increased from 4 to 8. However, the exchange field H_{ex} decreasing from ~230 mT to ~125 mT by increasing N from 4 to 8, respectively, due to the decrease of the total magnetic film thickness [220].

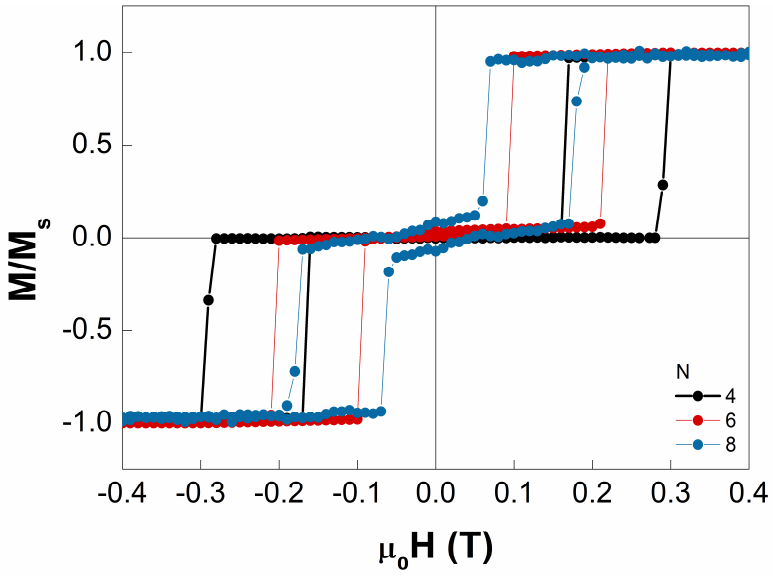

Figure 3.3. Room temperature out-of-plane field-dependent magnetization loops (M/M_s vs H) of $[Co/Pd]_N$/Ru(0.4 nm)/$[Co/Pd]_N$ thin film stacks deposited on SiO_2/Si (100) as a function of repetition number N (4, 6, 8).

On the basis of previous results, $[Pd(0.9)/Co(0.4)]_4$/Ru(0.4)/$[Co(0.4)/Pd(0.9)]_4$ SAF thin film stacks (thicknesses in nm) were used as building blocks for the growth of GMR SVs owing to the wide AF plateau reflecting a strong and almost compensated antiferromagnetic coupling in the SAF structure and the large perpendicular anisotropy over the whole system that this SAF structure offers.

3.1.2. **Co/Pd-based SAF thin film stacks for flexible PMA-GMR spin valves**

SAF thin film stacks with an optimized $[Pd(0.9)/Co(0.4)]_4$/Ru(0.4)/$[Co(0.4)/Pd(0.9)]_4$ structure (thicknesses in nm) were deposited on different substrates/underlayers, used to obtain flexible

PMA spin-valves, with the aim to explore the effect of the surface morphology on the magnetic properties of the SAF.

As reported in Figure 3.4, the out-of-plane field dependent magnetization loops show two well distinct minor loops separated by an almost fully compensated AF plateau for all the samples except for SAF thin film stacks deposited on KBr substrates. With respect to reference samples deposited on SiO_2/Si (100) substrates, no significant differences have been observed in terms of H_c and H_{ex} for SAF thin films deposited on MICA. When the film stacks are grown on Teonex®, PMMA/SiO_2/Si (100), and Au/SiO_2/Si (100), the characteristic two-steps behavior is still present but both the minor loop coercivity and the width of the AF plateau are affected by the substrate/underlayer. A significant change of the properties is observed for SAF thin films deposited on KBr (100), whose hysteresis loop becomes widely open in the middle region.

As reported in more detail in the next paragraphs, the explored substrates/underlayers show a different surface morphology and in particular a higher surface roughness, which can transfer to the thin film stack thus explaining the observed change of the magnetic properties. Indeed, the roughness plays a big role in determining key properties of magnetic thin films. In particular, rough interfaces may affect the interlayer exchange coupling in synthetic antiferromagnetic heterostructures [222] or induce a deterioration of the magnetic properties of magnetic multilayers [223,224], such as Co/Pd and Co/Pt, whose PMA arises from the proximity effect between the 3d and 5d element at the interface, thus explaining the decrease in the interlayer exchange coupling field for the SAF stacks deposited on the different underlayers/substrates, especially in the case of KBr substrates. Moreover, interface roughness can also induce microstructural defects that may alter the magnetization reversal mechanism through the formation of pinning sites [176,225–227], thus explaining the increase in the coercive field of the SAF stacks when deposited on the different underlayers/substrates as compared to the case of flat SiO_2/Si

substrates. This effect becomes dominant especially in the case of KBr substrates where the coercivity significantly jumps to 135 mT.

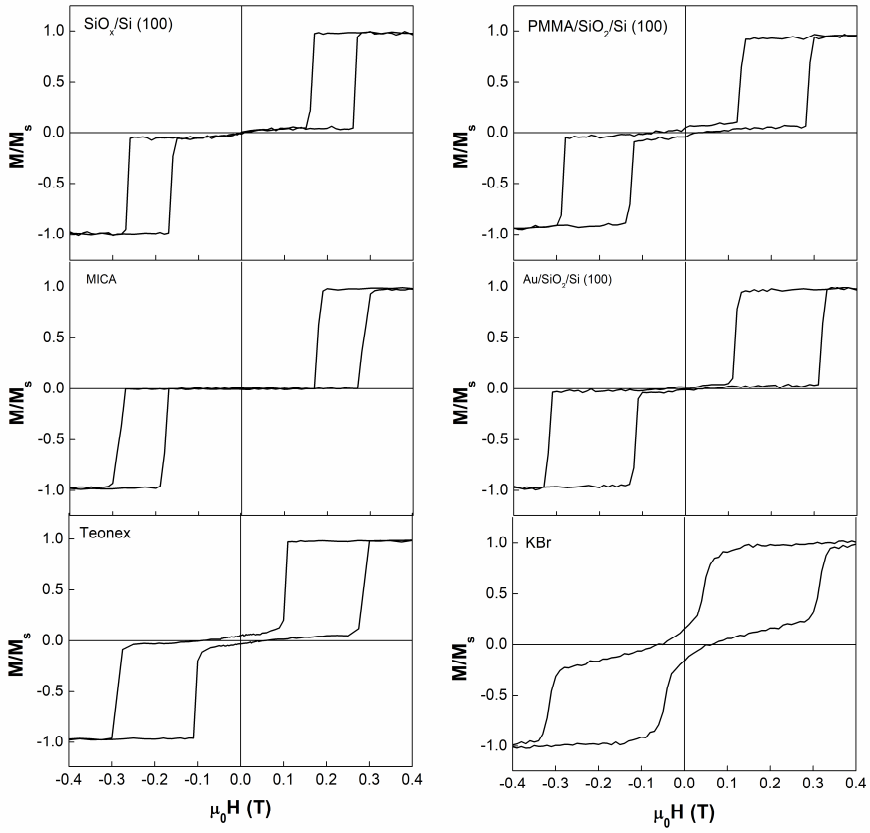

Figure 3.4. Room temperature out-of-plane field-dependent magnetization loops (M/M_S vs H) of $[Pd(0.9)/Co(0.4)]_4/Ru(0.4)/[Co(0.4)/Pd(0.9)]_4$ SAF thin film stacks deposited on different substrates.

3.2. PMA Co/Pd SAF-based GMR spin valves

The optimized SAF thin film stack was used as the reference layer of PMA-GMR SVs with a

Ta(10)/Pd(2.1)/[Pd(0.9)/Co(0.4)]$_4$/Ru(0.4)/[Co(0.4)/Pd(0.9)]$_3$/Co(0.4)/Cu/[Co(0.4)/Pd(0.9)]$_2$/Pd(2.1) structure, where [Co(0.4)/Pd(0.9)]$_2$ represent the free-layer and Cu the spacer thickness that was varied from 2 to 5 nm. The topmost Pd layer of the SAF was not included in the final stack to obtain a Co/Cu/Co interface and increase the efficiency of the spin-valve [228]. Flexible GMR spin valves with PMA were prepared by adopting two different strategies: (a) the direct deposition on flexible substrates, such as, freshly cleaved MICA and on Teonex® tapes and (b) the transfer-and-bonding approach that include wet etching lift-off and dry etching lift-off strategies exploiting the use of PMMA sacrificial layers, KBr sacrificial substrates and low-adhering-to-SiO_2 Au underlayers. For comparison, reference samples were also prepared by directly depositing the GMR SVs stacks on SiO_2/Si (100) substrates. The magnetic, magnetoresistance and, microstructural properties of the GMR SVs prepared by the different strategies were investigated and compared.

3.2.1. Reference PMA-GMR spin valves on SiO_2/Si (100) substrates

The room temperature out-of-plane M/M_s vs H loops of GMR-SV reference samples grown on SiO_2/Si (100) substrates are shown in Figure 3.5 (top panels) as a function of the Cu spacer thickness. A three-step field-dependent magnetization response associated to the individual sharp switching of the top layer of the reference electrode (*top* SAF-RL), the FL and the bottom layer of reference layer (*bottom* SAF-RL) is observed in all samples thus confirming the high reproducibility of the fabrication process, which ensure a large PMA and smooth interfaces to achieve the expected magnetization configuration as a function of the external field. The corresponding magneto-resistive curves (Figure 3.5a, b and c, bottom panels) show the typical behavior expected for a spin-valve system with a SAF reference layer. The GMR ratio, defined as $\Delta R/R_{low} = (R_{high} - R_{low})/R_{low}$, where R_{high} and R_{low} are the values of the resistance

corresponding to the antiparallel and parallel alignment of the magnetization at the Cu interfaces, shows a sudden increase in correspondence of the first jump in the hysteresis loop (at ~0.2 mT) thus indicating that the top SAF-RL switches first. This may be ascribed to a slightly higher magnetic anisotropy of the bottom layer of the SAF that is directly grown on the Pd/Ta buffer layer. The GMR ratio sharply reduces to its minimum value in correspondence of the magnetization reversal of the FL (at ~0.15 mT for t_{Cu} = 2 nm and ~0.3 mT for t_{Cu} = 3 and 5 nm). As the absolute value of the magnetic field increases further, a small kink is observed in the high field region corresponding to the GMR effect within the SAF-RL. The maximum GMR ratio of the spin valve stack decreases from ~4.5 % (for t_{Cu} = 2, 3 nm) to ~2.5 % (t_{Cu} = 5 nm), in line with the data reported in the literature for magneto-resistive systems based on Co/Pd multilayers [229–231]. The observed decrease of the GMR ratio with the increase in the non-magnetic layer thickness in the spin valves could be qualitatively ascribed to the reduction of the flow of electrons between the ferromagnetic layers with increasing spacer thickness which is due to the increase in scattering as the conduction electrons traverse the spacer layer [232].

TEM analysis was performed on a GMR SV stack with Cu thickness of 3nm. Figure 3.6 shows the very smooth and sharp interface between the Ta/Pd buffer layer and the SAF obtained by direct deposition on SiO_2/Si (100) substrates, which regularity extends over the successive layers. The Cu layer is clearly visible with a uniform thickness of about 3 nm, in perfect agreement with the nominal value.

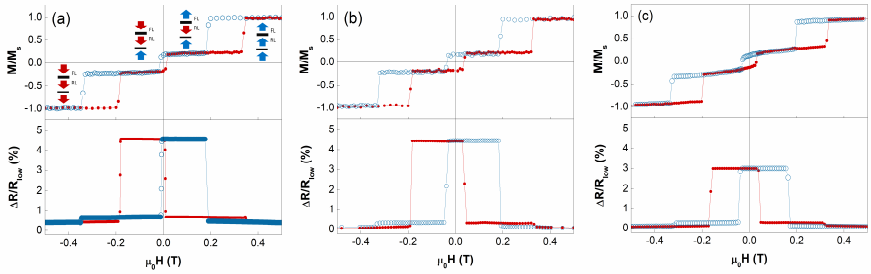

Figure 3.5. Magnetic and magneto-electric properties of PMA-GMR spin-valves deposited on SiO_2/Si (100) (reference samples). Top and bottom panels reports respectively on the room temperature out-of-plane hysteresis loops (M/M_s vs H) and the corresponding magneto-resistance (MR) response ($\Delta R/R_{low}$ vs H) as a function of Cu thickness: (a) 2 nm, (b) 3 nm and (c) 5 nm. Different colors and symbols are used for the upward and downward branches of both the hysteresis loops and MR curves to evidence the field sweep direction. The arrows reported in the top panel of figure (a) denote the mutual alignment of the magnetization in the FL, *top*-RL and *bottom*-RL at different points in the loop; the same evolution of the magnetic configuration is observed in all the other samples.

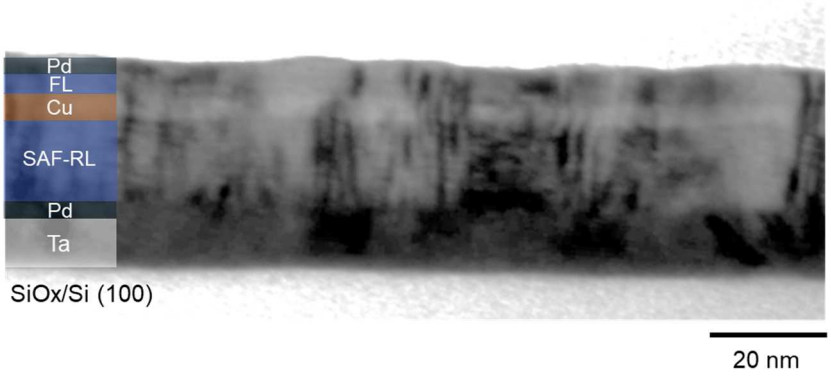

Figure 3.6. Cross section TEM bright-field image of a GMR-SV thin film stack (t_{Cu} = 3 nm) on SiO_2/Si (100).

3.2.2. **Flexible GMR spin valves - Direct deposition on flexible substrates**

Large area flexible PMA-GMR spin valve stacks were obtained by directly depositing the stacks on both flexible Teonex® tapes and freshly cleaved MICA substrates (Figures 3.7a and 3.8a).

The out-of-plane field-dependent magnetization loops of the spin valve stacks deposited on Teonex® tapes and on freshly cleaved MICA substrates are reported in figures 3.7 and 3.8 (top panels), respectively. With respect to the reference samples deposited on SiO_2/Si (100) substrates, no significant changes were observed. The loops show the characteristic three-steps reversal behavior of a GMR SV stack with a SAF-RL, and only small differences in terms of individual layer coercivity and reverse fields are present, likely due to an enhanced interface roughness as discussed later in the text. The corresponding magnetoresistance curves of thin film stacks deposited on Teonex® and MICA are reported in figures 3.7 and 3.8 (bottom panels), respectively. Similar to the reference samples, as the Cu spacer thickness increases from 2 nm to 5 nm, the GMR ratio decreases from 3.4 % to 2.8 % in the case of Teonex® tapes and from 4.1% to 3% for MICA substrates, due to the enhanced current shunting and scattering effects with the increase of Cu spacer thickness [232]. The measured GMR ratio values are perfectly in line with those of the reference samples, thus demonstrating the using Teonex® and MICA allows producing high quality GMR SVs on flexible substrates by direct deposition on top. Only a slight reduction is observed for thin film stacks grown on Teonex® tapes, which may be ascribed to its slightly higher average surface roughness (~0.7 nm, as reported in the data sheet) as compared to the Si/SiO_2 roughness of (~0.3 nm). Despite the presence of the sharp magneto-resistive jumps in all the samples deposited on Teonex® and MICA substrates, the shape of the MR curve differs while changing the Cu spacer thickness. Compared to the reference samples, the

magnetoresistance curves of the GMR SVs on Teonex® tapes with 3 and 5 nm Cu spacers report the same behavior, i.e. a symmetric curve with respect to zero field. This confirms that, the reversal starts with the switching of the top layer of the SAF reference layer followed by the switching of the free layer as indicated by the sudden increase of the GMR ratio to its maximum value. However, when the Cu spacer thickness is reduced to 2 nm, a qualitative change in the magnetoresistance behavior occurs (Figure 3.7b, bottom panel). Starting from the saturation, a small kink, corresponding to the switching of the SAF bottom layer, occurs first, followed by a sudden increase of the GMR ratio to its maximum value corresponding to the reversal of the SAF-FL. A similar behavior of the magnetoresistance curve was observed for GMR SVs grown on MICA substrates with a Cu thickness of 2 and 5 nm. For thin film stack with a 3 nm thick Cu spacer deposited on MICA, a different magnetoresistive response was observed consisting on an asymmetric MR curve with respect to zero field.

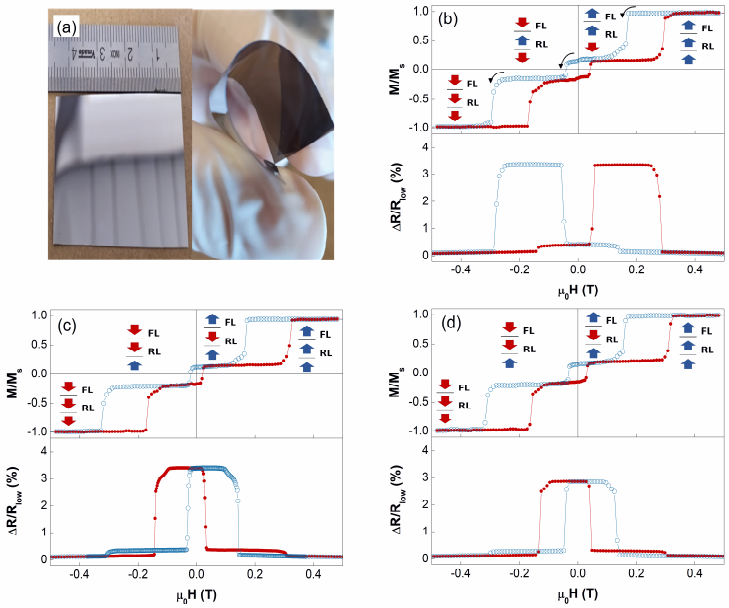

Figure 3.7. Co/Pd-based PMA-GMR spin valves deposited on Teonex® substrates. (a) Optical photograph of a free-standing and flexible PMA-GMR spin valve. (b-c) Room temperature out-of-plane hysteresis loops (M/M_s vs H) and corresponding magneto-resistance (MR) response ($\Delta R/R_{low}$ vs H) as a function of Cu thickness: (b) 2 nm, (c) 3 nm and (d) 5 nm. Different colors and symbols were used for the upward and downward branches of both the hysteresis loops and MR curves to show the field sweep direction. The arrows reported in top panels of the figures (b-c) denote the mutual alignment of the magnetization in the FL, *top*-RL and *bottom*-RL, depending on the external magnetic field.

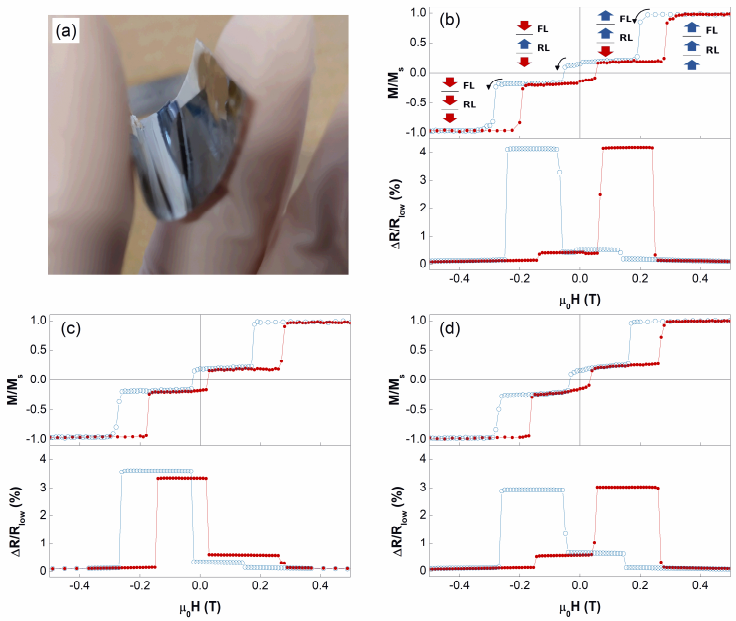

Figure 3.8. Co/Pd-based PMA-GMR spin valves deposited on MICA substrates. (a) Optical photograph of a free-standing and flexible PMA-GMR spin valve. (b-c) Room temperature out-of-plane hysteresis loops (M/M_s vs H) and corresponding magneto-resistance (MR) response ($\Delta R/R_{low}$ vs H) as a function of Cu thickness: (b) 2 nm, (c) 3 nm and (d) 5 nm. Different colors and symbols were used for the upward and downward branches of both the hysteresis loops and MR curves to show the field sweep direction. The arrows reported in figure (b) denote the mutual alignment of the magnetization in the FL, *top*-RL and *bottom*-RL, depending on the external magnetic field; the same evolution of the magnetic configuration is observed in the sample of figure (d).

To explore the reason behind the observed behavior of the MR curves, TEM and SEM analysis were carried out to study the morphological and microstructural changes induced by the substrate. At the local level, TEM cross section images (figures 3.9a, c) show the presence of very smooth and sharp interfaces in both the cases, thus explaining the high-quality of the GMR spin valve stacks deposited on Teonex® and MICA substrates. Large area SEM images of GMR-SV thin film stacks deposited on Teonex® (Figure

3.9b) confirm the very smooth surface of the stack, which results from the very low surface roughness of Teonex® compared to the most commonly used polymer tapes for flexible spintronics [233]. Despite the microstructural analysis does not allow appreciating any significant difference with respect to the reference samples, the slight change of magnetic properties (e.g. minor loop coercivity, individual layer switching field), the moderate reduction of the GMR ratio and also the peculiar shape of the MR curve for t_{Cu} = 2nm, which may be the consequence of a coupling between the FL and the Top SAF-RL, can be induced by the slight higher surface roughens of Teonex®, which is around 0.7 nm accordingly to the data sheet. As concerns the samples deposited on fresh cleaved MICA substrates, large area SEM images (Figure 3.9d) reveal the presence of cleavage steps and smooth terraces extending over several microns, which formed during the exfoliation process. The atomically flat terraces ensure the growth of thin film heterostructures with magnetic properties comparable to that of system grown on SiO_2/Si (100) substrates. However, the presence of cleavage steps may affect the coupling between the layers and possibly the electrical path, which would result in minor effect in the M vs H loop and in a significant change of the MR curve shape. However, owing to the randomness of the exfoliation process, the observed difference in the magnetic and magneto-transport properties cannot be ascribed to the Cu thickness but rather to the specific surface morphology of the substrate used for the deposition.

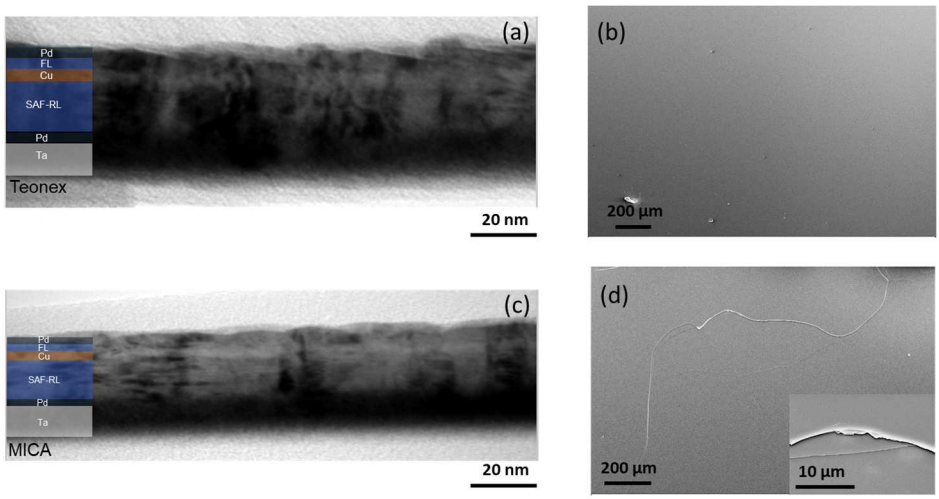

Figure 3.9. (a, c) Cross section TEM bright field and (b, d) SEM surface images of Co/Pd-based GMR-SV thin film stacks (t_{Cu} = 3 nm) deposited on (a, b) Teonex® tapes and (c, d) fresh cleaved MICA substrates. Inset in figure d reports on a magnification of a cleavage step.

3.2.3. **Flexible GMR spin valves - Transfer-and-bonding strategies**

Transfer-and-bonding approaches exploiting both wet etching lift-off and dry etching lift-off strategies were used to prepare flexible PMA-GMR spin valve stacks.

Wet etching lift-off – PMMA and KBr sacrificial layers/substrates

Figures 3.10a and b show the filed-dependent magnetization loops of GMR SVs thin film stacks grown on freshly cleaved KBr (100) substrates. The typical three-steps reversal is hardly observed in this case, suggesting the absence of smooth surface/interface. The same behavior was obtained after dissolving the salt substrate and transferring the film stack on a Kapton tape (figure 3.10c, d), thus suggesting that the transferring process is not a critical step.

To disclose the origin of the observed magnetic behavior, large area SEM images of the surface of cleaved KBr substrates and GMR SV thin film stacks (t_{Cu} = 3 nm) before and after the transferring process were carried out (Figure 3.11). The KBr substrate (Figure 3.11a) present brittles and fractures that in turn propagate to the deposited thin film stack (Figures 3.11b, c) and causes inhomogeneity and interfacial defects that may explain the deterioration of the magnetic properties of the GMR-SV thin film stacks, which strongly depend on the quality of the interface. Due to the presence of brittles and fractures it was not possible to carry out the MR measurements. The results indicate that further optimization are necessary to obtain high quality thin film heterostructures on water soluble salt substrates.

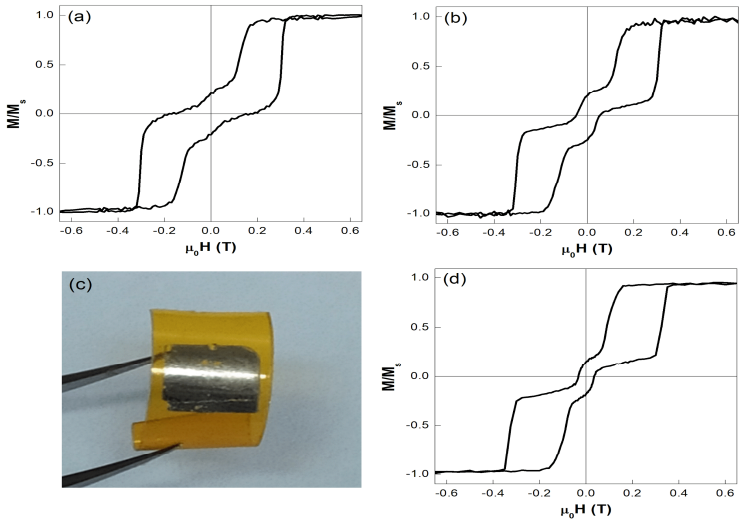

Figure 3.10. Wet etching lift-off – Freshly cleaved KBr (100) sacrificial substrates. (a, b) Room temperature $M/M_s(H)$ out-of-plane magnetization loops and corresponding magneto-resistance (MR) curves ($\Delta R/R_{low}$ vs H) of GMR-SV thin film stacks on KBr (100) substrates as a function of Cu thickness: (a) 2 nm and (b) 3 nm. (c) Optical photograph of a free-standing and flexible PMA-GMR spin valve. (d) Out-

of-plane $M/M_s(H)$ loops of a flexible spin-valve (Cu: 3 nm) obtained after dissolving the sacrificial layer.

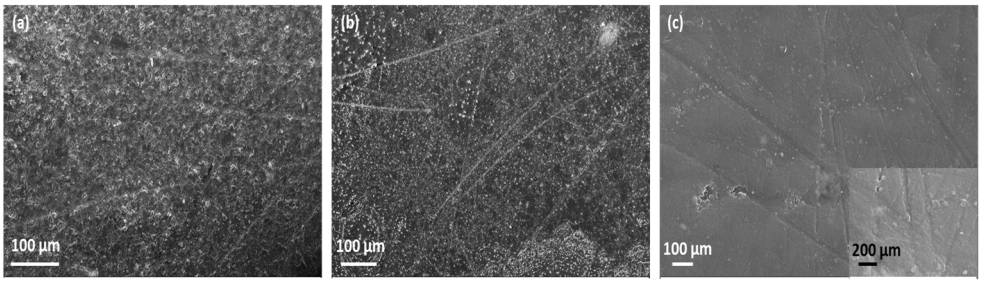

Figure 3.11. Large area SEM images showing the surface of: (a) cleaved KBr (100) substrates; (b,c) GMR SV thin film stacks (t_{Cu} = 3 nm) deposited on fresh cleaved KBr (100) substrates (b) before and (c) after the transferring on a Kapton tape . Inset in figure c reports a magnification of the image.

The magnetic and the magnetoresistive properties of the GMR SV thin film stacks with a Cu spacer of 2 and 3 nm deposited on PMMA/SiO_2/Si substrates exploiting PMMA sacrificial layers are reported in figures 3.12a, b and c (top panels). Similar to the reference samples deposited on SiO_2/Si (100) substrates, the field-dependent magnetization loops show the typical three-steps reversal behavior of a spin valve with a SAF-RL, which corresponds to the sharp reversal of the SAF-RL and the FL. However, M vs H curves show a slight increase of the coercivity of the bottom and top layers of the SAF from ~0.07 T to ~0.09 T. The corresponding magnetoresistance curves (figures 3.12a, b and c, bottom panels) show the typical behavior corresponding to a GMR spin valve with a SAF-RL, where a sudden increase of the GMR ratio occurs in correspondence of the first jump in the hysteresis loop indicating that the top SAF-RL switches first. All the spin valve stacks with 2, 3 and 5 nm thick Cu spacer report a maximum GMR ratio of around 2%. The lower GMR ratio compared to that of the reference samples could be due to defects and inhomogeneity induced by the increased interfacial roughness in the GMR SVs on PMMA/SiO_2/Si layer, which could be also responsible of

the increase of the coercivity of the SAF bottom and top layers. The roughness may arise during the spin-coating process of the PMMA on the rigid SiO_2/Si substrate as usually it is very critical to control the thickness uniformity, surface smoothness and the overall PMMA film quality.

The lift-off process was performed as described in chapter 2. Figure 3.13a reports on the magnetic hysteresis loop of the GMR spin valve with a 3 nm thick Cu spacer obtained after transferring the film stack on a Kapton tape. Compared to the magnetic loop of the GMR-SV thin film stack before the transferring step, the main magnetic features were maintained thus confirming the feasibility of the wet etching lift-off strategy exploiting PMMA sacrificial layers in obtaining the expected magnetization configuration on flexible tapes. Moreover, the approach allows highly flexible PMA GMR-SV thin film stacks to be obtained on large areas as shown in the optical image reported in figure 3.13b.

Despite we performed many attempts and modified the experimental conditions, we were unable to avoid the formation of cracks during the transfer-and-bonding process, which prevented performing the MR measurements. This was confirmed from the SEM analysis reported in figures 3.14a, b for the SV stack with a 3 nm thick Cu spacer before and after the transfer-and-bonding process. The GMR SV on PMMA/SiO_2/Si has a very smooth surface with the presence of some scratches (Figure 3.14a). On the contrary, a lot of cracks and flaking in the metal films formed after performing the lift-off process (Figure 3.14b). The observed wavy regions are an effect of the electron beam of the microscope. These cracks could be potential complications associated with the physical release process that may be due to the mismatch between the polymer and substrate, or it may be due to stresses during the phases of deposition, transfer, and bonding added to the shrinkage of the adhesive material during curing [234–236]. The obtained results impose the necessity of further improvements and optimizations of the lift-off process via PMMA sacrificial layers in the future.

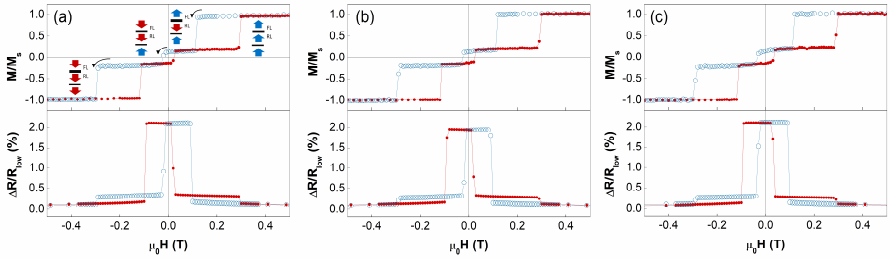

Figure 3.12. Wet etching lift-off - PMMA sacrificial layer. Room temperature $M/M_s(H)$ out-of-plane magnetization loops and corresponding magneto-resistance ($\Delta R/R_{low}$ vs H) curves of PMA-GMR spin-valves deposited on PMMA/SiO_2/Si as a function of Cu thickness: (a) 2 nm, (b) 3 nm and (c) 3 nm. Curved arrows in the $M/M_s(H)$ loops and different colors and symbols for the upward and downward branches of both the hysteresis loops and MR curves are used to show the field sweep direction. The arrows reported in the top panel of figure (a) denote the mutual alignment of the magnetization in the FL, *top*-RL and *bottom*-RL at different points in the loop; the same evolution of the magnetic configuration is observed in all the other samples.

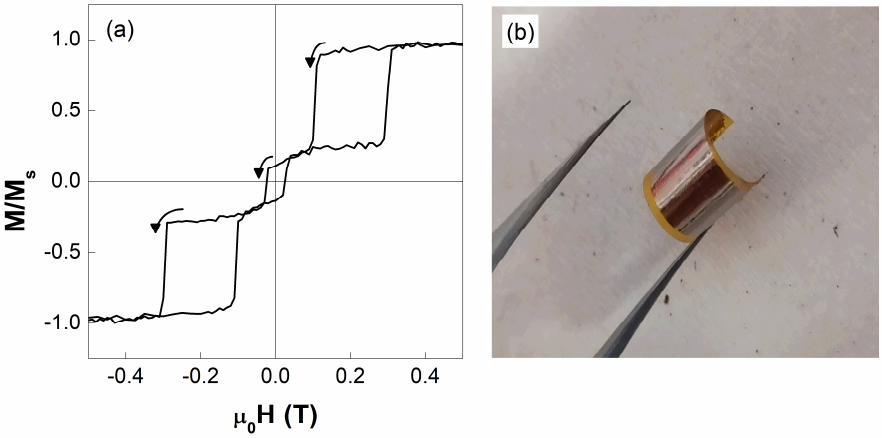

Figure 3.13. (a) Room temperature $M/M_s(H)$ out-of-plane magnetization loop of a flexible GMR spin-valve (Cu: 3 nm) obtained after dissolving the sacrificial PMMA layer. (b) Optical photograph of a free-standing and flexible PMA-GMR spin valve.

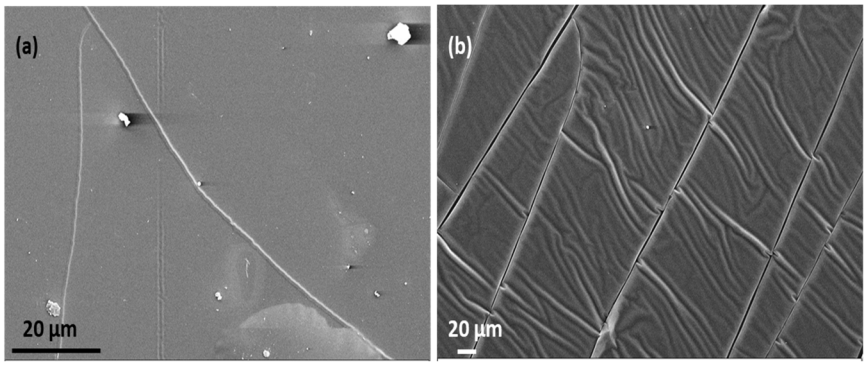

Figure 3.14. SEM images showing the surface of a GMR-SV thin film stack with a 3 nm thick Cu spacer deposited on PMMA/SiO_2/Si (100) substrates: (a) before and (b) (b) after the transfer-and-bonding process.

Dry etching lift-off – Low adhesion Au buffer layer

Flexible PMA-GMR spin valve stacks were prepared by using an innovative transfer-and-bonding approach exploiting the low adhesion of a gold underlayer to SiO_2/Si(100) substrates [202,237–239] (see chapter 2 for details).

When the film stacks are deposited on the Au-underlayer the main magnetic and magneto-resistive features are maintained for t_{Cu} = 3 and 5 nm (Figures 3.15b and c). The field-dependent magnetization and magneto-resistive loops show the same sharp reversal versus field as in the corresponding reference samples and a still relevant GMR ratio of ~1.5 %. However, the M Vs H loop shows an increment of the coercivity of bottom and top layers of SAF (from ~0.07 T to ~1.1 T) and a slight reduction of the coercivity of the free-layer (from ~0.35 mT to ~0.25 mT), which result in a narrowing of the plateau in the high-resistance region of the MR curves. When the Cu spacer thickness is reduced down to 2 nm, a major change occurs as indicated by the appearance of an “inverted” field-dependent

magnetization loop in the region around zero field that also manifests in a significant change of the magnetic-resistive curve (figure 3.15a). To disclose the origin of this behavior, field-dependent resistance loops were measured within the low-field region where only the FL switches (-0.15 – 0.15 mT) for two opposite initial states of the SAF-RL, i.e. after saturating the heterostructure with either a negative ($-H_{sat}$) or a positive ($+H_{sat}$) saturation field of 1 T. As shown in figures 3.16a and b, the hysteresis loop at low fields is subjected to a magnetic bias whose sign depends on the magnetic configuration of the SAF: when its *top* layer points inward (outward) the shift is positive (negative). This behavior may originate from an interlayer coupling between the FL and the top-SAF_RL, possibly triggered by the higher roughness of the film when the heterostructure comprises the Au underlayer, which can lead to an interlayer magnetostatic interaction (orange-peel Néel coupling) or a direct exchange coupling through the formation of pinholes in the Cu spacer layer [240].

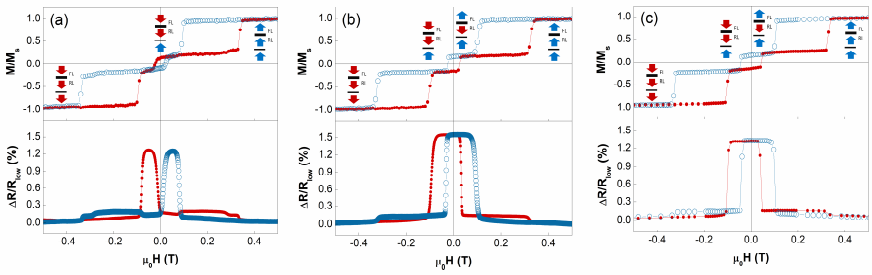

Figure 3.15. Magnetic and electric properties of perpendicular GMR-SVs deposited on Au/SiO_2/Si(100) before the peel-off procedure. Top and bottom panels report on the room temperature out-of-plane hysteresis loops (M/M_s vs H) and the corresponding magneto-resistance (MR) response ($\Delta R/R_{low}$ vs H) as a function of Cu layer thickness: (a) 2 nm, (b) 3 nm, and (c) 5 nm. Different colors and symbols are used to evidence the two sweep directions of the external field. The sketches reported in the top panels denote the mutual alignment of the magnetization (arrows) in the FL, *top* SAF-RL, and *bottom* SAF-RL at different points in the loop for the magnetic field sweep from positive to negative values.

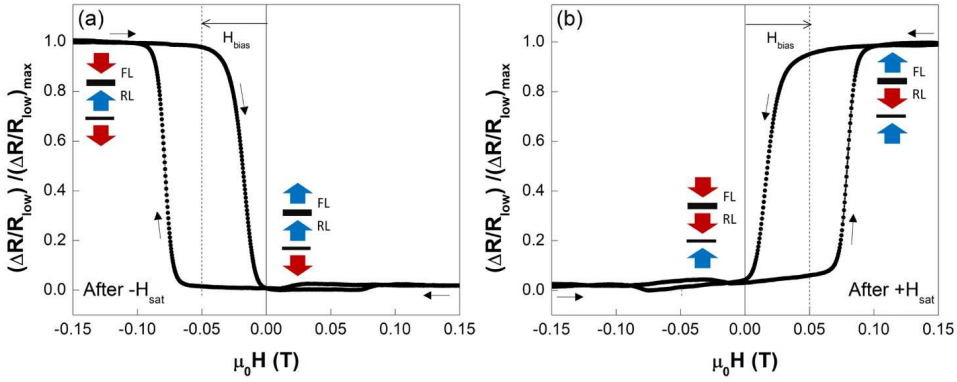

Figure 3.16. Room temperature field-dependent resistance loops in the low-field region (-0.15 – 0.15 mT) of thin film stacks with t_{Cu} = 2nm deposited on Au/SiO_2/Si(100). Measurements were performed for two opposite magnetic configurations of the SAF obtained by saturating the sample with either a negative (-H_{sat}. panel a) or a positive (+H_{sat}, panel b) saturation field of 1 T. Thin arrows indicate the field swept direction, while the thick arrows illustrate the mutual alignment of the magnetization in the FL, *top*-RL, and *bottom*-RL at different points in the loop The hysteresis loop of the FL is subjected to a magnetic bias due to its interaction with the *top* SAF-RL whose sign depends on the magnetic configuration of the SAF: when its top layer points inward (outward) the shift is positive (negative).

The observed differences with respect to the reference samples are ascribed to the specific morphology of the Au underlayer, whose growth on SiO_2 follows the *Volmer-Weber* mechanism, involving the nucleation and growth of islands that coalesce when the thickness reaches a value between 10 and 15 nm [238]. The resulting nanogranular microstructure can lead to surface inhomogeneity extending over the whole structure deposited on top, which may affect the PMA of the Co/Pd multilayers [223,224], the interlayer exchange coupling in synthetic antiferromagnetic heterostructures[222] and the magneto-resistive properties of the whole GMR spin-valve stack [240]. To investigate the microstructural changes induced by the Au underlayer in details, TEM analysis was performed on a SV stack (t_{Cu} = 3nm) deposited on

Au/SiO_2/Si (100). In this sample, the TEM image in figure 3.17 shows the presence of adjacent Au islands, confirming the Volmer-Weber growth and resulting in a wavy surface (yellow arrow and dotted line used as a guide for the eyes) with an estimated amplitude and wavelength of ~1.5 nm and ~20 nm, respectively. Although the roughness tends to be transmitted to the upper layers (white and blue arrows and dotted lines at the buffer layer/SAF and SAF/Cu interfaces), the ratio between the amplitude and the wavelength associated to it is small enough that the whole structure is overall retained. However, the presence of this roughness can be a source of inhomogeneity and defects, which in turn may locally affect the magnetic and magneto-resistive properties of the systems. In particular, it may be responsible for the reduction of the GMR ratio[240] and the enhancement of the coercivity of the bottom and top layers of the SAF as a result of an increase domain wall pinning [241,242]. Moreover, it can be the source of interlayer magnetostatic interactions (orange-peel Néel coupling) or a direct exchange coupling through the formation of pinholes in the Cu spacer layer[240], between the FL and the *top* SAF-RL, which can explain the inverted magnetization loop for t_{Cu} = 2 nm and the slight reduction of the coercivity of the free layer for t_{Cu} = 3 nm.

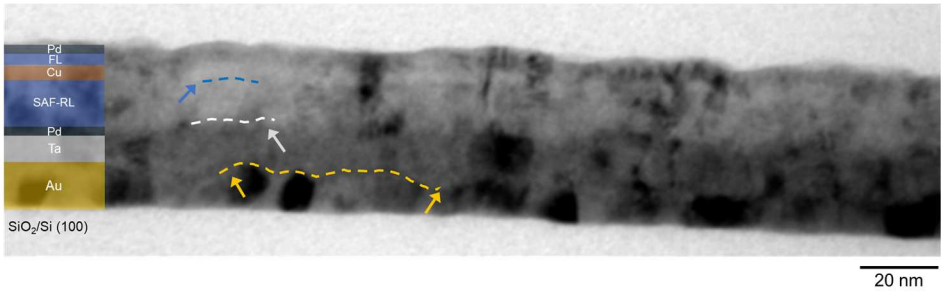

Figure 3.17. TEM bright field image of a spin-valve stack (t_{Cu} = 3 nm) on Au/SiO_2/Si (100). The Volmer-Weber growth mechanism of the Au underlayer results in a wavy interface with the Ta buffer layer (gold arrow and dotted line). The ripple is then transferred to the Pd/SAF-RL (white arrow and dotted line) and SAF-RL/Cu (blue arrow and dotted line) interfaces.

Spin-valve thin film stacks with a Cu spacer thickness of 3 nm, showing the characteristic magnetic and magneto-resistive features of perpendicular magnetized GMR-SVs with a SAF-RL and a still relevant GMR ratio when grown on the gold underlayer, were transferred on a flexible tape by mechanical peel-off as described in chapter 2. Despite the presence of very thin layers forming the spin valve thin film stacks whose thickness is as low as 0.4 nm for Co and Ru, both the magnetic and magneto-resistance behavior remain unchanged after the peeling-off process (figure 3.18b), thus revealing the high robustness of the system and high potentiality of the proposed Au-mediated transfer-and-bonding methodology that allows transferring complex multilayered heterostructures over large areas (figure 3.18a) on flexible tapes without sacrificing their properties (which is clearly demonstrated when the results are compared with those of the sample before peeling (figure 3.15b).

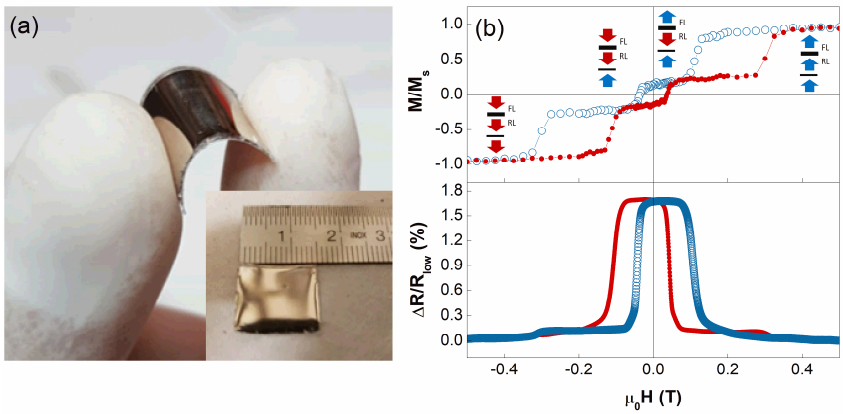

Figure 3.18. (a) Optical photograph of a flexible PMA-GMR spin-valve (t_{Cu} = 3 nm). (b) Corresponding room temperature out-of-plane hysteresis loops (M/M_s vs H) and magneto-resistive response ($\Delta R/R_{low}$ vs H). Different colors and symbols were used for the upward and downward to evidence the field sweep direction.

In order to explore the possibility to integrate such flexible systems on curved surfaces, bending tests under a uniform magnetic field were

performed on flexible spin-valves with t_{Cu} = 3 nm. To the best of our knowledge, the effect of bending in perpendicular magnetized GMR-SV thin film stacks is not reported in literature and here we disclose the influence of the geometry of a bended heterostructure. Contrary to the case of planar samples, when a PMA flexible spin-valve is bended and placed in a uniform magnetic field, each region of a folded sample will experience a different angle with the external magnetic field (Figure 3.19a), thus resulting in a variation of the magneto-resistance. To quantify the geometrical effect of a folded heterostructure, samples were glued to a plastic semi-cylindrical support with a given radius of curvature *r* = 5 mm (refer to chapter 2) and Van Der Pauw measurements were performed at different bending angles $\theta\ (°) = L \cdot 360/2\pi r$ ranging between 20° and 180°, where *L* is the distance between the electrical contacts along the side of the sample parallel to the bending along which the probing current is injected (Figure 3.19b). This configuration with a fixed radius of curvature allows measuring the effect of the angular distribution between the magnetic field and the easy axis while keeping constant the strain to which the heterostructure is subject. Representative magneto-resistive curves for different bending angles are reported in Figure 3.20b, c. As compared to the planar structure, the GMR ratio of the bended samples (hereafter called $GMR_B(\theta)$, where "B" stands for "bended") slightly decreases down to ~15% of the GMR of the flat sample for θ = 180°.

To explain the observed behavior, the change of the magnetization loops was first studied on planar samples (i.e. without bending) as a function of the angle Φ between the external applied field *H* and the film normal (Φ = 0° for *H* perpendicular to the film plane). As shown in Figure 3.21a, the characteristic three-step behavior of perpendicular GMR-SV with a SAF-RL is retained up to Φ = 45°, while at larger angles ($\Phi \geq 60°$) the shape of the loop significantly changes with a progressive evolution towards a fully reversible curve at Φ = 90°, corresponding to the magnetic hard-axis of the stack. This magnetic behavior is also reflected in the magneto-resistive curves

measured as a function of the angle Φ (Figure 3.21b), revealing that the magneto-resistive response is almost insensitive for angles $\Phi \leq 45°$. Figure 3.21c indicates that the maximum GMR_P ratio (where "P" stands for "planar") slowly decreases with Φ approaching a cross-geometry configuration when the magnetic field is parallel to the sample surface (Φ = 90°), where the magneto-resistive curve significantly differs from that measured at Φ = 0°.

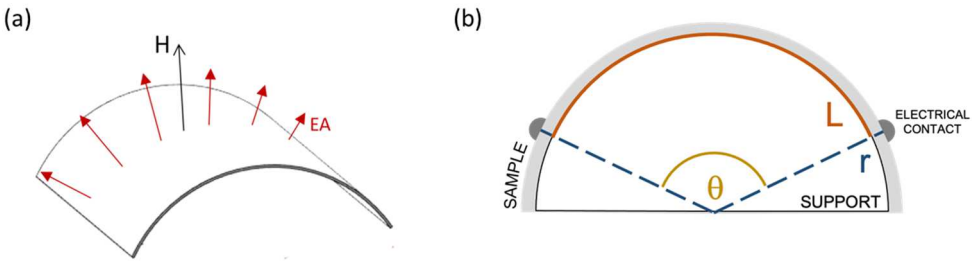

Figure 3.19. (a) Schematic representation of a bended system with out-of-plane magnetic anisotropy (EA: easy-axis) placed in a uniform magnetic field (H). Each region of the sample will experience a different angle with the external magnetic field, which depends on the sample curvature. (b) Geometrical definition of the bending angle $\theta\ (°) = L \cdot 360/2\pi r$; r is the radius of the semi-cylindrical plastic support and L is the distance between the electrical contacts along the side of the sample parallel to the bending.

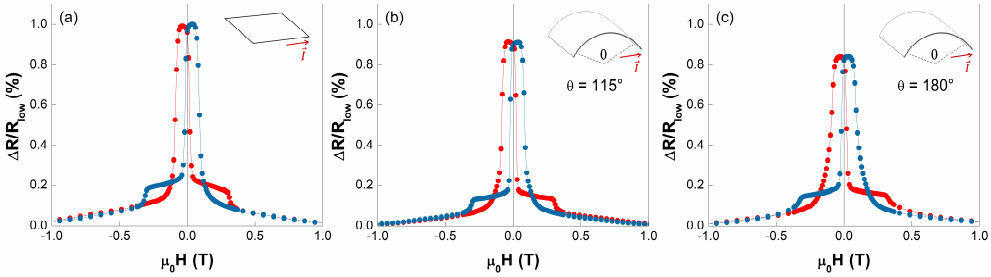

Figure 3.20. Representative room temperature magneto-resistive curves of flexible perpendicular GMR-SVs with t_{Cu} = 3nm: (a) without bending (θ = 0°) and (c,d) under

a bending angle of (c) 115° and (d) 180°; the probing current *I* is injected parallelly to the curvature. Curves are normalized to the maximum $\Delta R/R_{low}$ value measured on the flat sample (θ= 0°).

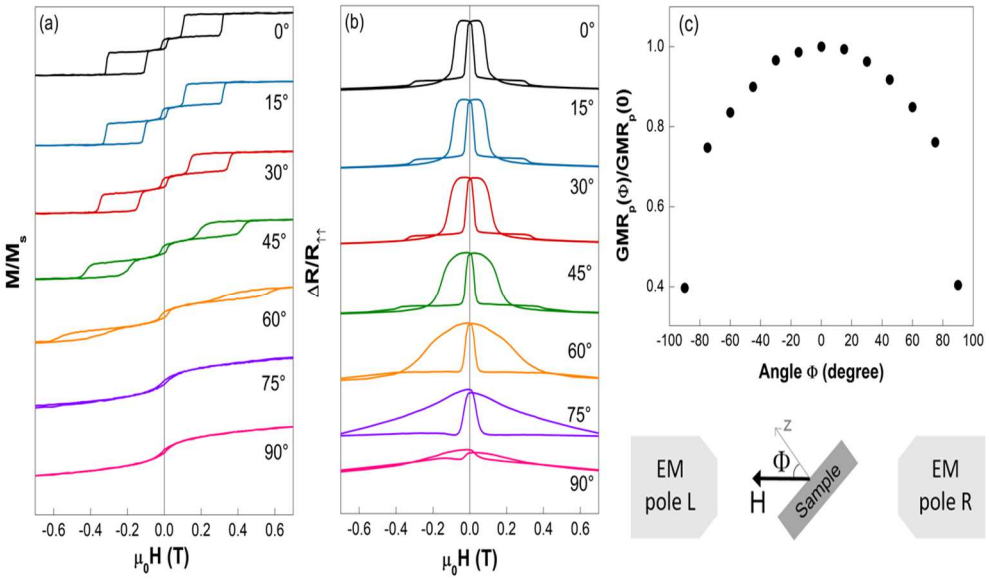

Figure 3.21. Evolution of the (a) magnetic (M/M_s vs H) and (b) magnetoresistive ($\Delta R/R_{low}$ vs H) response of a planar flexible GMR spin valve (t_{Cu} = 3nm) as a function of the angle Φ between the external applied field H and the film normal. All measurements were performed at room temperature. (c) Evolution of the maximum of the GMR ratio normalized to the value at Φ = 0° as a function of the angle Φ, $GMR_P(\Phi)/GMR_P(0)$, as obtained from the curves in (b). The sketch illustrates the experimental configuration.

Starting from these results, the evolution of the GMR ratio as a function of the bending angle, $GMR_B(\theta)$, is modeled as the integral of the experimental $GMR_P(\Phi)$, where Φ accounts for the different angle that each portion of the sample forms with the magnetic field due to the bending. Referring to the sketch in the inset of figure 3.20b, c, the expected GMR ratio for the bended film under the magnetic field can be interpret as the result of the following integral:

$$GMR_B(\theta) = \frac{1}{\theta}\int_{-\frac{\theta}{2}}^{\frac{\theta}{2}} GMR_P(\Phi)d\Phi \qquad (3.1)$$

calculated over the whole path of the current. Figure 3.22 shows the quantitative agreement between measurements and model suggests that the moderate reduction of the GMR ratio upon bending is related to the distribution of the magnetic easy-axis with respect to the external field. In this sense, we do not observe major changes in the electric behavior (both resistance and GMR ratio), suggesting the robustness of such flexible PMA spin-valves with respect to bending.

Finally, it is worth mentioning that we do not detect a major effect of strain on the magneto-electric behaviour. Indeed, the GMR ratio of flat samples is the same as the one measured on the same samples at small bending angles (up to θ = 20°), where the magnetic field can be considered orthogonal to the surface within the experimental error bar. This suggests that the level of strain we applied, which meets the curvature of practical applications, does not imply any significant effect on the magneto-electric properties of our heterostructures.

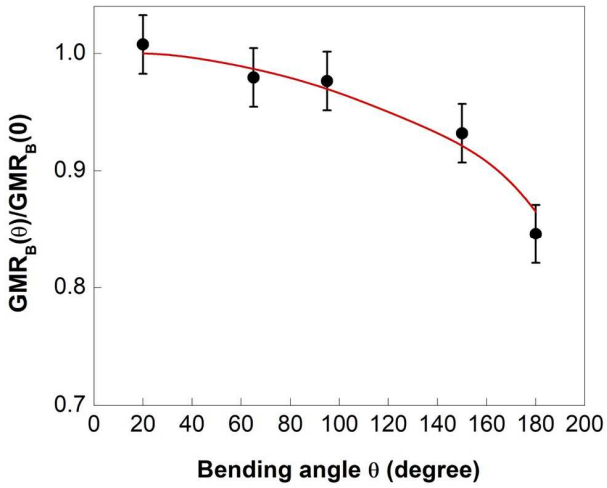

Figure 3.22. Experimental $GMR_B(\theta)$ ratio normalized to the value measured on the flat sample ($\theta = 0°$). (dots) compared with the values calculated from the model of Eq. 3.1 (continuous line).

3.3. Conclusions and perspectives

Different strategies, including direct deposition on flexible substrates and both dry- and wet-etching transfer-and-bonding approaches have been exploited to obtain flexible Co/Pd-based GMR spin-valve thin films with perpendicular magnetic anisotropy consisting of a $[Co/Pd]_N$ free layer and a fully compensated $[Co/Pd]_N/Ru/[Co/Pd]_N$ synthetic antiferromagnet reference layer separated by a Cu spacer of variable thickness. Concerning the direct deposition of flexible substrates, for the first time, we demonstrated that using Teonex® substrates, consisting of a PEN tape with a flattening capping layer, allow obtaining high quality flexible GMR spin-valves with PMA and showing a GMR ratio of ~3.5%, which is very close to that of the reference samples. However, this polymer tape can be only used to grow thin film systems that do not require high processing temperatures (> 500 K). By using fresh cleaved MICA substrates, which also allow for high

temperature processes, very good magnetic and magneto-resistive properties, comparable to those of reference samples, were obtained. However, the cleavage process it not easily controllable and it induces the formation of micrometer size terraces and cleavage steps that affected the shape of the MR curves. Therefore, further work it is necessary to improve the cleavage process with the aim to obtain a flat surface over large areas. As for the wet-etching lift-off strategy based on water soluble KBr (100) sacrificial substrates, the results proved that the transferring process is not a critical step, however the presence of brittles and fractures on the KBr surface causes inhomogeneity and interfacial defects that lead to a deterioration of the magnetic properties of the GMR-SV thin film stacks. When PMMA sacrificial layers were used for the wet-etching lift-off strategy, only a moderate change of the magnetic and the magneto-resistive properties was observed. However, while the overall magnetic properties are maintained after carrying out the lift-off process, the magneto-resistive properties were strongly deteriorated due to the formation of cracks. By exploiting the weak adhesion of an Au underlayer on SiO_x/Si(100) substrates, perpendicular GMR-SVs with a still sizeable GMR ratio of ~1.5 %, were efficiently transfer on commercial adhesive tapes by mechanical peel-off while preserving the whole magnetic and magneto-resistive properties despite the presence of very thin layers forming the spin valve thin film stacks (down to 0.4 nm). An improvement of the GMR ratio towards the limit of reference samples deposited on SiO_x/Si (100) substrates is expected to be achieved by further reducing the Au surface roughness through a fine optimization of the deposition conditions. The results also prove the effectiveness of the proposed Au-mediated transfer and bonding approach, which can be easily extended to the grown of other functional and flexible multilayer materials engineered at the nanoscale, including those whose fabrication process requires high temperature treatments that impedes the direct deposition on flexible polymeric tapes. Finally, magneto-resistance measurements versus bending revealed the magneto-electric robustness of

these flexible structures, where the moderate change in the GMR ratio is mainly ascribed to the geometrical configuration with respect to the magnetic field rather than to a change of the electric behavior, thus paving the way for their integration on curved surfaces and the development of novel flexible devices requiring perpendicular magnetic anisotropy.

Chapter 4.

Perpendicularly magnetized Co/Ni SAF-based GMR spin valves on flexible substrates

This chapter reports on flexible Co/Ni-based GMR spin-valve thin films with perpendicular magnetic anisotropy consisting of a $[Co/Ni]_N$ free layer and a fully compensated $[Co/Ni]_N/Ru/[Co/Ni]_N$ synthetic antiferromagnet reference layer separated by a Cu spacer. Following the results reported in Chapter 3, flexible Co/Ni-based GMR spin valves were prepared by direct deposition on Teonex® tapes. Reference samples were also prepared by depositing the Co/Ni-based stacks on rigid SiO_2/Si(100) substrates. The magnetic, magneto-resistance and morphological properties were investigated.

4.1. Co/Ni-based SAF thin film stacks

$[Co/Ni]_N/Co/Ru/Co/[Ni/Co]_N$ SAF thin film stacks with variable Ni layer thickness (t_{Ni}) and bilayer number (N) were deposited on both SiO_2/Si (100) and flexible Teonex® substrates by using different buffer-layers (i.e. Ta/Pd, and Cu) with the aim to optimize the magnetic properties of the SAF building block and investigate to which extent they are influenced when the film stacks are deposited on the flexible tapes. Throughout this study the Ru thickness was set to 0.4 nm to maximize the antiferromagnetic coupling (as reported in Chapter 3 for Co/Pd-based systems), while the Co layer thickness

was fixed at 0.2 nm to ensure a high PMA and a low damping in the system [200,243]. A Cu/Ta capping layer was deposited on top to prevent the SAF-topmost layer oxidation.

4.1.1. Co/Ni-based SAF thin film stacks on SiO_2/Si(100) substrates

To investigate the effect of the number of bilayers *N*, $[Co(0.2)/Ni(0.6)]_N/Co(0.2)/Ru(0.4)/Co(0.2)[Ni(0.6)]/Co(0.2)]_N/Cu(2)/Ta(3)$ thin film stacks with a Ta/Pd buffer layer were deposited on SiO_2/Si(100) substrates. Figure 4.1a shows the room temperature out-of-plane field-dependent magnetization loops (M/M_s vs H) as a function of *N*. All the samples show two well defined minor loops corresponding to the individual reversal of the $[Co/Ni]_N$ ferromagnetic layers separated by a wide antiferromagnetic-coupled field region with a zero moment in the whole field range, thus confirming a compensated antiferromagnetic coupling of the layers across the Ru spacer. The interlayer exchange coupling field, H_{ex}, decreased from 400 mT to 300 mT when *N* increased from 4 to 6, due to both the increase of the magnetic layer thickness and saturation magnetization [220] (Table 4.1). From the values of H_{ex} and M_s, the interlayer exchange coupling J_{ex} was evaluated from the relation $\mu_0 H_{ex} M_s t/2$ [15,218,219], where t is the total thickness of the Co/Ni multilayers, H_{ex} is the exchange coupling field and M_s is the saturation magnetization. All the samples show a rather large interlayer exchange coupling ranging in between 0.95 mJm^{-2} (for N = 4) and 1.3 mJm^{-2} (for N = 6), in line with the data reported in literature for Co/Ni-based SAF thin film stacks [243]. Moreover, to investigate the anisotropy of the system, the effective magnetic anisotropy was evaluated from the relation $\mu_0 H_k M_s/2$, where $\mu_0 H_k$ is the anisotropy field, obtained from the extrapolated intersection of the in-plane field-dependent magnetization curve with the saturation value of the out-of-plane hysteresis loop [172] (figure 4.1b). As reported in Table 4.1, the effective magnetic

anisotropy shows a maximum value of 472 KJm^{-3} for SAF thin films stack with N = 6 in lien with eth data reported in the literature [243].

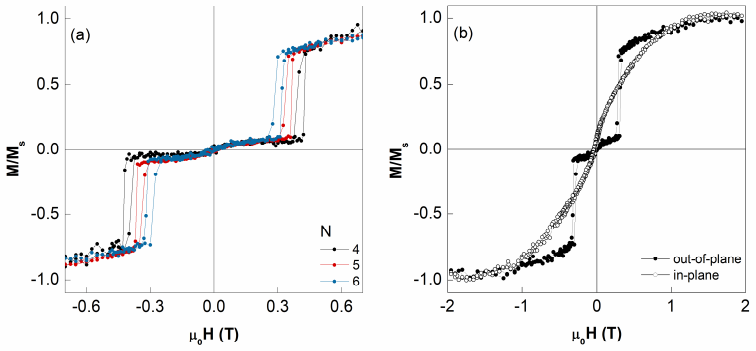

Figure 4.1. (a) Room temperature out-of-plane field-dependent magnetization loops (M/M_s vs H) of $[Co(0.2)/Ni(0.7)]_N/Co(0.2)/Ru(0.4)/Co(0.2)[Ni(0.7)/Co(0.2)]_N$ SAF thin film stacks deposited on $Pd/Ta/SiO_2/Si$ (100) substrates as a function of the repetition number N. Room temperature out-of-plane (– ● –) and in-plane (– ○ –) field-dependent magnetization loops (M/M_s vs H) of sample $[Co(0.2)/Ni(0.7)]_6/Co(0.2)/Ru(0.4)/Co(0.2)[Ni(0.7)/Co(0.2)]_6$ that owns the largest effective magnetic anisotropy K_{eff}.

To investigate the effect of the Ni layer thickness (t_{Ni}), the bilayer repetition was set to 6 as it allows achieving the largest magnetic anisotropy constant while maintaining a wide antiferromagnetic region. The room temperature out-of-plane field-dependent magnetization loops (M/M_s vs H) of SAF thin film stacks deposited on $SiO_2/Si(100)$ substrates as a function of t_{Ni} are reported in Figure 4.2a. They show an almost compensated antiferromagnetic coupling of the layers across the Ru spacer in all the samples as indicated by the two well defined minor loops corresponding to the individual reversal of the $[Co/Ni]_6$ ferromagnetic layers separated by a wide antiferromagnetic-coupled field region with a zero moment in the whole field range. As reported in Table 4.2, H_{ex} decreases from ~350 mT to ~230 mT as t_{Ni} increased from 0.5 nm to 0.8 nm, likely because of an increase

of the magnetic layer thickness[220] . As expected, the saturation magnetization decreases with the decrease of the Co/Ni thickness ratio owing to the larger saturation magnetization of Co ($M_{s,Bulk}^{Co}$= 1422 KAm^{-1}) with respect to Ni ($M_{s,Bulk}^{Ni}$ = 484 KAm^{-1}). A similar behavior was observed for J_{ex} that decreases from 1.4 mJm^{-2} (for t_{Ni} = 0.5 nm) to 1.2 mJm^{-2} (for t_{Ni} = 0.8 nm), in line with the data reported in the literature [243]. By comparing the in-plane and out-of-plane field-dependent magnetization loop (Figure 4.2 b) allows evaluating the effective magnetic anisotropy K_{eff}, which reaches a maximum value of 600 KJ m^{-3} at t_{Ni} = 0.7 nm.

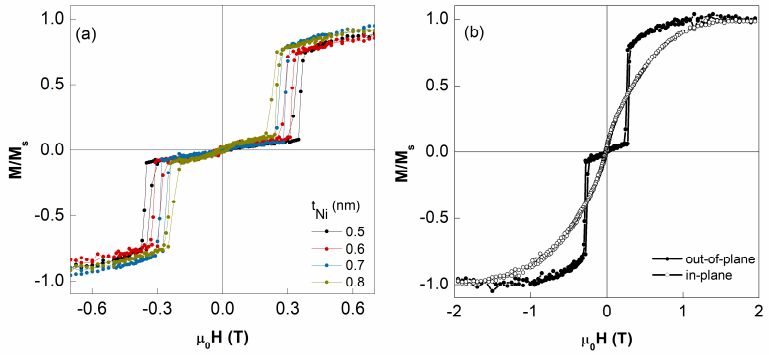

Figure 4.2. (a) Room temperature out-of-plane field-dependent magnetization loops (M/M_s vs H) of [Co(0.2)/Ni(t_{Ni})]$_6$/Co(0.2)/Ru(0.4)/Co(0.2)[Ni(t_{Ni})/Co(0.2)]$_6$ SAF thin film stacks deposited on Pd/SiO_2/Si (100) substrates as a function of Ni layer thickness t_{Ni}. (b) Room temperature out-of-plane (– ● –) and in-plane (– ○ –) field-dependent magnetization loops (M/M_s vs H) of sample [Co(0.2)/Ni(0.7)]$_6$/Co(0.2)/Ru(0.4)/Co(0.2)[Ni(0.7)/Co(0.2)]$_6$ that owns the largest effective magnetic anisotropy K_{eff}.

Table 4.1. Calculated values of H_{ex}, H_c, M_s, J_{ex} and K_{eff} as a function of the repetition number N (t_{Ni} = 0.6 nm) of $[Co/Ni]_N$ SAF thin film stacks deposited on $Pd/Ta/SiO_2/Si$ (100) substrates.

N	H_{ex} (mT)	H_c (mT)	M_s (kAm^{-1})	J_{ex} (mJm^{-2})	K_{eff} (KJm^{-3})
4	400	20	696	0.95	348
5	350	20	770	1.2	424
6	300	15	859	1.3	472

Table 4.2. Calculated values of H_{ex}, H_c, M_s, J_{ex} and K_{eff} as a function of the the Ni layer thickness t_{Ni} (N = 6) of $[Co/Ni]_N$ SAF thin film stacks deposited on $Pd/Ta/SiO_2/Si$ (100) substrates.

T_{Ni} (nm)	H_{ex} (mT)	H_c (mT)	M_s (kAm^{-1})	J_{ex} (mJm^{-2})	K_{eff} (KJm^{-3})
0.5	350	10	897	1.4	540
0.6	300	10	859	1.3	560
0.7	270	20	744	1.2	600
0.8	230	10	842	1.2	500

Based on the above results, $[Co(0.2)/Ni(0.7)]_6/Ru(0.4)/[Co(0.2)/Ni(0.7)]_6$ SAF stacks were used as building blocks for the subsequent studies and the preparation of flexible GMR spin valve heterostructures. The Ni thickness and the number of bilayers were set to 0.7 and 6, respectively, because they are capable of maximizing the effective magnetic anisotropy which can be

relevant to achieve high thermal stability especially for the fabrication of nano-patterned devices, while keeping a wide antiferromagnetic coupled region, which is necessary to guarantee well defined three-steps loops especially when the single layers' coercivity increases in multi-SAF stacks as a result of using buffer layers.

As an alternative to Pd buffer-layer, optimized $[Co(0.2)/Ni(0.7)]_6/Co(0.2)/Ru(0.4)/[Co(0.2)/Ni(0.7)]_6/Co(0.2)/Cu(2)/Ta(3)$ SAF thin film stacks were deposited on Cu buffer-layers, with the aim to prepare and study heavy-metal-free heterostructures. The Cu layer thickness was set to 10 nm to promote the formation of highly (1 1 1) textured Co/Ni multilayers with large PMA while limiting the increase of film roughness in agreement with previous works [243,244]. When a Cu buffer layer is used, both the saturation magnetization (M_s) and the magnetic anisotropy K increases thus resulting in a larger exchange field, exchange energy and coercivity of the individual layer (Table 4.3).

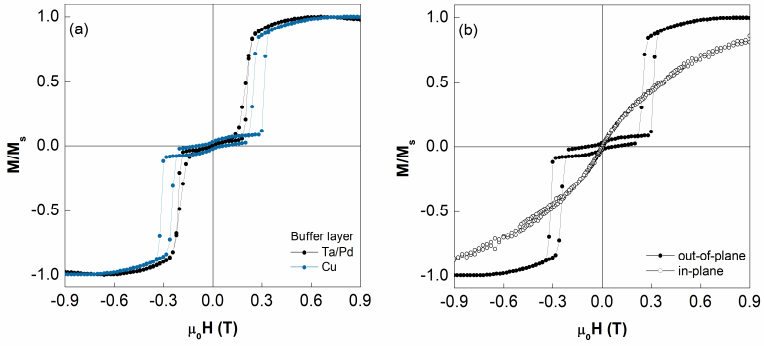

Figure 4.3. (a) Room temperature out-of-plane field-dependent magnetization loops (M/M_s vs H) of $[Co(0.2)/Ni(0.7)]_6/Co(0.2)/Ru(0.4)/Co(0.2)[Ni(0.7)/Co(0.2)]_6$ SAF thin film stacks deposited on SiO_2/Si (100) substrates with different buffer-layers. (b) Room temperature out-of-plane (– ● –) and in-plane (– ○ –) field-dependent magnetization loops (M/M_s vs H) of the $[Co(0.2)/Ni(0.7)]_6/Co(0.2)/Ru(0.4)/Co(0.2)[Ni(0.7)/Co(0.2)]_6$ SAF thin film stack deposited on Cu/SiO_2/Si (100).

Table 4.3. Calculated values of H_{ex}, H_c, M_s, J_{ex} and K_{eff} of $[Co/Ni]_N$ SAF thin film stacks deposited on different buffer-layers on SiO_2/Si (100) substrates.

Buffer layer	**H_{ex} (T)**	**H_c (mT)**	**M_s (kAm^{-1})**	**J_{ex} (mJm^{-2})**	**K_{eff} (KJm^{-3})**
Ta/Pd	190	10	500	0.5	250
Cu	280	55	752	1.2	583

4.1.2. **Flexible Co/Ni-based SAF thin film stacks on Teonex® tapes**

The same SAF thin film stacks were simultaneously deposited on flexible Teonex® tapes to investigate the effect of the substrate. When deposited on the flexible substrate, the main magnetic features were maintained as confirmed from the out-of-plane and in-plane field-dependent magnetization loops (figures 4.4). Moreover, a similar behavior was observed for the trends of H_{ex}, M_s and J_{ex} as a function of t_{Ni}, N and buffer layer (Tables 4.4, 4.5 and 4.6). The main differences with respect to the reference samples are a less sharp switching of the magnetization and the decrease in the coercivity of the ferromagnetic layers and the interlayer exchange coupling field, which are likely due to a higher interface roughness driven by the larger surface roughness of Teonex® tapes (~0.7 nm) with respect to SiOx/Si(100) (~0.3 nm).

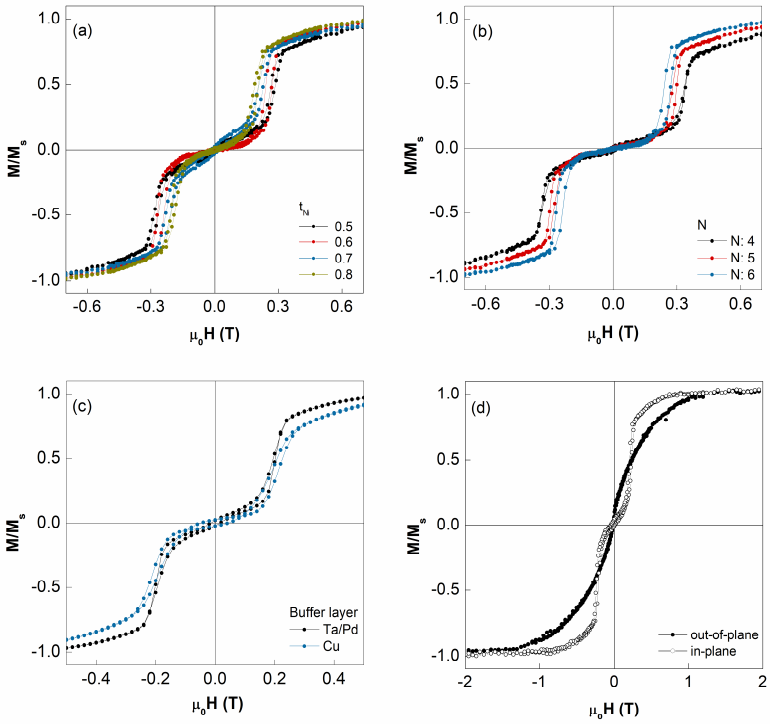

Figure 4.4. (a, b and c) Room temperature out-of-plane field-dependent magnetization loops (M/M_s vs H) of SAF thin film stacks deposited on Teonex® tapes. (a) Effect of Ni layer thickness t_{Ni} (buffer-layer: Ta/Pd), (b) Effect of bilaye repetition number N (buffer-layer: Ta/Pd); (c) Effect of buffer-layer effect; (d) Representative room temperature out-of-plane (– ● –) and in-plane (– ○ –) field-dependent magnetization loops.

Table 4.4. Calculated values of H_{ex}, H_c, M_s, J_{ex} as a function of the repetition number N (t_{Ni} = 0.6 nm) of $[Co/Ni]_N$ SAF thin film stacks deposited on Pd/Ta/Teonex tapes®.

N	**H_{ex} (mT)**	**H_c (mT)**	**M_s (kAm^{-1})**	**J_{ex} (mJm^{-2})**
4	330	5	750	0.85
5	290	10	765	0.95
6	250	20	730	0.95

Table 4.5. Calculated values of H_{ex}, H_c, M_s, J_{ex} as a function of the Ni layer thickness t_{Ni} (N = 6) of $[Co/Ni]_N$ SAF thin film stacks deposited on Pd/Ta/Teonex tapes®.

T_{Ni} (nm)	**H_{ex} (mT)**	**H_c (mT)**	**M_s (kAm^{-1})**	**J_{ex} (mJm^{-2})**
0.5	270	10	870	1.05
0.6	250	20	730	0.95
0.7	220	15	783	0.95
0.8	190	10	680	0.8

Table 4.6. Calculated values of H_{ex}, H_c, M_s, J_{ex} of $[Co/Ni]_N$ SAF thin film stacks deposited on different buffer-layers Teonex tapes®.

Buffer layer	H_{ex} (T)	H_c (mT)	M_s (kAm^{-1})	J_{ex} (mJm^{-2})
Ta/Pd	170	5	755	0.7
Cu	190	10	666	0.7

4.2. PMA Co/Ni SAF-based GMR spin valves

Flexible Co/Ni-based GMR spin valve heterostructures with a $[Co(0.2)/Ni(0.7)]_6/Co(0.2)/Ru(0.4)/Co(0.2)/[Ni(0.7)]/Co(0.2)]_6$ SAF reference layer and a $Co(0.2)/Ni(0.7)]_2/Co(0.2)$ were prepared by direct deposition on Teonex® tapes, and the effect of different buffer and capping layers on the magnetic and magneto-resistance properties was investigated. Reference samples were also prepared on SiO_2/Si (100) substrates.

4.2.1. Co/Ni-based GMR spin valves on SiO_2/Si(100) substrates

Effect of buffer layer

To investigate the effect of the buffer layer on the magnetic and magneto-resistive properties of Co/Ni-based PMA-GMR spin valves, thin film stacks with different buffer-layers (Ta/Pd and Cu) were deposited on rigid SiO_2/Si (100) substrates and a Cu/Ta capping layer was used for all the samples. The room temperature out-of-plane M/M_s vs H loops are shown in top panels of figure 4.5. A three-step field-dependent magnetization response associated to the individual sharp switching of the top layer of the reference electrode (*top* SAF-RL), the FL and the bottom layer of reference layer (*bottom* SAF-RL) is observed in all samples, thus confirming the high

reproducibility of the fabrication process on the different buffered-SiO_2/Si substrates, which ensures a large PMA and smooth interfaces to achieve the expected magnetization configuration as a function of the external field. The corresponding magneto-resistive curves (figure 4.5, bottom panels) show the typical behavior expected for a PMA spin-valve with a SAF reference layer. The GMR ratio shows a sudden increase in correspondence of the first jump in the hysteresis loop (at ~0.26 T for Cu buffer layer, 0.21 T for Pd buffer layer) thus indicating that the top SAF-RL switches first likely because of a slightly higher magnetic anisotropy of the bottom layer of the SAF that is directly grown on buffer-layer. The GMR ratio then sharply reduces to its minimum value in correspondence with the magnetization reversal of the FL (at ~0.021 T for Pd and ~0.034 T for Cu buffer layers). As the absolute value of the magnetic field increases further, a small kink is observed in the high field region corresponding to the GMR effect within the SAF-RL. The maximum GMR ratio of the whole stack significantly decreased from ~4.7 % for Pd buffer layer to ~2.4 % for Cu buffer layer. Despite the absence of non-magnetic heavy metals when using a Cu buffer-layer, the stack presents a reduced GMR ratio, which might be due to a lager interface roughness driven by a large surface roughness of the Cu buffer-layer [200,243,245].The increased roughness might also contribute to the larger coercivity of the individual layers observed when a Cu buffer-layer is used ($H_{c,SAF}^{Cu}$ = 40 mT, $H_{c,SAF}^{Pd}$ = 15 mT, $H_{c,FL}^{Cu}$ = 30 mT, $H_{c,FL}^{Pd}$ = 15 mT).

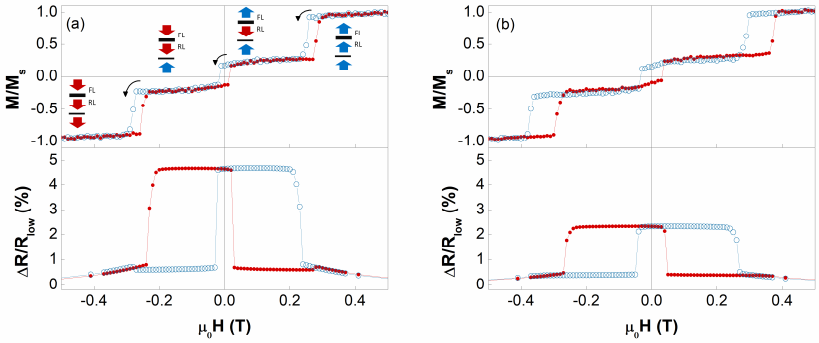

Figure 4.5. Room temperature magnetic and magneto-electric properties of Co/Ni-based GMR-SV thin film stacks deposited on SiO_2/Si (100) substrates with different buffer-layers: (a) Ta/Pd and (b) Cu. For both samples a Cu/Ta capping layer was used. Top and bottom panels reports respectively on the room temperature out-of-plane hysteresis loops (M/M_s vs H) and the corresponding magneto-resistance (MR) response ($\Delta R/R_{low}$ vs H). Different colors and symbols are used for the upward and downward branches of both the hysteresis loops and MR curves to evidence the field sweep direction. The arrows reported in the top panel of figure (a) denote the mutual alignment of the magnetization in the FL, *top*-RL and *bottom*-RL at different points in the loop; the same evolution of the magnetic configuration is observed in both samples.

Effect of capping layer

To study the effect of the capping layer, which plays a critical role in contributing at the stabilization of the perpendicular magnetic anisotropy of the free layer [246,247], the properties of GMR-SV thin film stacks with a Pd buffer-layer, yielding to the largest GMR ratio, and different capping layers (Cu/Ta, Pd) were compared. The room temperature out-of-plane magnetization loops and the corresponding magneto-resistive curves (figure 4.6) show the expected shape in both the cases thus suggesting that both the capping layers contribute to the stabilization of the PMA in the free layer. As well reported in the literature, the Pd layer induces indeed a strong interfacial anisotropy that serves to rotate and stabilize the magnetization

of the Co layer out-of-plane. Concerning the Cu/Ta capping layer, the formation of a CuO_x/TaO_x capping layer as a consequence of the natural oxidation of Cu/Ta might be responsible for the stabilization of the PMA in the free layer, through the hybridization of the Co and O orbitals [248]. However, when a Pd capping was used, the GMR ratio decreases to 3 % for Pd capping layer, due to the larger spin-orbit scattering induced by the non-magnetic Pd layer [249].

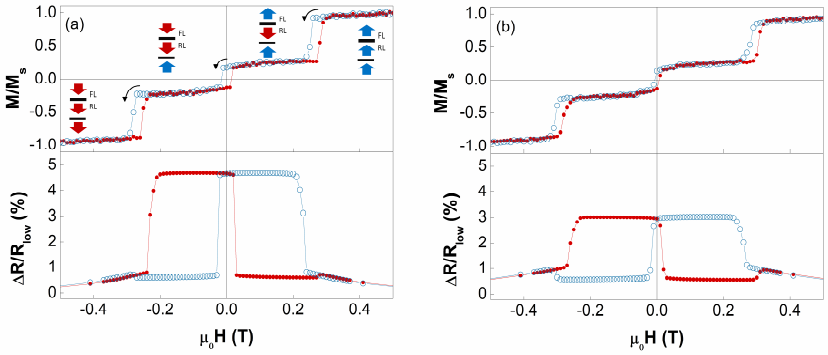

Figure 4.6. Room temperature magnetic and magneto-electric properties of Co/Ni-based GMR-SV thin film stacks deposited on Pd/Ta/SiO_2/Si (100) with different capping-layers: (a) Cu/Ta and (b) Pd. Top and bottom panels report respectively on the room temperature out-of-plane hysteresis loops (M/M_s vs H) and the corresponding magneto-resistance (MR) response ($\Delta R/R_{low}$ vs H). Different colors and symbols are used for the upward and downward branches of both the hysteresis loops and MR curves to evidence the field sweep direction. The arrows reported in the top panel of figure (a) denote the mutual alignment of the magnetization in the FL, *top*-RL and *bottom*-RL at different points in the loop; the same evolution of the magnetic configuration is observed in both samples.

4.2.2. **Flexible Co/Ni-based GMR spin valves on Teonex® tapes**

The same GMR-SV thin film stacks were simultaneously deposited on flexible Teonex® tapes to investigate the effect of the substrate. When deposited on the flexible tape, the main features of the magnetic hysteresis loops (the

three-steps reversal behavior of the magnetization) and the typical behavior of the MR curve for a GMR SV with a SAF reference layer were maintained as compared to the reference samples figures 4.7 and 4.8. The major differences are the switching of the magnetization that is not as sharp as for the reference samples which is in turn reflected in the shape of the corresponding MR curves that became rounded rather than straight implying a slight deterioration in the PMA. Moreover, the free-layer coercivity slightly reduces resulting a narrowing of the plateau in the high-resistance region of the MR curves used ($H_{c,SAF}^{Cu}$ = 25 mT, $H_{c,SAF}^{Pd}$ = 15 mT, $H_{c,FL}^{Cu}$ = 10 mT, $H_{c,FL}^{Pd}$ = 10 mT). The GMR ratio manifested the largest value (~4.5 %) for the SV with a Ta/Pd buffer layer and a Cu/Ta capping layer while lower values of (~2.2 %) for the SV with a Cu buffer layer and (~3 %) for the SV with a Pd capping were reported. All the observed changes could be ascribed to a higher surface roughness of Teonex® (0.7 nm) with respect to SiO_2/Si (100) substrates.

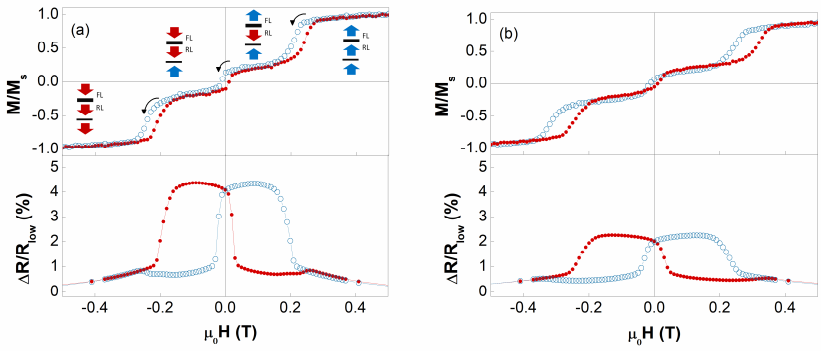

Figure 4.7. Room temperature magnetic and magneto-electric properties of Co/Ni-based GMR-SV thin film stacks deposited on flexible Teonex® tapers with different buffer-layers: (a) Pd and (b) Cu. For both samples a Cu/Ta capping layer was used. Top and bottom panels report respectively on the room temperature out-of-plane hysteresis loops (M/M_s vs H) and the corresponding magneto-resistance (MR) response ($\Delta R/R_{low}$ vs H). Different colors and symbols are used for the upward and downward branches of both the hysteresis loops and MR curves to evidence the field sweep direction. The arrows reported in the top panel of figure (a) denote the mutual alignment of the magnetization in the FL, *top*-RL and *bottom*-RL at different points in the loop; the same evolution of the magnetic configuration is observed in both samples.

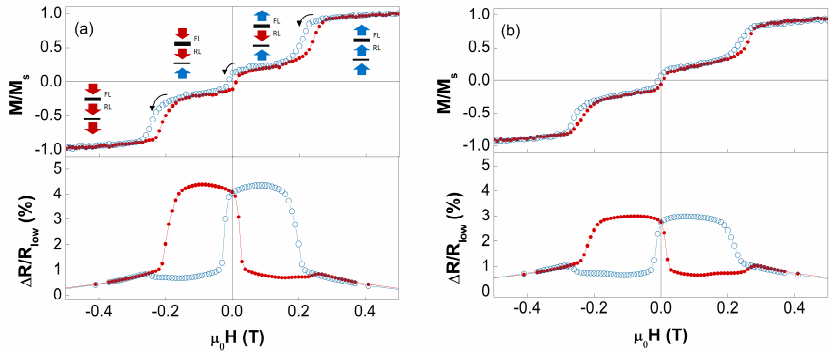

Figure 4.8. Room temperature magnetic and magneto-electric properties of Co/Ni-based GMR-SV thin film stacks deposited on Pd/Ta/Teonex® tapes with different capping-layers: (a) Cu/Ta and (b) Pd. Top and bottom panels report respectively on the room temperature out-of-plane hysteresis loops (M/M_s vs H) and the corresponding magneto-resistance (MR) response ($\Delta R/R_{low}$ vs H). Different colors and symbols are used for the upward and downward branches of both the hysteresis loops and MR curves to evidence the field sweep direction. The arrows reported in the top panel of figure (a) denote the mutual alignment of the magnetization in the FL, *top*-RL and *bottom*-RL at different points in the loop; the same evolution of the magnetic configuration is observed in both samples.

4.3. Conclusions and perspectives

$[Co/Ni]_N/Ru/[Co/Ni]_N$ SAF thin film stacks were prepared on SiO_2/Si (100) substrates and Teonex® tapes and the effects of the number of bilayers, the Ni layer thickness and the buffer layer on the magnetic properties were investigated. The magnetic anisotropy was maximized for a 0.7 nm thick Ni layer and a number of bilayers of 6. To prepare GMR spin valves with perpendicular magnetic anisotropy, the optimized SAF thin film stack and a $[Co/Ni]_2$ were coupled through a 3 nm Cu spacer, and the effect of different buffer (Ta/Pd and Cu layers) and capping layers (Pd and Cu/Ta layers) was investigated. When deposited on rigid SiO_2/Si (100) substrates, the magnetic and magnetoresistance measurements revealed the characteristics of a GMR spin valve with a SAF reference layer for both buffer layers. A maximum

GMR ratio of ~4.7 % was obtained for a Ta/Pd buffer layer, while it reduced to ~2.4 % for a Cu buffer layer which could be attributed to a lager interface roughness driven by a large surface roughness of the Cu buffer-layer. As for the capping layer effect (Pd and Cu/Ta layers), we observed that both capping layers contribute to the stabilization of the PMA in the free layer. In particular, the use of a Pd layer might be capable of inducing a strong interfacial anisotropy that serves to rotate and stabilize the magnetization of the Co layer out-of-plane; whereas, the formation of a CuO_x/TaO_x capping layer as a consequence of the natural oxidation of Cu/Ta might be responsible for the stabilization of the PMA in the free layer, through the hybridization of the Co and O orbitals when a Cu/Ta was used. A reduction of the GMR ratio from ~4.5 % (Cu/Ta capping layer) to 3 % for Pd capping layer was reported due to the larger spin-orbit scattering induced by the non-magnetic Pd layer. The GMR SV stacks were also deposited on flexible Teonex® tapes by using the direct deposition approach. When deposited on flexible substrates, the main magnetic and magnetoresistance characteristics of the GMR SVs were maintained. The major differences with respect to the reference samples are the unsharp switching of the magnetization, which was also reflects in the shape of the MR curves that became rounded rather than straight. Moreover, the free-layer coercivity slightly reduces resulting in a narrowing of the plateau in the high-resistance region of the MR curves. All these differences could be related to a higher surface roughness of Teonex® (0.7 nm) with respect to SiO_2/Si (100) substrates (~0.3 nm).

Chapter 5.

Perpendicularly magnetized Co/Pd-based synthetic antiferromagnetic micro/nanodisks

This chapter reports on the fabrication of Co/Pd-based synthetic antiferromagnetic microdisks with perpendicular magnetic anisotropy of potential interest for therapeutic and diagnostic applications in biomedicine. The focus is on the study and optimization of the properties of thin film stacks consisting of multiple repeats of Co/Pd-based SAF units grown on a sacrificial resist layer spin-coated on SiO_2/Si (100) substrates, which allows for the preparation of free-standing disks after its dissolution. The properties of SAF microdisks fabricated by using both bottom-up and top-down lithography processes are discussed. In the last part, preliminary tests about the use of the nanosphere lithography for massive production of SAF nanodisks are also reported.

5.1. Co/Pd-based Multi-SAF thin film stacks with perpendicular anisotropy

Starting from the results reported in Chapter 3, $[Pd(0.9)/Co(0.4)]_4/Ru(0.4)/[Co(0.4)/Pd(0.9)]_4$ SAF thin film stacks with optimized magnetic properties were used as building blocks for the preparation of thin film multi-stacks consisting of multiple repeats (M = 1, 3, 5, 6, 8) of the single SAF unit. As a first step, the effect of the Au/resist

underlayer on the morphological and magnetic properties of a single SAF unit was investigated. As reported in figure 5.1a, the presence of the Au/resist underlayer leads to a slight deterioration of the magnetic properties with respect to the thin film stack grown on Si/SiO_2. A strong antiferromagnetic coupling is still present, but we observed an increase of the minor loop coercivity (from ~65 to ~90 mT) most likely induced by the higher film roughness. The higher roughness can also affect the magnetic properties of the bottom and top layers of the SAF structure, which can have a slightly different magnetic moment that leads to the appearance of a non-zero-moment plateau in the AF coupling field region. Nevertheless, the stack still presents a marked perpendicular magnetic anisotropy, as evidenced by the shape of the in-plane field-dependent magnetization loop (Figure 5.1b), making it a suitable building-block for the preparation of SAF multi-stack samples with Au/resist underlayer.

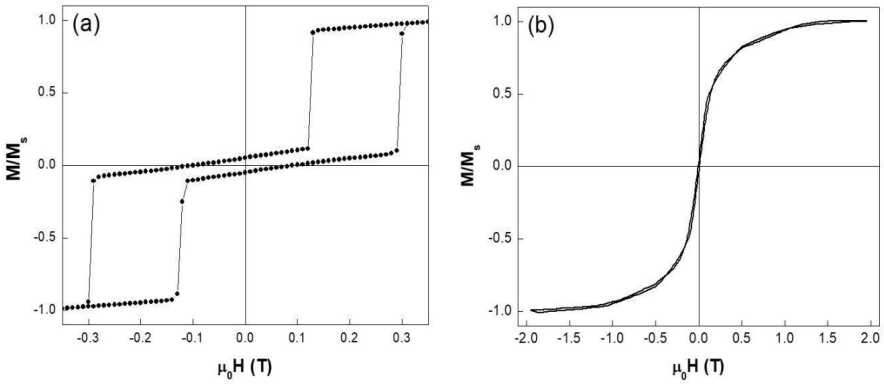

Figure 5.1. Room temperature (a) out-of-plane and (b) in-plane field-dependent magnetization loops (M/Ms vs H) of a $[Co/Pd]_4$/Ru(0.4 nm)/$[Co/Pd]_4$ SAF film deposited on Au/resist/SiO_2/Si.

This was confirmed from the XRR results (figure 5.2 and Table 5.1 right and left panels) which showed, as a general trend, that Au/resist samples reveal always higher roughness values of the layer interfaces with respect to SiO_2/Si

samples. The experimental XRR curves (open dots) of $[Co/Pd]_4$/Ru(0.4 nm)/$[Co/Pd]_4$ samples deposited on Au/resist and SiO_2/Si are reported in figure 5.2 with superimposed the results of the software simulation (color continuous curve). Thickness (t), roughness (σ) and density (ρ) values of each layer as estimated by the Leptos software package for the XRR data fitting are reported in the left and right panels of Table 5.1 for the Au/resist and SiO_2/Si, respectively. It is worth to note that in the physical theory for XRR curve interpretation, interface roughness (σ) is the mean-squared amplitude density fluctuations at the interface with respect to a reference level. Therefore, very small roughness values ($\sigma < 0.01$ nm) are typical of flat interfaces, while $\sigma > 1$ nm is peculiar for rough interfaces. In the investigated multilayer, the Pd/Co periodic layers deposited on SiO_2/Si have flat interfaces, that tend to become rougher in the sample deposited on Au/resist. This latter effect can be ascribed to the rough Au layer ($\sigma = 1.25$ nm) in the Au/resist sample that influences the interface roughness of all overlying layers.

The higher roughness can also affect the magnetic properties of the bottom and top layers of the SAF structure, which can have a slightly different magnetic moment that leads to the appearance of a non-zero-moment plateau in the AF-coupled field region. Nevertheless, the stack still presents a marked perpendicular magnetic anisotropy, as evidenced by the shape of the in-plane field-dependent magnetization loop (figure 5.1b), making it a suitable building-block for the preparation of PMA-SAF multi-stack samples with Au/resist underlayer.

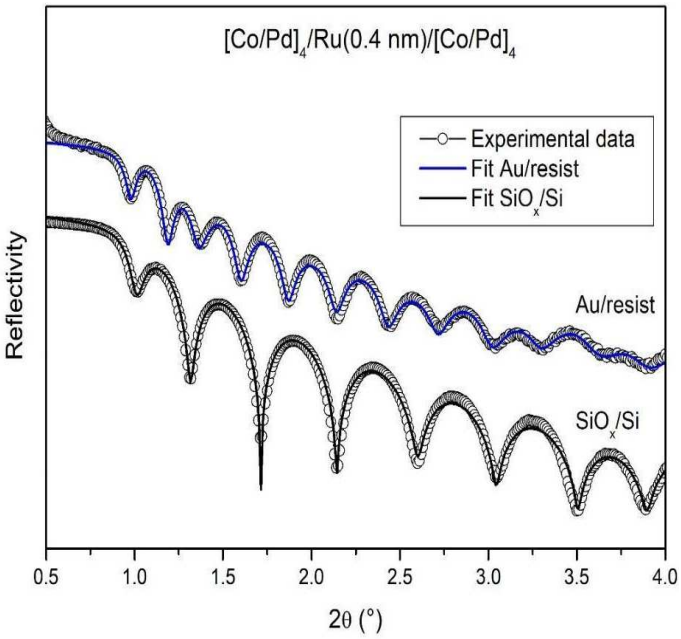

Figure 5.2. XRR experimental data (open dots) and best fitting (continuous line) for $Co/Pd]_4/Ru(0.4\ nm)/[Co/Pd]_4$ samples deposited on Au/resist and SiO_2/Si.

Table 5.1. Software simulation results of the XRR curve fitting of the SiO_2/Si and Au/resist sample. *N* is the layer number starting from the top surface, *R* is the layer repetition, SUB is the substrate, while *t*, *σ* and *ρ* are the software estimated values of thickness, roughness and density, respectively.

N	R	Material	t ± 3% (nm)	σ ± 10% (nm)	ρ ± 5% (g/cm³)	N	R	Material	t ± 3% (nm)	σ ± 10% (nm)	ρ ± 5% (g/cm³)
1	1	Pd	2.50	0.17	13.2	1	1	Pd	2.25	0.44	11.9
2	4	Pd	0.97	1.00	11.7	2	4	Pd	0.92	0.006	11.5
3	4	Co	0.40	0.94	10.7	3	4	Co	0.40	0.057	10.2
4	1	Ru	0.50	0.04	12.8	4	1	Ru	0.40	0.001	11.3
5	4	Co	0.37	0.34	7.6	5	4	Co	0.48	0.004	10.4
6	4	Pd	0.91	0.35	11.7	6	4	Pd	0.93	0.090	11.8
7	1	Pd	2.46	0.76	11.2	7	1	Pd	2.09	0.005	12.4
8	1	Ta	2.72	0.98	16.7	8	1	Ta	2.74	0.42	17.9
9	1	Au	9.01	1.25	18.6	9	1	SiO_2	106	0.33	2.14
10	1	Resist	31.2	0.24	0.86	SUB	1	Si	0.00	2.11	2.33
11	1	SiO_2	117	0.67	2.43						
SUB	1	Si	0.00	1.52	2.33						

After studying the effect of Au-induced roughness, film samples consisting of multiple repeats *M* (= 1, 3, 5, 6, 8) of $[Co/Pd]_4$/Ru(0.4 nm)/$[Co/Pd]_4$ SAF units with Au/resist underlayer were prepared and the resulting room temperature out-of-plane field-dependent magnetization loops are shown in figure 5.3a. The magnetization was normalized to the samples' surface area in order to allow a comparison among the samples and evidence the effect of the repetition number *M* on the magnetic properties. A two-step magnetic reversal behavior and a wide AF-coupled field region are clearly retained up to M = 5. However, magnetization loops of multi-stack thin films with M = 3 and M = 5 do not consist of a perfect superposition of identical hysteresis loops of fully decoupled single SAF units (M = 1) as indicated by the slight differences between the shape of the three loops. In particular, the transition from the parallel (P) to the antiparallel (AP) state and vice versa becomes more and more slanted with the increase of the repetition number M, which also results in a gradual enhancement of the minor loop coercivity. These effects can be the result of a gradual variation of the

properties of consecutive SAF units. The analysis of the hysteresis loops also indicates that the non-zero moment in the AF-coupled field region clearly visible in the single SAF film (M = 1) is no more evident when the number of repetition M is increases, thus indicating that its contribution to the total magnetic signal becomes negligible with significant advantages for biomedical applications. At a closer inspection of the AF-coupled field region (figure 5.3b), it results that samples with M = 1, 3 and 5 present a very similar magnetic signal in the AF-coupled field region in terms of shape and magnitude. This result suggests that the non-zero moment in the AF-coupled field region comes from the first single SAF unit due to the slight difference of the magnetic properties of the bottom and top layer, the former being most affected by the Au underlayer [148].

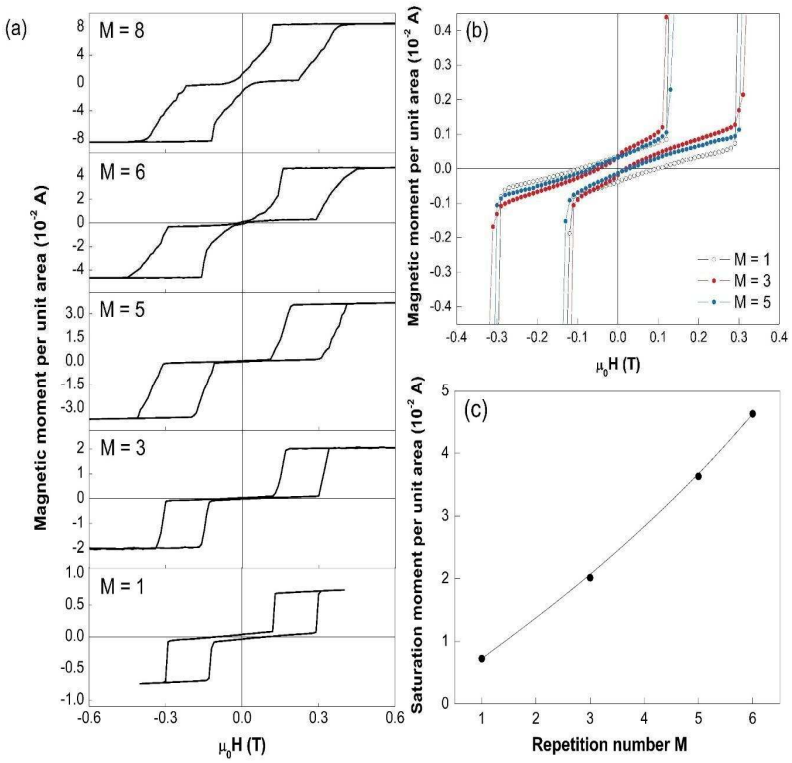

Figure 5.3. (a) Room temperature out-of-plane field-dependent magnetization loops of $\{[Co/Pd]_4/Ru(0.4\ nm)/[Co/Pd]_4\}_M$ multi-stack thin films (M = 1, 3, 5, 6, 8) deposited on Au/resist/SiO_2/Si. The magnetization is normalized to the sample surface area. (b) Magnification of the AF-coupled field region of the hysteresis loop of samples with M = 1, 3 and 5. (c) Evolution of the saturation moment per unit are as a function of the repetition number M.

Increasing M up to 6, the two-step magnetic reversal behavior is still present, however, a tail appears in the minor loops in correspondence of the end of both the AF–F and F–AF transitions, the latter causing a narrowing of the AF-coupled field region. This result can be the consequence of a further deterioration of the interfaces quality, which is expected to modify the magnetic moment of the single units, with a possible magnetostatic interaction that may affect the magnetization reversal mechanism of the

system as a whole. This effect become even more evident in the sample with M = 8, where Hex decreases and a finite and strong moment at remanence appears. Hence, M = 6 can be considered a threshold value, the best properties being obtained for the sample with M = 5, which also preserves a strong PMA, as confirmed by comparing in-plane and out-of-plane field-dependent magnetization loops in figure 5.4. In summary all key criteria required for biomedical applications, i.e., zero remanence, zero field susceptibility at small fields, and sharp magnetization reversal to saturation, are maintained for samples up to M = 5. Moreover, as shown in figure 5.3c, the magnetic moment per unit of area at saturation can be easily modulated by varying the number of repetitions M without significantly affecting any of the other magnetic properties, thus paving the way for the preparation of high moment PMA-SAF microdisks of interest for different biomedical applications (e.g. mechanical destruction of cells, cell manipulation, microfluids, etc.). As reported in ref. 12 and 13 for similar systems, commercially available magnets can be used to efficiently manipulate the microdisks; moreover, the possibility to vary the moment by changing M, permits adding a further degree of freedom that allows reducing the microdisks diameter while keeping a high magnetic moment if required by specific applications.

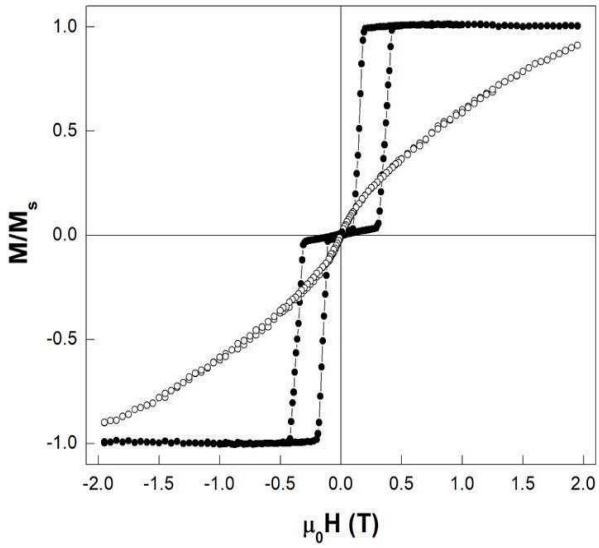

Figure 5.4. Room temperature in-plane and out-of-plane of-plane field-dependent magnetization loops (M/M_s vs H) of the $\{[Co/Pd]_4/Ru(0.4\ nm)/[Co/Pd]_4\}_5$ film.

To explain the observed deterioration of the magnetic properties as a function of repetition number M, cross-sectional TEM imaging was performed on the $\{[Co/Pd]_4/Ru(0.4\ nm)/[Co/Pd]_4\}_8$ sample ($M = 8$) deposited on the Au/resist underlayer (figure 5.5). The eight SAF single units separated by Ta/Pd spacers are clearly visible together with the two Au bottom and top layers. The SAF single units are quite uniform in thickness near the substrate; however, starting from the third layer, the interface roughness enhances with increasing number of SAF units and in the last units the chemical contrast of the Ta/Pd spacers is barely visible. This increasing interface roughness and intermixing will certainly affect the layer quality in particular of the Ru layer and can even result in other magnetic coupling contributions, such as orange peel coupling [250,251]. We believe that this increased interface roughness is the origin of the observed deterioration of the overall magnetic properties with increasing repetition number.

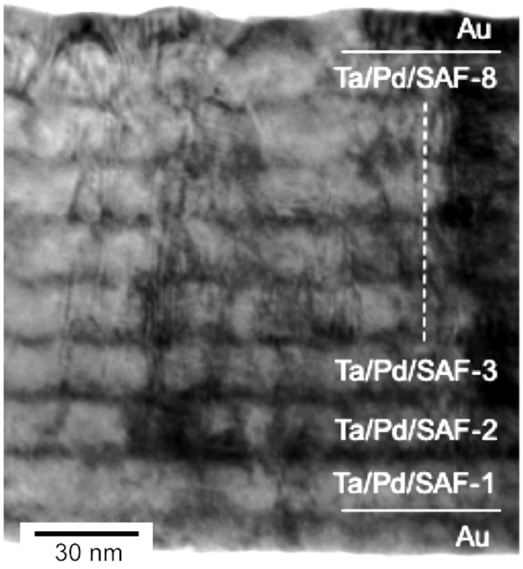

Figure 5.5. Cross-sectional TEM image of a $\{[Co/Pd]_4/Ru(0.4\ nm)/[Co/Pd]_4\}_8$ film sample (M = 8) with Ta/Pd buffer layers separating the SAF units. The SAF multi-stack was deposited on an Au/resist underlayer.

The multi-stack thin film sample with M = 5 showing the most suitable magnetic properties was used to prepare an array of microdisks (diameter: 2 µm, pitch: 4 µm) by combining electron beam lithography and Ar ion-milling (figure 5.6a). The prepared microdisks still reveal the characteristic two-step magnetic reversal behavior of a synthetic antiferromagnet although the magnetic properties are slightly deteriorated as indicated by the appearance of a small hysteretic contribution in the low field region (figure 5.6b). This effect can be probably ascribed to a damage of the edges of the microdisks induced by the Ar ion-milling process [252]. Indeed, Co-based multilayers are strongly sensitive to ion irradiation processes, being the out-of-plane anisotropy highly dependent on the interface microstructure and relatively low ion doses are able to decrease the anisotropy or even change its sign thus moving the easy axis of Co/Pt multilayers into the film plane [253]. Moreover, the presence of microstructural defects as well as the possible

atomic intermixing at the damage regions are expected to vary the value and/or the sign of J_{ex}, thus modifying the reversal behavior characterizing the SAF system. Despite the complex scenario that is expected to occur as a consequence of the etching process, it is to underline that the antiferromagnetic coupling is still able to give an almost compensated magnetization state at zero field while keeping a high magnetization state at about 0.5 T. In addition, it should be mentioned that the cure procedure (e.g., prebake and post-bake processes) of the negative resist used as a mask, has affected the sacrificial resist layer introducing surface ripples and cracks as confirmed from the SEM images of figure 5.7, which can influence the effectiveness of the ion-milling process and hence the final physical properties of the microdisks.

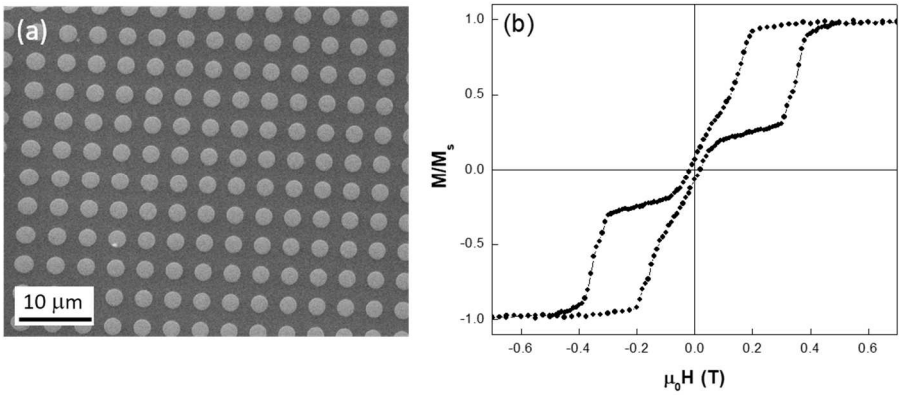

Figure 5.6. (a) Multi-stack (M = 5) microdisks array (diameter: 2 µm, pitch: 4 µm); (b) room temperature field-dependent magnetization loops (M/M_s vs H).

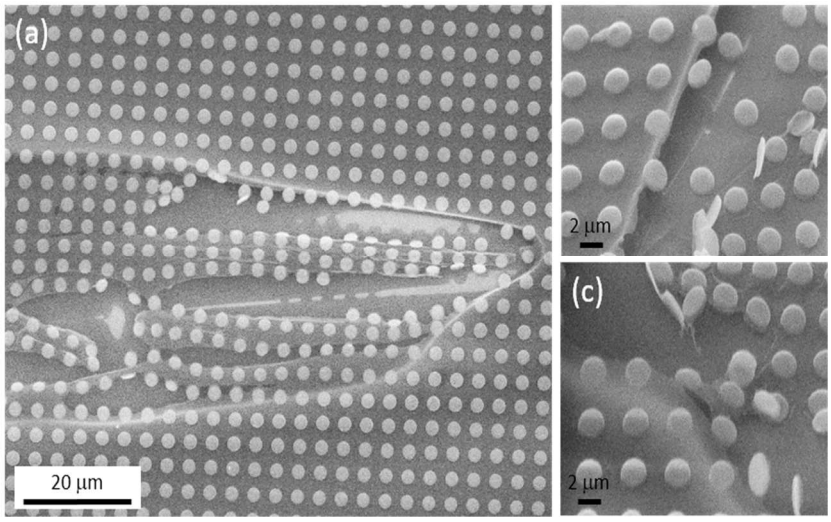

Figure 5.7. SEM images of the patterned microdisks array, showing the resist sacrificial layer defects induced by the curing of the e-beam negative resist.

As an alternative to the top-down strategy, bottom-up approaches were also investigated to prepare SAF microdisks. Au/{Ta/Pd/$[Pd/Co]_4$/Ru/$[Co/Pd]_4$}$_M$/Au (M = 3) thin film stacks were deposited on pre-patterned arrays of microholes with different pitches, initially prepared by combining EBL and lift-off strategies on the resists stack composed of PMMA 669.06/COP 8.5 EL6/LOR B (7B). LOR B is the sacrificial resist while PMMA and COP were used for a better undercut (refer to chapter 2 for the details). After thin film deposition, microdisks array were obtained by removing the PMMA resist together with the continuous film on top.

Figure 5.8 reports on both the pre-patterned substrate with the resist still present and the microdisks array obtained after the lift-off process. Due to the substrate rotation during the sputtering process, a glass-like shape was obtained due to the deposition of the material on the walls of the microholes.

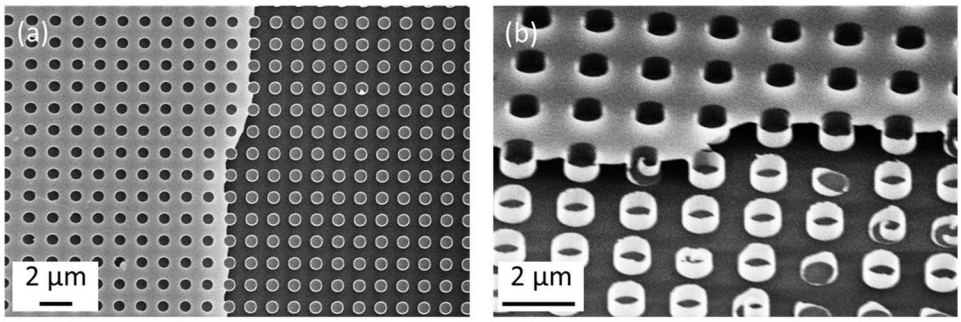

Figure 5.8. SEM images of the patterned arrays of microholes and microdisks (pitch and d ~ 1 µm), showing the microdisks' shape defects induced by the substrate rotation during sputtering: (a) Planar sample and (b) Tilted sample.

Au/{Ta/Pd/[Pd/Co]$_4$/Ru/[Co/Pd]$_4$}$_M$/Au (M = 3) thin film stacks were also deposited on SiO_2/Si (100) (reference sample) without rotating the substrate during the sputtering process. The corresponding room temperature out-of-plane M(H) hysteresis loop, reported in figure 5.9, shows that the magnetic properties slightly deteriorated as indicated from the hysteretic contribution in the low field region. Microdisks composed of the same stacks were then prepared (without substrate rotation). Figure 5.10a shows the SEM image of a well-ordered array of perfectly-shaped microdisks with diameter *d* = 1 µm and lattice periodicity of ~ 4 µm; thus confirming the necessity to stop the substrate rotation during deposition to avoid the glass shape. The corresponding field-dependent magnetization loop is shown in figure 5.10b. compared to the reference samples, the magnetic properties are slightly deteriorated as indicated by the appearance of a small hysteretic contribution in the low field region. Nevertheless, the prepared microdisks still reveal the characteristic two-step magnetic reversal behavior of a synthetic antiferromagnet.

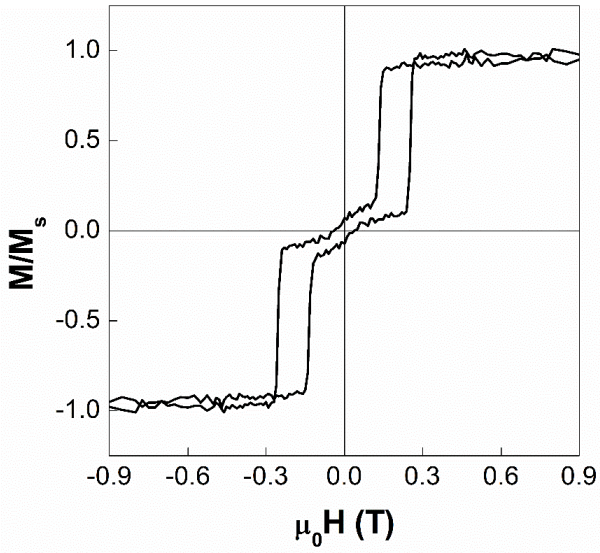

Figure 5.9. Room temperature field-dependent magnetization loops (M/M_s vs H) of Au/{Ta/Pd/[Pd/Co]$_4$/Ru/[Co/Pd]$_4$}$_M$/Au (M = 3) microdisks prepared on SiO_2/Si (100) without rotating the substrate during sputtering.

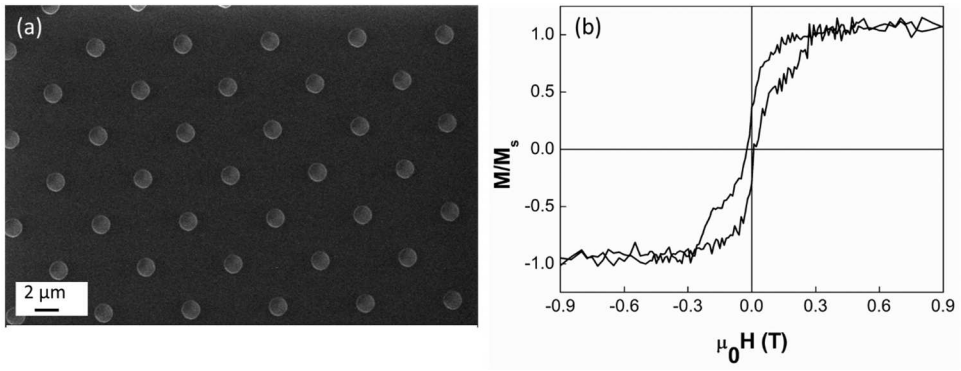

Figure 5.10. (a) Multi-stack (M = 3) microdisks array (diameter: 1 µm, pitch: 4 µm). (b) Room temperature field-dependent magnetization loops (M/M_s vs H).

As final tests, the samples of the microdisk arrays obtained prepared using both bottom-up and top-down EBL strategies were rinsed in proper solvent (i.e. acetone for PMMA and PG remover for LOR B) to dissolve the sacrificial resist and obtain free standing microdisks. Figure 5.11 shows the obtained

microdisks with a diameter of ~ 1 µm. However, due to the small patterned area obtained by EBL it was not possible to collect a significant number of microdisks to be investigated manetically.

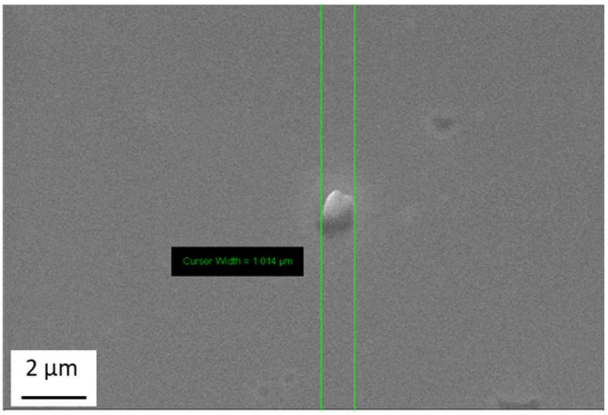

Figure 5.11. SEM image of the microdisks obtained after dissolving the sacrificial resist.

5.2. Conclusions and Perspectives

The possibility to design complex magnetic heterostructures that can be used for biomedical applications has been explored in this study. In particular, the $[Co/Pd]_N$ multilayer system, which is well known for its tunable magnetic properties, was chosen to build up compensated synthetic antiferromagnetic $[Co/Pd]_N/Ru/[Co/Pd]_N$ thin films with perpendicular magnetic anisotropy. These layers are used in a further step as building-blocks to prepare $\{[Co/Pd]_4/Ru/[Co/Pd]_4\}_M$ multi-stacks on an Au/resist underlayer. These SAF film samples fulfill all the key criteria required for biomedical applications, i.e., zero remanence, zero field susceptibility at small fields, and a sharp magnetization reversal to saturation. Moreover, the magnetic moment at saturation can be modulated, without changing the hysteresis main features, by varying the number of repetitions up to M = 6.

Above this value, the interface quality, which gradually reduces with increasing repetition number, is significantly affected, leading to a substantial deterioration of the magnetic properties. The main output of the presented work is the significant versatility and adaptability of this complex system to be grown on different substrates and, in particular, on an Au/resist underlayer that makes it a suitable material for the preparation of free-standing synthetic antiferromagnetic micro-/nanodisks for biomedical applications. In this regard, SAF microdisks were prepared by means of conventional top-down and bottom-up EBL combined with lift-off and/or ion etching processes. The prepared microdisks were still revealing the characteristic two-step magnetic reversal behavior of a synthetic antiferromagnet with slight deterioration of the magnetic properties as demonstrated by the appearance of a small hysteretic contribution in the low field region. Moreover, the potentiality of the tested technique has been demonstrated by obtaining free standing microdisks after dissolving the sacrificial resist although it was impossible to collect a significant number of microdisks for the magnetic characterization due to the small patterned area obtained by EBL. The obtained results impose the necessity for further work to optimize the lithographic process and hence the properties of microdisks with such a complex multi-layered structure. Moreover, for practical applications and massive production of optimized multi-SAF microdisks, lift-off and/or ion etching strategies combined with cost and time-effective lithographic processes are necessary.

The use of lithographic methods based on self-assembled templates from colloidal spheres has emerged as an alternative and intriguing strategy for generating periodic nanostructures with the advantages of low cost, high throughput, easy controllability and no need of complex equipment [254–256] as compared to other nanofabrication techniques such as the expensive EBL. Self-assembly of closely-packed colloidal spheres into two-dimensional (2D) ordered arrays plays a major role for nanotechnologists for a wide range of

applications, going from the fabrication of photonic crystals to plasmonic devices or biomimetic surfaces with specific wettability or reflection properties, just to name a few. Silica and polymer colloids are the most commercially available and most widespread building blocks for 2D crystals due also to their better monodispersity, an important condition for ordered self-assembled structures [257–259]. Nanosphere lithography (NSL) techniques exploiting the use of monolayers of colloidal micro/nanospheres as mask layers combined with ion etching processes have been used to prepare micro/nano-patterned structures [210,260]. Moreover, recently, monolayers of colloidal crystals-assisted photolithography have attracted much attention as a simple and convenient technique to fabricate 2D or 3D nanostructures, using the light scattering/diffraction through colloidal spheres into the photoresist layer [261]. This approach came up with the aim to utilize the self-assembled array of polystyrene (PS) spheres as optical lenses to generate deep sub-wavelength regular patterns on a photoresist. PS spheres have optical indices [262] that are close to the optimum value at the wavelengths used by conventional UV lithography; thus, making them able to focus light into deep subwavelength dimensions [263]. Indeed, an extremely uniform pattern size can be achieved even for relatively poor sphere size uniformity. This approaches allows to avoid the use of ion etching processes utilized in the EBL technique.

A rich variety of techniques is available to produce colloidal particles of quasi-spherical shape and approximately monodisperse in size from different materials such as PS and PMMA [257–259,264]. Such methods differ in terms of area coverage and order properties of the self-assembled monolayers as well as in the complexity of the process and its sensitivity to ambient conditions (e.g. temperature or humidity) that ultimately affect the characteristics of the monolayers.

To allow for a massive production of microdisks, a strategy based on the NSL was developed. The approach is based on the use of self-assembled monolayer arrays of PS microspheres either as mask layers for top-down

lithographic approaches combining ion etching processes or as UV optical lenses to prepare pre-patterned arrays of sub-micron holes for bottom-up approaches combining lift-off processes. To this aim, a preliminary work has been done to obtain self-assembled PS monolayers by using two different strategies: 1) the drop-casting method and 2) the scooping transfer technique. The spheres used in this work were polystyrene latex beads with a diameter of 1.1 µm supplied as aqueous suspensions of 10 % w/w by Sigma-Aldrich.

The drop-casting method is a simple method that can be easily implemented by directly depositing on a target substrate from a drying droplet containing colloidal particles, i.e. dispensation and evaporation of a colloidal drop [265–267]. The scooping transfer technique, on the other hand, is a method that allows producing high quality colloidal monolayers over large areas without the need of any special equipment. The process uses a direct assembly of colloids at the air–water interface in a way that no additional compression of the monolayer is necessary prior transfer. The close-packed monolayer directly forms at the air–water interface and can be transferred to arbitrary substrates simply by immersion of the substrate into the water phase and picking up the monolayer with a transfer substrate of arbitrary material or topography. Thus, the technique presents an essential simplification of the crystallization procedure and holds promise to make colloidal monolayers available wherever needed even to untrained persons.

To form a monolayer of PS spheres, the in-plane drop casting method was first investigated and the effects of different concentrations of the spheres and the amount of the sphere suspensions added were carefully studied. Starting from the 10 % w/w aqueous suspension of polystyrene spheres, 3 different diluted PS suspensions were prepared. The first two suspensions were obtained by diluting the 10 % w/w suspension in deionized water (DI) water down to 0.2 % w/w and 4 % w/w. The third suspension was prepared by diluting the 10 % w/w suspension in DI water down to 4 % w/w and then it was mixed with ethanol to get a 1:4 volume ratio of dispersion:

ethanol. Ethanol was used to facilitate the spreading of PS spheres. To make the surface of the substrate/sample hydrophilic, a positive surface charge was created by immersing the clean substrate/sample in 0.2% (w/v) poly (diallyldimethylammonium) chloride (Sigma-Aldrich) for 30 s to promote the formation of a monolayer of HCP PS spheres directly on top of the substrate/sample. The substrate/sample was then rinsed with water and put on any clean plane and using a pipette, 10 µl of the PS suspension were withdrawn from the prepared solution and drop-casted to the surface of the substrate/sample and left for 2 minutes. Finally, the substrate/sample was rinsed with water and put on a hot plate at 40 ^{o}C until water evaporated. The process is schematically illustrated in figure 5.12a.

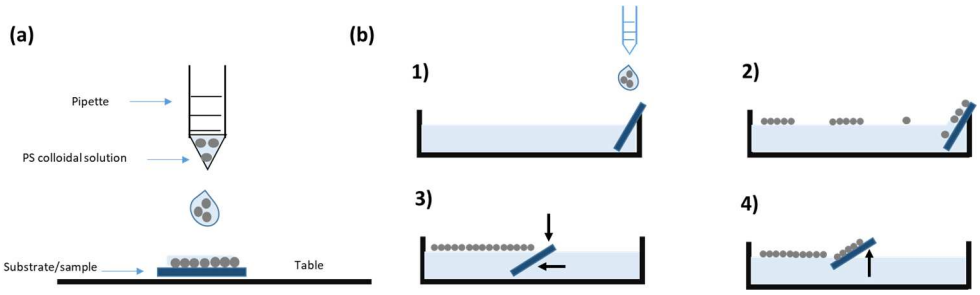

Figure 5.12. Schematic illustration of the monolayer fabrication process. (a) Sketch of the in-plane drop-casting technique. (b) Sketch of the scooping transfer technique: 1) Addition of colloids to the interface via a tilted glass slide inside a Petri dish full with DI water, 2) spreading of the colloidal suspension so as to contact the surrounding water at the edge, 3 and 4) self-assembly of the particles upon addition of a small amount of surfactant and monolayer transfer by immersion of the transfer substrate and subsequent elevation under a shallow angle.

Figure 5.13 shows the SEM images of the results obtained with the drop-casting method with different PS concentrations. Figures 5.13a and b show that the PS spheres accumulated at the edges of the drop forming a ring of multilayers while separate particle patches inside the drop were formed. Moreover, comparing figures 5.13b and 5.13c, we could conclude that a low concentration (0.2 % w/w) of spheres was not enough to produce a

complete monolayer of PS while a higher concentration of spheres (4 % w/w) could assemble more spheres together and form more separate patches of particles but not a complete monolayer and still with multilayers at the edges despite the self-healing effect of particles that tend to form a hexagonal close packing (hcp) structure. Figure 5.13d shows the SEM image of a sample drop-casted starting from a 4 % w/w PS dispersion diluted with ethanol (ratio: 1:4 vol.-% mixture of PS: ethanol) with the aim to facilitate the spreading of the spheres [268]. Using this combination, we obtained regions with a large monolayer of spheres and no multilayers were formed. However, void gaps were still present and we could not obtain a complete monolayer of PS spheres. Indeed, although this approach looks simple, the colloidal pattern formation is a consequence of physical phenomena resulting from a complex interplay of different mechanisms such as evaporative convection, thermal and solutal Marangoni flow and instabilities, advection-diffusion of particles in the drop, interaction forces between the particles and the substrate, wetting phenomena, contact line pinning, depinning and repinning, heat transfer by convection inside the drop and conduction in the substrate, mass transfer through diffusion of liquid vapor in the atmosphere [269]. In particular, the so-called Marangoni effect implies the transformation of physicochemical energy into flow due to variations in the liquid-vapor interfacial tension, where differences in temperature or evaporation rate are responsible for surface tension gradients; generally, a temperature increase induces a decrease in the surface tension, causing flow of the liquid from the hot spots to cooler regions and dimples in a surface drying or solidifying under uneven temperature conditions [266,270,271]. Moreover, the radial flow driven by evaporation mechanism is responsible for the colloidal pattern; in particular, for the so-called coffee ring which consists of the accumulation of particles at the edges of the drop and depletion in the middle [270,271] as clearly observed in figures 5.13a, b and c.

Based on the above results and the related discussion, it can be easily deduced that even if drop-casting is an attractive solution due to its simplicity, control over the final pattern is very difficult. And, to obtain a pattern as close as possible to an hcp pattern, the different flows and interactions intervening in drop casting should be balanced by playing with different parameters in addition to the accurate control and optimization of drying time, particle concentration and drying agents (use of mixed solvents with proper drying control agents) [266].

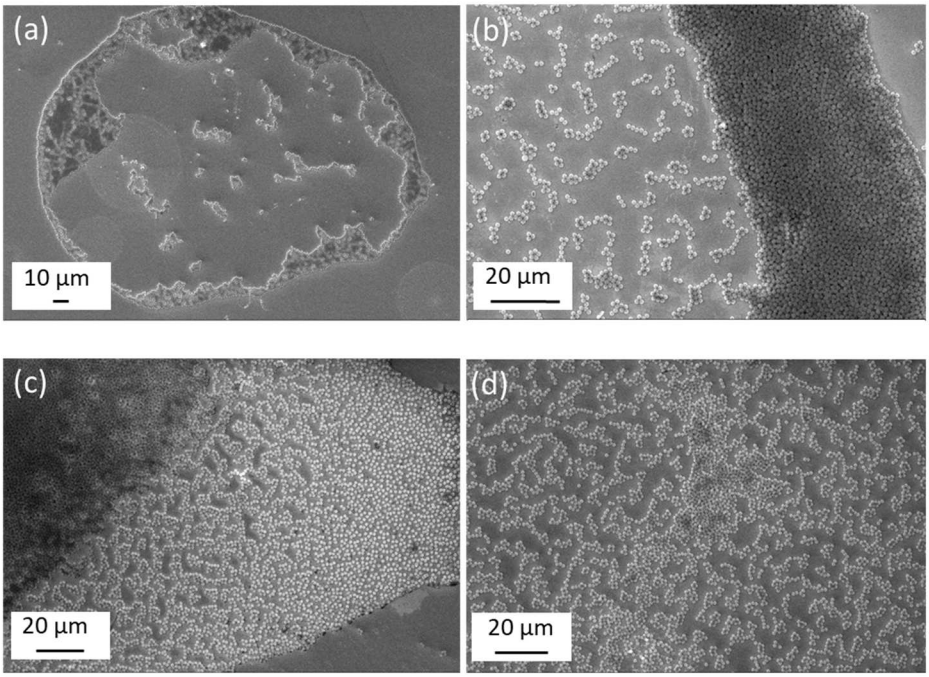

Figure 5.13. Self-assembly of PS colloids by drop-casting method using a colloidal dispersion of: (a) and (b) 0.2% w/w. (c) 0.4% w/w. (d) 1:4:colloids:ethanol.

As an alternative to the drop-casting method, a scooping transfer strategy belonging to self-assembly at the air/water interface approaches was investigated (Figure 5.12b). This technique allows for a sufficient particle mobility required for the formation of large crystalline domains while the

assembly at the interface excludes the formation of multilayer structures [255,268,272]. The scooping transfer process is versatile with respect to colloidal size and substrate material. Transfer to solid substrates is straightforward and conveniently done by hand. There are no special requirements for the substrate except for that it must be sufficiently hydrophilic in order not to completely dewet during the deposition process. Thus, considering the best results obtained above, we started from a 4 % w /w concentrated suspension diluted with ethanol to form a 1:4 vol.% mixture of dispersion. In a glass petri dish, the PS beads were applied to the water surface via a partially immersed hydrophilic glass slide with at a tilt angle of approximately 45 ^{o} with respect to the water surface. Upon spreading, patches of colloidal monolayers formed and remained afloat at the interface of pure water. To help the direct crystallization process, small amounts of sodium dodecyl Sulfate (SDS) were added to the water phase. The monolayer readily formed at the air–water interface could be clearly seen by the bright colorful Bragg reflexes (figure 5.14a). The substrate/sample was immersed in 0.2% (w/v) poly(diallyldimethylammonium) chloride (Sigma-Aldrich) for 30 s to make the surface hydrophilic. After rinsing with water, the substrate/sample was immersed into the petri dish and elevated under a shallow angle to transfer the monolayer, and finally it was dried on a slightly hot plate.

Figures 5.14b shows the SEM image of the PS monolayer arrays obtained after performing the scooping transfer from the air-water interface to the target substrate/sample. Compared to the drop-casting method, patches of continuous 2D well-ordered hcp monolayer arrays of PS colloids were produced over large areas. The used SDS molecules in our work are amphiphilic, they accumulate at the air/water interface and constitute a soft barrier for the colloids added to the interface. This barrier facilitates the packing process of the individual colloidal particles into a hexagonal lattice. On a molecular scale, the particles detaching from the glass slide at the interface are pushing against the floating surfactant layer which in turn

pushes the particles closer together and thus facilitates the nucleation of 2D crystals. This feature has been called ‘‘piston oil effect” [273].

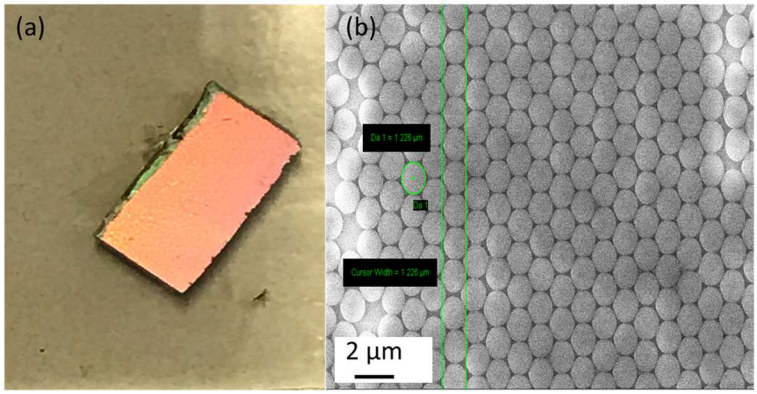

Figure 5.14. Self-assembly of PS colloids by the scooping transfer technique using a colloidal dispersion of 1:4:colloids:ethanol: a) optical photograph of the substrate after collecting the PS monolayer of spheres and b) close-packed monolayer of PS spheres.

To use the PS microsphere array as a mask for the fabrication of microdisks, a further step is necessary to obtain separated beads. To this aim, Ar ion milling was used to selectively reduce the size of the spheres and obtain a mask for further etching processes (As an example, figure 5.15 reports on the Ar ion milling at 300 W power and a bias of 400 V for about 30 seconds that was performed). The SEM image shows that the spheres’ diameter was reduced from 1.1 µm to about 870 nm.

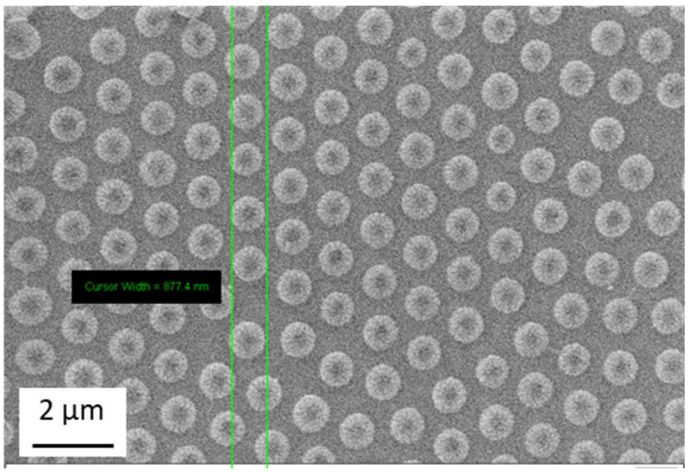

Figure 5.15. SEM image reporting on an example of the obtained spheres upon performing an Ar ion milling process to reduce the spheres' diameter.

As an alternative approach, self-assembled arrays of PS spheres were used as UV optical lenses to fabricate pre-patterned substrates of sub-micron holes. To this aim, LOR B (7B)/LOR A (1A)/S1811 resists' stack consisting of three different layers was spin-coated and baked on Si substrates (see table 5.2 for details about the conditions used). LOR B was used as a sacrificial resist that allows obtaining the micro/nanodisks after its dissolution in PG remover while the dual resists LOR A (Lift-off resist A which is based on polydimethylglutarimide PMGI) and Shipley resist S1811 were used to get a better undercut. The undercut is required to achieved good lift–off. This is achieved by creating defined gap between the deposited film on the substrate and the resist surface, via a bilayer resist [206]. Using the scooping transfer technique, an hcp array of PS spheres was then self-assembled on top of the resists and exploited as optical lenses to UV-expose the resists using a conventional photolithography tool "Mask Aligner" with a wavelength of 315 nm for 1 s. Finally, the patterned holes were obtained by removing the PS spheres by sonication for 2 minutes in DI water and developing the dual resists for 30 seconds in MF319. A schematic illustration of the fabrication process is reported in figure 5.16.

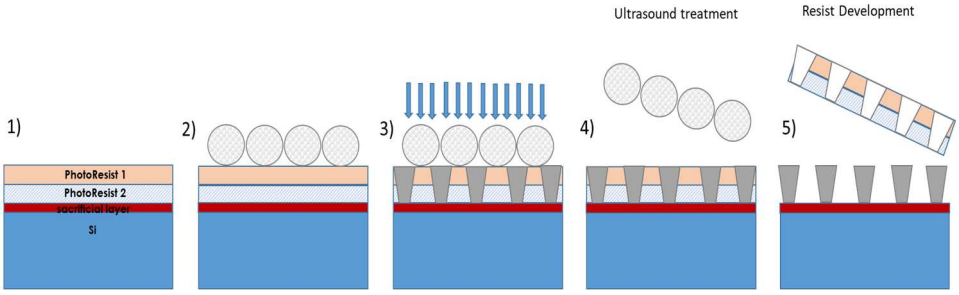

Figure 5.16. Schematic illustration of the NSL process based on PS monolayers used as lenses and lift-off strategies: 1) spin-coating of photoresists on a substrate, 2) formation of a monolayer of PS spheres on top of the photoresists by scooping transfer technique, 3) UV light exposure of the photoresists covered by the monolayer of HCP microspheres 4) spheres removal by sonication, 5) development of the photoresists.

Table 5.2. Experimental conditions used for the resists preparation (spinning and baking).

Resist name	Spinning speed (rpm)	Time of spinning (s)	Baking temperature (°C)	Baking time (min)
LOR B (7B)	4000	45	170	5
LOR A (1A)	1500	45	150	5
S1811	4000	60	115	1

Figure 5.17a shows the SEM image of an array of sub-micron holes formed inside the LOR A (1A)/S1811 photoresists. An ordered array of nanoholes with $d \sim 440$ nm was obtained with a lattice periodicity of ~ 1 μm, which is almost identical to the diameter of the spheres. Figures 5.17b, c show the cross-sectional images of the holes' pattern formed in the dual LOR A

(1A)/S1811 photoresist, which present an undercut profile that should to prevent the resist sidewalls from being coated, thus making easier the subsequent lift-off process.

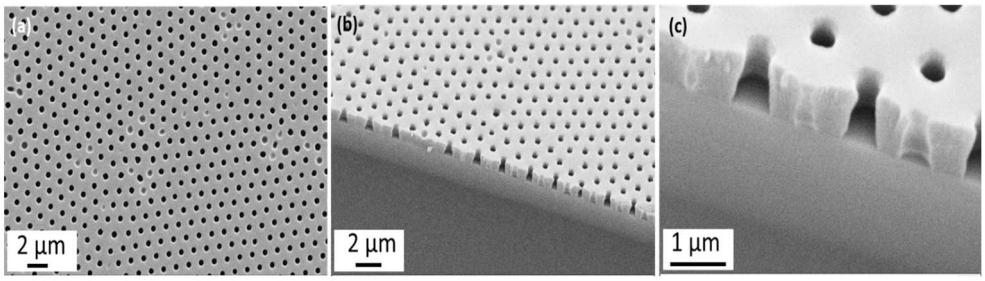

Figure 5.17. SEM images of (a) a two-dimensional hcp nanoholes array (440 nm hole diameter) formed inside S1811 photoresist after removing the spheres by ultrasound and developing the photoresist, (b) a cross section of the nanopattern showing the undercut obtained in the dual resists and (c) enlarged cross section of nanopatterns.

Concluding Remarks

The main goal of this thesis was to design, prepare and systematically investigate the magnetic, morphological and magneto-resistive properties of thin film stacks based on SAFs with perpendicular magnetic anisotropy for flexible spintronics and biomedical applications. Particularly, we focused on Co/Pd- and Co/Ni-based systems due to their large PMA, the high tunability of their magnetic properties via the modulation of the individual layers' thicknesses and the number of bilayers as well as the possibility to virtually obtain such structures on any substrates.

To further contribute to the domain of flexible spintronics, PMA [Co/Pd]-based GMR spin valves consisting of a fully compensated $[Co/Pd]_N/Ru/[Co/Pd]_N$ synthetic antiferromagnet (SAF) reference layer and a $[Co/Pd]_N$ free layer were prepared and obtained on flexible substrates using different approaches, including the direct deposition on different flexible substrates as well as dry and wet etching transfer-and-bonding strategies. Flexible PMA [Co/Ni]-based GMR spin valves, consisting of a fully compensated $[Co/Ni]_N/Ru/[Co/Ni]_N$ synthetic antiferromagnet (SAF) reference electrode and a $[Co/Ni]_N$ free layer were also prepared using the best developed strategy. Besides endowing the family of flexible electronics with PMA magneto-resistive heterostructures, the investigated systems are perfect candidates to test and demonstrate the potential of the proposed strategies, that might be easily extended to other functional multilayer materials, due to the complexity of the structure whose properties are strongly affected by the quality of the interfaces.

Co/Pd-based SAF thin film stacks were deposited and optimized by investigating the effect of number of bilayers, Co and Ru layer thickness, and the optimized SAF stack was then coupled to a $[Co/Pd]_N$ free layer across a Cu spacer to obtain a GMR spin valve. Large-area PMA flexible GMR spin valves with the structure

Ta/Pd/[Pd/Co]$_4$/Ru/[Co/Pd]$_3$/Co/Cu/[Co/Pd]$_2$/Pd, were prepared by employing different strategies, and the effect of the Cu spacer thickness on the magnetic, magnetoresistance and morphological properties was studied. Reference samples were also prepared by the direct deposition of the GMR SVs on SiO_2/Si (100) substrates to be compared with the flexible samples. By direct deposition on flexible Teonex® tapes and MICA substrates, high quality PMA-GMR SVs were obtained with a GMR ratio up to ~4% on mica and ~3.5 % on Teonex® tapes, which are comparable to the GMR ratio of the reference samples (~4.5%). However, in the case of MICA substrates, the shape of the MR curves was affected by the micrometres size terraces and cleavage steps that formed during the cleavage process, thus imposing the necessity to improve the cleavage process with the aim to obtain a flat surface over large area. Wet etching transfer-and-bonding strategies exploiting the use of PMMA sacrificial layers and KBr sacrificial substrates were also tested. High quality PMA-GMR SVs were obtained on PMMA/ SiO_2/Si with a GMR ratio of ~2%. After performing the lift-off process, a highly-flexible GMR spin valve on Kapton tapes with PMA was obtained. The magnetic properties were preserved; however, the MR measurements were suppressed due to the formation of cracks. A possible solution could be through the use of adhesion promoters based on silane molecules that are able to react chemically at both ends, with the sample' surface on one side and the polymer on the other side, thus creating a chemical bridge at the interface, which can help the adhesion and facilitate the transfer of the film stacks without creating cracks. When deposited on KBr substrates, the magnetic properties of the GMR SVs significantly deteriorated due to the formation of fractures brittles on the substrate that caused inhomogeneity and interfacial defects in the film stacks. Nevertheless, the transferring process was successfully accomplished. Using water soluble salt underlayers deposited prior to the growth of the GMR-SV thin film stack may be a solution to overcome the above mentioned issues. Finally, a dry etching transfer-and-bonding strategy exploiting the low

adhesion between Au on SiO_2/Si (100) substrates was developed and investigated. This strategy was capable of ensuring large-area flexible GMR SVs with sizeable GMR ratio of ~1.5 % and preserved magnetic properties when transferred on commercial adhesive tapes by mechanical peel-off. The GMR ratio could be further improved by reducing the Au surface roughness through a fine optimization of the deposition conditions. The results also prove the effectiveness of the proposed Au-mediated transfer and bonding approach, which can be easily extended to the grown of other functional and flexible multilayer materials engineered at the nanoscale, including those whose fabrication process requires high temperature treatments that impedes the direct deposition on flexible polymeric tapes. Moreover, the magneto-electric robustness of these flexible structures was demonstrated by performing magneto-resistance measurements versus bending where the moderate change in the GMR ratio is mainly ascribed to the geometrical configuration with respect to the magnetic field rather than to a change of the electric behaviour; thus paving the way for their integration on curved surfaces and the development of novel flexible devices requiring perpendicular magnetic anisotropy. Moreover, further work will be done in future to fabricate flexible magnetoresistive sensors as our PMA flexible systems can serve as switching sensors for a wide number of applications (e.g. wearable electronics) without the need of additional conditioning electronics as in the case of magneto-resistive devices with in-plane magnetic anisotropy.

The second part of this thesis was focused on studying Co/Ni-based systems. $[Co/Ni]_N/Ru/[Co/Ni]_N$ SAF thin film stacks were prepared on SiO_2/Si (100) substrates and on Teonex® tapes and the effects of the number of bilayers, the Ni layer thickness and the buffer layer on the magnetic properties were investigated. We observed that setting t_{Ni} to 0.7 nm and the number of bilayers to 6 allows maximizing the magnetic anisotropy, which is useful to achieve high thermal stability especially for the fabrication of nano-patterned devices, while keeping a wide antiferromagnetic coupled region,

which is necessary to guarantee well defined three-steps loops especially when the single layers' coercivity increases in multi-SAF stacks as a result of using buffer layers. The optimized SAF thin film stack was coupled to a $[Co/Ni]_N$ free layer through a 3 nm Cu spacer to obtain GMR-SVs with perpendicular magnetic anisotropy on rigid SiO_2/Si (100) substrates, and the effect of different buffer and capping layers was also investigated. The magnetic and magnetoresistance measurements revealed the characteristics of a GMR spin valve with a SAF reference layer. When a Ta/Pd buffer layer was used, a maximum GMR ratio of ~4.7 % was obtained which reduced to ~2.4 % for a Cu buffer layer which could be attributed to a lager interface roughness driven by a large surface roughness of the Cu buffer-layer. As for the capping layer effect (Pd and Cu/Ta layers), it was revealed from the magnetic and the corresponding magneto-resistive curves that both the capping layers contribute to the stabilization of the PMA in the free layer. Indeed, the use of a Pd layer might be capable of inducing a strong interfacial anisotropy that serves to rotate and stabilize the magnetization of the Co layer out-of-plane; whereas, the formation of a CuO_x/TaO_x capping layer as a consequence of the natural oxidation of Cu/Ta might be responsible for the stabilization of the PMA in the free layer, through the hybridization of the Co and O orbitals when a Cu/Ta was used. Concerning the GMR ratio, it decreased from ~4.5 % (Cu/Ta capping layer) to 3 % for Pd capping layer due to the larger spin-orbit scattering induced by the non-magnetic Pd layer. The GMR SV stacks were also deposited on flexible Teonex® tapes by using the direct deposition approach. When deposited on flexible substrates, the main magnetic and magnetoresistance characteristics of the GMR SVs were maintained. The major differences with respect to the reference samples are the unsharp switching of the magnetization, which was also reflects in the shape of the MR curves that became rounded rather than straight. Moreover, the free-layer coercivity slightly reduces resulting in a narrowing of the plateau in the high-resistance region of the MR curves. All these differences could be related to a higher

surface roughness of Teonex® (0.7 nm) with respect to SiO_2/Si (100) substrates (~0.3 nm).

The last part of this thesis was concerned with the preparation and study of Co/Pd-SAF based micro/nanodisks with perpendicular magnetic anisotropy for biomedical applications using both top-down and bottom-up EBL approaches. In the top-down approach, PMA thin film stacks consisting of multiple repeats M (from 1 to 8) of the optimized $[Co/Pd]_N/Ru/[Co/Pd]_N$ SAF units were studied as potential materials to fabricate free-standing microdisks through the use of a sacrificial resist layer. These layers were used as building-blocks to prepare $\{[Co/Pd]_4/Ru/[Co/Pd]_4\}_M$ multi-stacks on an Au/resist underlayer. The SAF film samples were found to fulfil all the key criteria required for biomedical applications, i.e., zero remanence, zero field susceptibility at small fields, and a sharp magnetization reversal to saturation. Moreover, the results indicate that the magnetic moment at saturation can be modulated without changing the hysteresis main features, by varying the number of repetitions up to M = 6. Above this value, the interface quality, which gradually reduces with increasing repetition number, was significantly affected, leading to a substantial deterioration of the magnetic properties. The main output of this work is the significant versatility and adaptability of this complex system to be grown on different substrates and, in particular, on an Au/resist underlayer that makes it a suitable material for the preparation of free-standing synthetic antiferromagnetic micro-/nanodisks for biomedical applications. This was demonstrated by preparing SAF microdisks by means of top-down and bottom-up EBL combined with lift-off and/or ion etching processes. The prepared microdisks revealed only a slight deterioration of the magnetic properties. For practical applications and massive production of optimized multi-SAF nanodisks, a strategy combining lift-off and/or ion etching processes with cost and time-effective lithographic techniques was set-up. In particular, we investigated both bottom-up and top-down nanosphere lithographic (NSL) approaches based on the use of self-assembled

monolayer arrays of Polystyrene (PS) microspheres either as mask layers for top-down lithographic approaches combining ion etching processes or as UV optical lenses to prepare pre-patterned arrays of sub-micron holes for bottom-up approaches combining lift-off processes. Self-assembled PS monolayers were obtained by using the best strategy, the "scooping transfer" technique. As for the top-down approach, Ar ion milling was used to selectively reduce the size of the spheres and obtain a mask for further etching processes. While for the bottom-up approaches, ordered arrays of nanoholes with $d \sim 440$ nm were obtained with a lattice periodicity of ~ 1 μm. Indeed, nanopatterned holes obtained by photolithography represent an alternative to the micro/nanoholes patterns prepared by the more expensive EBL technique. Moreover, besides the capability of NSL in yielding large areas of micro/nanoholes' patterns, it is also possible to control both the hole diameter by varying the exposure time and the hole-to-hole distance (lattice period) by using different spherical diameters. Thus, this work will be completed in the future by optimizing the experimental setup and the conditions with the aim of obtaining SAF micro/nanodisks that are suitable for biomedical applications.

References

1. Chappert, C., Fert, A. & Van Dau, F. N. The emergence of spin electronics in data storage. *Nat. Mater.* (2007) doi:10.1038/nmat2024.
2. Bandiera, S. *et al.* Comparison of synthetic antiferromagnets and hard ferromagnets as reference layer in magnetic tunnel junctions with perpendicular magnetic anisotropy. *IEEE Magn. Lett.* **1**, 1–4 (2010).
3. Zheng, Y. & Zhu, J. G. Micromagnetics of spin valve mram with synthetic antiferromagnet. in (2005). doi:10.1109/intmag.1998.742149.
4. Vemulkar, T., Mansell, R. & Cowburn, R. P. Toward Flexible Spintronics : Perpendicularly Magnetized Synthetic Antiferromagnetic Thin Films and Nanowires on Polyimide Substrates. 4704–4711 (2016) doi:10.1002/adfm.201505138.
5. Grünberg, P. *et al.* Layered magnetic structures: Evidence for antiferromagnetic coupling of Fe layers across Cr interlayers. *J. Appl. Phys.* **61**, 3750–3752 (1987).
6. Parkin, S. S. P. Systematic variation of the strength and oscillation period of indirect magnetic exchange coupling through the 3d, 4d, and 5d transition metals. *Phys. Rev. Lett.* **67**, 3598–3601 (1991).
7. Parkin, S. S. P., Bhadra, R. & Roche, K. P. Oscillatory magnetic exchange coupling through thin copper layers. *Phys. Rev. Lett.* (1991) doi:10.1103/PhysRevLett.66.2152.
8. Parkin, S. S. P., More, N. & Roche, K. P. Oscillations in exchange coupling and magnetoresistance in metallic superlattice structures: Co/Ru, Co/Cr, and Fe/Cr. *Phys. Rev. Lett.* **64**, 2304–2307 (1990).
9. Roth, L. M., Zeiger, H. J. & Kaplan, T. A. Generalization of the Ruderman-Kittel-Kasuya-Yosida interaction for nonspherical fermi surfaces. *Phys. Rev.* (1966) doi:10.1103/PhysRev.149.519.
10. Bruno, P. & Chappert, C. Oscillatory coupling between ferromagnetic layers separated by a nonmagnetic metal spacer. *Phys. Rev. Lett.*

(1991) doi:10.1103/PhysRevLett.67.1602.
11. Edwards, D. M., Mathon, J., Muniz, R. B. & Phan, M. S. Oscillations of the exchange in magnetic multilayers as an analog of de Haasvan Alphen effect. *Phys. Rev. Lett.* **67**, 493–496 (1991).
12. Cebollada, A. *et al.* Antiferromagnetic ordering in Co-Cu single-crystal superlattices. *Phys. Rev. B* (1989) doi:10.1103/PhysRevB.39.9726.
13. Thiyagarajah, N. & Bae, S. Effects of engineered Cu spacer on the interlayer coupling and giant magnetoresistance behavior in Pd/ [Pd/Co] 2 /Cu/ [Co/Pd] 4 pseudo-spin-valves with perpendicular anisotropy. *J. Appl. Phys.* **104**, (2008).
14. Yakushiji, K., Fukushima, A., Kubota, H., Konoto, M. & Yuasa, S. Ultralow-voltage spin-transfer switching in perpendicularly magnetized magnetic tunnel junctions with synthetic antiferromagnetic reference layer. *Appl. Phys. Express* **6**, 113006 (4pp) (2013).
15. Yakushiji, K., Kubota, H., Fukushima, A. & Yuasa, S. Perpendicular magnetic tunnel junctions with strong antiferromagnetic interlayer exchange coupling at first oscillation peak. *Appl. Phys. Express* **8**, 083003 (4pp) (2015).
16. Arora, M. *et al.* Magnetic properties of Co / Ni multilayer structures for use in STT-RAM. *J. Phys. D Appl. Phys.* **50**, 505003 (11pp) (2017).
17. Arora, M. *et al.* Spin torque switching in nanopillars with antiferromagnetic reference layer. *IEEE Magn. Lett.* **8**, (2017).
18. Chang, Y., Garcia-vazquez, V., Chang, Y. & Wu, T. Perpendicular magnetic tunnel junctions with synthetic antiferromagnetic pinned layers based on [Co/Pd] multilayers. *J. Appl. Phys.* **113**, 17B909 (2016).
19. Devolder, T. *et al.* Annealing stability of magnetic tunnel junctions based on dual MgO free layers and [Co/Ni] based thin synthetic antiferromagnet fixed system. *J. Appl. Phys.* **121**, 113904 (2017).
20. Li, Z., Zhang, Z., Zhao, H., Ma, B. & Jin, Q. Y. High giant magnetoresistance and thermal annealing effects in perpendicular magnetic [Co/Ni]N-based spin valves. *J. Appl. Phys.* **106**, 013907 (2015).
21. Lim, S. Ter, Tran, M., Chenchen, J. W., Ying, J. F. & Han, G. Effect of

different seed layers with varying Co and Pt thicknesses on the magnetic properties of Co/Pt multilayers. *J. Appl. Phys.* **117**, 17A731 (2015).
22. Engel, B. N., England, C. D., Leeuwen, R. A. Van, Wiedmann, M. H. & Falco, C. M. Interface Magnetic Anisotropy in Epitaxial Superlattices. *Phys. Rev. Lett.* **67**, 1910–1913 (1991).
23. Baibich, M. N. *et al.* Giant magnetoresistance of (001)Fe/(001)Cr magnetic superlattices. *Phys. Rev. Lett.* **61**, 2472–2475 (1988).
24. Barna, J., Fuss, A., Camley, R. E., Gr̈nberg, P. & Zinn, W. Novel magnetoresistance effect in layered magnetic structures: Theory and experiment. *Phys. Rev. B* **42**, 8110–8120 (1990).
25. Ohno, H. Making nonmagnetic semiconductors ferromagnetic. *Science* (1998) doi:10.1126/science.281.5379.951.
26. Wolf, S. A. *et al.* Spintronics: A spin-based electronics vision for the future. *Science* (2001) doi:10.1126/science.1065389.
27. Fert, A. *et al.* Review of recent results on spin polarized tunneling and magnetic switching by spin injection. *Mater. Sci. Eng. B Solid-State Mater. Adv. Technol.* (2001) doi:10.1016/S0921-5107(01)00548-7.
28. Barthélémy, A. *et al.* Magnetoresistance and spin electronics. *J. Magn. Magn. Mater.* (2002) doi:10.1016/S0304-8853(01)01193-3.
29. Dieny, B., Goldfarb, R. B. & Lee, K. J. *Introduction to magnetic random-access memory*. *Introduction to Magnetic Random-Access Memory* (2016). doi:10.1002/9781119079415.
30. Binasch, G., Grünberg, P., Saurenbach, F. & Zinn, W. Enhanced magnetoresistance in layered magnetic structures with antiferromagnetic interlayer exchange. *Phys. Rev. B* **39**, 4828–4830 (1989).
31. Ikeda, S. *et al.* Tunnel magnetoresistance of 604% at 300 K by suppression of Ta diffusion in CoFeBMgOCoFeB pseudo-spin-valves annealed at high temperature. *Appl. Phys. Lett.* (2008) doi:10.1063/1.2976435.
32. Bass, J. & Pratt, W. P. Current-perpendicular (CPP) magnetoresistance in magnetic metallic multilayers. *J. Magn. Magn. Mater.* (1999) doi:10.1016/S0304-8853(99)00316-9.
33. Dieny, B. *et al.* Magnetotransport properties of magnetically soft

spin-valve structures (invited). *J. Appl. Phys.* **69**, 4774–4779 (1991).
34. J.C., S. Current-driven excitation of magnetic multilayers. *J. Magn. Magn. Mater.* **159**, L1–L7 (1996).
35. Berger, L. Emission of spin waves by a magnetic multilayer traversed by a current. *Phys. Rev. B - Condens. Matter Mater. Phys.* (1996) doi:10.1103/PhysRevB.54.9353.
36. Garello, K. *et al.* Symmetry and magnitude of spin-orbit torques in ferromagnetic heterostructures. *Nat. Nanotechnol.* (2013) doi:10.1038/nnano.2013.145.
37. Miron, I. M. *et al.* Current-driven spin torque induced by the Rashba effect in a ferromagnetic metal layer. *Nat. Mater.* (2010) doi:10.1038/nmat2613.
38. Pohm, V. Threshold properties of 1, 2 and 4 mm multilayer magneto-resistive cells. *IEEE Trans. Magn.* **23**, 2575–2577 (1987).
39. Pohm, A. V., Huang, J. S. T., Daughton, J. M., Krahn, D. R. & Mehra, V. The design of a one megabit non-volatile m-r memory chip using 1.5 × 5 μm cells. *IEEE Trans. Magn.* (1988) doi:10.1109/20.92353.
40. Hu, J. M., Li, Z., Chen, L. Q. & Nan, C. W. High-density magnetoresistive random access memory operating at ultralow voltage at room temperature. *Nat. Commun.* (2011) doi:10.1038/ncomms1564.
41. Zheng, C. *et al.* Magnetoresistive Sensor Development Roadmap (Non-Recording Applications). *IEEE Trans. Magn.* (2019) doi:10.1109/TMAG.2019.2896036.
42. Freitas, P. P., Ferreira, R. & Cardoso, S. Spintronic Sensors. *Proc. IEEE* (2016) doi:10.1109/JPROC.2016.2578303.
43. Silva, A. V. *et al.* Linearization strategies for high sensitivity magnetoresistive sensors. *EPJ Appl. Phys.* (2015) doi:10.1051/epjap/2015150214.
44. Smith, C. H. & Schneider, R. W. Magnetic field sensing utilizing GMR materials. *Sens. Rev.* (1998) doi:10.1108/02602289810240592.
45. Khvalkovskiy, A. V. *et al.* Basic principles of STT-MRAM cell operation in memory arrays. *J. Phys. D. Appl. Phys.* (2013) doi:10.1088/0022-3727/46/7/074001.
46. Giebeler, C. *et al.* Robust GMR sensors for angle detection and rotation speed sensing. *Sensors Actuators, A Phys.* (2001)

doi:10.1016/S0924-4247(01)00510-6.
47. Wang, Y. H. *et al.* Impact of stray field on the switching properties of perpendicular MTJ for scaled MRAM. in *Technical Digest - International Electron Devices Meeting, IEDM* (2012). doi:10.1109/IEDM.2012.6479127.
48. Jiancheng, H. *et al.* Effect of the stray field profile on the switching characteristics of the free layer in a perpendicular magnetic tunnel junction. *J. Appl. Phys.* (2015) doi:10.1063/1.4916037.
49. Kent, A. D. & Worledge, D. C. A new spin on magnetic memories. *Nat. Nanotechnol.* **10**, 187–191 (2015).
50. Parkin, S. S. P. Origin of enhanced magnetoresistance of magnetic multilayers: Spin-dependent scattering from magnetic interface states. *Phys. Rev. Lett.* (1993) doi:10.1103/PhysRevLett.71.1641.
51. Feng, Z., Yan, H. & Liu, Z. Electric-Field Control of Magnetic Order : From FeRh to Topological Antiferromagnetic Spintronics. *Adv. Electron. Mater.* **5**, 1800466 (1–14) (2019).
52. Back, C. *et al.* The 2020 skyrmionics roadmap. *J. Phys. D. Appl. Phys.* **53**, 363001 (2020).
53. Chen, R. *et al.* Realization of Isolated and High-Density Skyrmions at Room Temperature in Uncompensated Synthetic Antiferromagnets. *Nano Lett.* **20**, 3299–3305 (2020).
54. Dohi, T., Duttagupta, S., Fukami, S. & Ohno, H. Formation and current-induced motion of synthetic antiferromagnetic skyrmion bubbles. *Nat. Commun.* **1'**, 5153 (2019).
55. Legrand, W. *et al.* Room-temperature stabilization of antiferromagnetic skyrmions in synthetic antiferromagnets. *Nat. Mater.* **19**, 34–42 (2020).
56. Zhou, S., Zheng, C., Chen, X. & Liu, Y. Skyrmion-based spin-torque nano-oscillator in synthetic antiferromagnetic nanodisks. *J. Appl. Phys.* **128**, 033907 (2020).
57. Yu, Z. *et al.* Voltage-controlled skyrmion-based nanodevices for neuromorphic computing using a synthetic antiferromagnet. *Nanoscale Adv.* **2**, 1309–1317 (2020).
58. Yang, Q. *et al.* Ionic liquid gating control of RKKY interaction in FeCoB/Ru/FeCoB and (Pt/Co)2/Ru/(Co/Pt)2 multilayers. *Nat. Commun.* **9**, 991 (2018).

59. Yang, Q. *et al.* Ionic Gel Modulation of RKKY Interactions in Synthetic Anti-Ferromagnetic Nanostructures for Low Power Wearable Spintronic Devices. *Adv. Mater.* **30**, 1800449 (1–8) (2018).
60. Wang, X. *et al.* E-field Control of the RKKY Interaction in FeCoB/Ru/FeCoB/PMN-PT (011) Multiferroic Heterostructures. *Adv. Mater.* **30**, 1803612 (1–8) (2018).
61. Engel, B. N. *et al.* A 4-Mb toggle MRAM based on a novel bit and switching method. *IEEE Trans. Magn.* **41**, 132–136 (2005).
62. Hung, C. C. *et al.* Adjacent-reference and self-reference sensing scheme with novel orthogonal wiggle MRAM cell. *Tech. Dig. - Int. Electron Devices Meet. IEDM* 10–13 (2006) doi:10.1109/IEDM.2006.346851.
63. Jose, S. *et al.* (12) United States Patent. **2**, (2016).
64. Hu, J. *et al.* Flexible integrated photonics: where materials, mechanics and optics meet [Invited]. *Opt. Mater. Express* (2013) doi:10.1364/ome.3.001313.
65. Sun, Q. *et al.* Functional biomaterials towards flexible electronics and sensors. *Biosensors and Bioelectronics* (2018) doi:10.1016/j.bios.2018.08.018.
66. Pan, L. *et al.* Metal-organic framework nanofilm for mechanically flexible information storage applications. *Adv. Funct. Mater.* (2015) doi:10.1002/adfm.201500449.
67. Makarov, D., Melzer, M., Karnaushenko, D. & Schmidt, O. G. Shapeable magnetoelectronics. *Appl. Phys. Rev.* **3**, (2016).
68. D.-H. Kim, J.-H. Ahn, W. M. Choi, H.-S. Kim, T.-H. K. & J. Song, Y. Y. Huang, Z. Liu, C. L. and J. A. R. Stretchable and Foldable Silicon Integrated Circuits. *Science (80-.).* **320**, (2008).
69. J. A. Rogers, T. S. and Y. H. Materials and Mechanics for Stretchable Electronics. *Science (80-.).* **327**, (2010).
70. H. Nishide and K. Oyaizu. Toward flexible batteries. *Science (80-.).* **319**, (2008).
71. N. Li, Z. Chen, W. Ren, F. L. and H.-M. C. Flexible graphene-based lithium ion batteries with ultrafast charge and discharge rates. *Acad. Sci. U. S. A.* **109**, (2012).
72. M. S. White, M. Kaltenbrunner, E. D. G., K. Gutnichenko, G. Kettlgruber, I. Graz, S. A., C. Ulbricht, D. A. M. Egbe, M. C. Miron, Z.

M., M. C. Scharber, T. Sekitani, T. Someya, S. B. and & N. S. Sariciftci. Ultrathin, highly flexible and stretchable PLEDs. *Nat. Photonics,* **7**, (2013).

73. S. S. P. Parkin, A. P. L. Flexible giant magnetoresistance sensors. **69**, (1996).
74. Y. Chen, Y. Mei, R. Kaltofen, J. I. Mönch, J. S. & J. Freudenberger, H.-J. K. and O. G. S. Towards Flexible Magnetoelectronics: Buffer-Enhanced and Mechanically Tunable GMR of Co/Cu Multilayers on Plastic Substrates. *Adv. Mater.* **20**, (2008).
75. M. Melzer, D. Makarov, A. Calvimontes, D. K. & S. Baunack, R. Kaltofen, Y. M. and O. G. S. Stretchable Magnetoelectronics. *Nano Lett.* **11**, (2011).
76. G. H. Gelinck, H. E. A. Huitema, E. van V., E. Cantatore, L. Schrijnemakers, J. B. P. H. van der P., T. C. T. Geuns, M. Beenhakkers, J. B. Giesbers, B.-H. H., E. J. Meijer, E. M. Benito, F. J. Touwslager, A. W. M. & B. J. E. van Rens and D. M. de Leeuw. Flexible active-matrix displays and shift registers based on solution-processed organic transistors. *Nat. Mater.* **3**, (2004).
77. 0 Y. Chen, J. Au, P. Kazlas, A. Ritenour, H. G. and M. M. Flexible active-matrix electronic ink display. *Nature* **423**, (2003).
78. M. Kaltenbrunner, T. Sekitani, J. Reeder, T. Y., K. Kuribara, T. Tokuhara, M. Drack, R. Schwödiauer, I. G. & S. Bauer-Gogonea, S. B. and T. S. An ultra-lightweight design for imperceptible plastic electronics. *Nature* **499**, (2013).
79. G. A. Salvatore, N. Münzenrieder, T. Kinkeldei, L. P. & C. Zysset, I. Strebel, L. B. and G. T. Wafer-scale design of lightweight and transparent electronics that wraps around hairs. *Nat. Commun.* **5**, (2014).
80. M. Kaltenbrunner, M. S. White, E. D. Głowacki, T. S. & T. Someya, N. S. S. and S. B. Ultrathin and lightweight organic solar cells with high flexibility. *Nat. Commun.* **3**, (2012).
81. F. Eder, H. Klauk, M. Halik, U. Zschieschang, G. S. and & C. Dehm. Organic electronics on paper. *Appl. Phys. Lett.* **84**, (2004).
82. Cai, L. & Wang, C. Carbon Nanotube Flexible and Stretchable Electronics. *Nanoscale Research Letters* (2015) doi:10.1186/s11671-015-1013-1.

83. Stewart R, Chiang A, Hermanns A, Vicentini F, Jacobsen J, Atherton J, Boiling E, C. F. & Drzaic P, P. S. Rugged low-cost display systems. *Proc SPIE – Int Soc Opt Eng* **4712**, (2002).
84. Bühler, J., Steiner, F. P. & Baltes, H. Silicon dioxide sacrificial layer etching in surface micromachining. *Journal of Micromechanics and Microengineering* (1997) doi:10.1088/0960-1317/7/1/001.
85. Linder, V., Gates, B. D., Ryan, D., Parviz, B. A. & Whitesides, G. M. Water-soluble sacrificial layers for surface micromachining. *Small* **1**, 730–736 (2005).
86. Hofmann, S., Ducati, C., Kleinsorge, B. & Robertson, J. Direct growth of aligned carbon nanotube field emitter arrays onto plastic substrates. *Appl. Phys. Lett.* (2003) doi:10.1063/1.1630167.
87. Choi, M. C., Kim, Y. & Ha, C. S. Polymers for flexible displays: From material selection to device applications. *Progress in Polymer Science (Oxford)* (2008) doi:10.1016/j.progpolymsci.2007.11.004.
88. Eder, F. *et al.* Organic electronics on paper. *Appl. Phys. Lett.* (2004) doi:10.1063/1.1690870.
89. Chu, Y. H. Van der Waals oxide heteroepitaxy. *npj Quantum Materials* (2017) doi:10.1038/s41535-017-0069-9.
90. Zheng, M., Sun, H. & Kwok, K. W. Mechanically controlled reversible photoluminescence response in all-inorganic flexible transparent ferroelectric/mica heterostructures. *NPG Asia Mater.* **11**, 0–7 (2019).
91. Fortier, S. M. & Giletti, B. J. Volume self-diffusion of oxygen in biotite, muscovite, and phlogopite micas. *Geochim. Cosmochim. Acta* (1991) doi:10.1016/0016-7037(91)90310-2.
92. Ma, C. H. *et al.* Van der Waals epitaxy of functional MoO2 film on mica for flexible electronics. *Appl. Phys. Lett.* (2016) doi:10.1063/1.4954172.
93. Saha, S. *et al.* Single heterojunction solar cells on exfoliated flexible ∼25 μm thick mono-crystalline silicon substrates. *Appl. Phys. Lett.* (2013) doi:10.1063/1.4803174.
94. Lee, Y., Li, H. & Fonash, S. J. High-performance poly-Si TFT on plastic substrates using a nano-structured separation layer approach. *IEEE Electron Device Lett.* **24**, 19–21 (2003).
95. Inoue, S., Utsunomiya, S., Saeki, T. & Shimoda, T. Surface-Free Technology by Laser Annealing (SUFTLA) and Its Application to Poly-

Si TFT-LCDs on Plastic Film With Integrated Drivers. **49**, 1353–1360 (2002).
96. Heczko, O., Thomas, M., Niemann, R., Schultz, L. & Fähler, S. Magnetically induced martensite transition in freestanding epitaxial Ni-Mn-Ga films. *Appl. Phys. Lett.* **94**, 1–4 (2009).
97. Tillier, J. *et al.* Fabrication and characterization of a Ni-Mn-Ga uniaxially textured freestanding film deposited by DC magnetron sputtering. *J. Alloys Compd.* **489**, 509–514 (2010).
98. Al., L. W. G. et. Structural and magnetic properties of Mn O " lms grown on MgO (0 0 1) substrates by plasma-assisted MBE. **213**, (2000).
99. Bodong Li, Mincho N.Kavaldzhiev, J. K. Flexible magnetoimpedance sensor. *J. Magn. Magn. Mater.* **378**, (2015).
100. Kumar, A. Methods and Materials for Smart Manufacturing: Additive Manufacturing, Internet of Things, Flexible Sensors and Soft Robotics. *Manuf. Lett.* (2018) doi:10.1016/j.mfglet.2017.12.014.
101. Yeo, W.-H., Webb, R. C., Lee, W., Jung, S. & Rogers, J. A. Bio-integrated electronics and sensor systems. in *Micro- and Nanotechnology Sensors, Systems, and Applications V* (2013). doi:10.1117/12.2016380.
102. Schwarz, M. *et al.* Single chip CMOS imagers and flexible microelectronic stimulators for a retina implant system. *Sensors Actuators, A Phys.* (2000) doi:10.1016/S0924-4247(00)00290-9.
103. Yan, F., Xue, G. & Wan, F. A flexible giant magnetoresistance sensor prepared completely by electrochemical synthesis. *J. Mater. Chem.* (2002) doi:10.1039/b206896f.
104. Amara, S. *et al.* High-Performance Flexible Magnetic Tunnel Junctions for Smart Miniaturized Instruments. *Adv. Eng. Mater.* (2018) doi:10.1002/adem.201800471.
105. Chen, J. Y., Lau, Y. C., Coey, J. M. D., Li, M. & Wang, J. P. High performance MgO-barrier magnetic tunnel junctions for flexible and wearable spintronic applications. *Sci. Rep.* **7**, 1–7 (2017).
106. Hawsawi, M. *et al.* Flexible Magnetoresistive Sensors for Guiding Cardiac Catheters. in *MeMeA 2018 - 2018 IEEE International Symposium on Medical Measurements and Applications, Proceedings* (2018). doi:10.1109/MeMeA.2018.8438796.

107. Mashraei, Y., Swanepoel, L. & Kosel, J. A Triaxial Flexible Magnetic Tunnel Junction Sensor for Catheter Tracking. in *Proceedings of IEEE Sensors* (2019). doi:10.1109/SENSORS43011.2019.8956888.
108. Wang, Z., Shaygan, M., Otto, M., Schall, D. & Neumaier, D. Flexible Hall sensors based on graphene. *Nanoscale* (2016) doi:10.1039/c5nr08729e.
109. Parkin, S. S. P. Flexible giant magnetoresistance sensors. *Appl. Phys. Lett.* **69**, 3092–3094 (1996).
110. Wu, M. & Huang, S. Magnetic nanoparticles in cancer diagnosis, drug delivery and treatment (Review). *Mol. Clin. Oncol.* **7**, 738–746 (2017).
111. Mir, M. *et al.* Nanotechnology: from In Vivo Imaging System to Controlled Drug Delivery. *Nanoscale Res. Lett.* **12**, 500 (16pp) (2017).
112. Kafrouni, L. & Savadogo, O. Recent progress on magnetic nanoparticles for magnetic hyperthermia. *Prog. Biomater.* **5**, 147–160 (2016).
113. Huang, J., Zhong, X., Wang, L., Yang, L. & Mao, H. Improving the magnetic resonance imaging contrast and detection methods with engineered magnetic nanoparticles. *Theranostics* **2**, 86–102 (2012).
114. Akbarzadeh, A., Samiei, M. & Davaran, S. Magnetic nanoparticles: preparation, physical properties, and applications in biomedicine. *Nanoscale Res. Lett.* **7**, 144 (13pp) (2012).
115. Kumar, C. S. S. R. & Mohammad, F. Magnetic nanomaterials for hyperthermia-based therapy and controlled drug delivery. *Adv. Drug Deliv. Rev.* **63**, 789–808 (2011).
116. Krishnan, K. M. Biomedical Nanomagnetics: A Spin Through Possibilities in Imaging, Diagnostics, and Therapy. *Magn. IEEE Trans.* **46**, 2523–2558 (2010).
117. Pankhurst, Q. A., Thanh, N. K. T., Jones, S. K. & Dobson, J. Progress in applications of magnetic nanoparticles in biomedicine. *J. Phys. D. Appl. Phys.* **42**, 224001 (15pp) (2009).
118. Bellusci, M. *et al.* Magnetic Metal − Organic Framework Composite by Fast and Facile Mechanochemical Process. *Inorg. Chem.* **57**, 1806–18014 (2018).
119. Scano, A. *et al.* New opportunities in the preparation of nanocomposites from biomedical applications: Revised

mechanosynthesis of magnetite-silica nanocomposites. *Mater. Res. Express* **4**, 025004 (11pp) (2017).
120. Zhang, L., Zhao, Y. & Wang, X. Nanoparticle-Mediated Mechanical Destruction of Cell Membranes: A Coarse-Grained Molecular Dynamics Study. *ACS Appl. Mater. Interfaces* **9**, 26665–26673 (2017).
121. Mansell, R. *et al.* Magnetic particles with perpendicular anisotropy for mechanical cancer cell destruction. *Sci. Rep.* **7**, 4257 (7pp) (2017).
122. Cheng, Y. *et al.* Rotating magnetic field induced oscillation of magnetic particles for in vivo mechanical destruction of malignant glioma. *J. Control. Release* **223**, 75–84 (2016).
123. Wo, F. *et al.* A multimodal system with synergistic effects of magneto-mechanical, photothermal, photodynamic and chemo therapies of cancer in graphene-quantum dot-coated hollow magnetic nanospheres. *Theranostics* **6**, 485–500 (2016).
124. Martínez-Banderas, A. I. *et al.* Functionalized magnetic nanowires for chemical and magneto-mechanical induction of cancer cell death. *Sci. Rep.* **6**, 35786 (11pp) (2016).
125. Golovin, Y. I. *et al.* Towards nanomedicines of the future: Remote magneto-mechanical actuation of nanomedicines by alternating magnetic fields. *J. Control. Release* **219**, 43–60 (2015).
126. Leulmi, S. *et al.* Triggering the apoptosis of targeted human renal cancer cells by the vibration of anisotropic magnetic particles attached to the cell membrane. *Nanoscale* **7**, 15904–15914 (2015).
127. Zhang, E. *et al.* Dynamic magnetic fields remote-control apoptosis via nanoparticle rotation. *ACS Nano* **8**, 3192–3201 (2014).
128. Domenech, M., Marrero-Berrios, I., Torres-Lugo, M. & Rinaldi, C. Lysosomal membrane permeabilization by targeted magnetic nanoparticles in alternating magnetic fields. *ACS Nano* **7**, 5091–5101 (2013).
129. Scialabba, C. *et al.* Folate targeted coated SPIONs as efficient tool for MRI. *Nano Res.* **10**, 3212–3227 (2017).
130. Peddis, D. *et al.* Studying nanoparticles' 3D shape by aspect maps: Determination of the morphology of bacterial magnetic nanoparticles. *Faraday Discuss.* **191**, 177–188 (2016).
131. Peddis, D. *et al.* Beyond the Effect of Particle Size : Influence of CoFe2O4 Nanoparticle Arrangements on Magnetic Properties. *Chem.*

Mater. **25**, 2005–2013 (2013).
132. Néel, L. Theorie du trainage magnetique des feroomagnetiques en grain fins avec applications aux terres cuties. *Ann. Gèophysique* **5**, 99–136 (1949).
133. Laureti, S. *et al.* Magnetic interactions in silica coated nanoporous assemblies of CoFe2O4 nanoparticles with cubic magnetic anisotropy. *Nanotechnology* **21**, 315701 (6pp) (2010).
134. Qi, Y. *et al.* Carboxylic silane-exchanged manganese ferrite nanoclusters with high relaxivity for magnetic resonance imaging. *J. Mater. Chem. B* **1**, 1846–1851 (2013).
135. Paquet, C. *et al.* Clusters of superparamagnetic iron oxide nanoparticles encapsulated in a hydrogel: A particle architecture generating a synergistic enhancement of the T2 relaxation. *ACS Nano* **5**, 3104–3112 (2011).
136. Gibbs, J. G. *et al.* Nanohelices by shadow growth. *Nanoscale* **6**, 9457–9466 (2014).
137. Goiriena-Goikoetxea, M., García-Arribas, A., Rouco, M., Svalov, A. & Barandiaran, J. M. High-yield fabrication of 60nm Permalloy nanodiscs in well-defined magnetic vortex state for biomedical applications. *Nanotechnology* **27**, 175302 (10pp) (2016).
138. Leulmi, S. *et al.* Comparison of dispersion and actuation properties of vortex and synthetic antiferromagnetic particles for biotechnological applications. *Appl. Phys. Lett.* **103**, 132412 (5pp) (2013).
139. Tiberto, P. *et al.* Ni80Fe20 nanodisks by nanosphere lithography for biomedical applications. *J. Appl. Phys.* **117**, 17B304 (4pp) (2015).
140. Kim, D. H. *et al.* Biofunctionalized magnetic-vortex microdiscs for targeted cancer-cell destruction. *Nat. Mater.* **9**, 165–171 (2010).
141. Hu, W. *et al.* High-moment antiferromagnetic nanoparticles with tunable magnetic properties. *Adv. Mater.* **20**, 1479–1483 (2008).
142. Hu, W. *et al.* Synthetic antiferromagnetic nanoparticles with tunable susceptibilities. *J. Appl. Phys.* **105**, 07B508 (3pp) (2009).
143. Joisten, H. *et al.* Self-polarization phenomenon and control of dispersion of synthetic antiferromagnetic nanoparticles for biological applications. *Appl. Phys. Lett.* **97**, 253112 (3pp) (2010).
144. Zhang, M. *et al.* Functionalization of high-moment magnetic

nanodisks for cell manipulation and separation. *Nano Res.* **6**, 745–751 (2013).
145. Van Roosbroeck, R. *et al.* Synthetic antiferromagnetic nanoparticles as potential contrast agents in MRI. *ACS Nano* **8**, 2269–2278 (2014).
146. Muroski, M. E. *et al.* Controlled payload release by magnetic field triggered neural stem cell destruction for malignant glioma treatment. *PLoS One* **11**, 4–15 (2016).
147. Vemulkar, T., Mansell, R., Petit, D. C. M. C., Cowburn, R. P. & Lesniak, M. S. Highly tunable perpendicularly magnetized synthetic antiferromagnets for biotechnology applications. *Appl. Phys. Lett.* **107**, 012403 (4pp) (2015).
148. Vemulkar, T., Mansell, R., Petit, D. C. M. C., Cowburn, R. P. & Lesniak, M. S. The effect of underlayers on the reversal of perpendicularly magnetized multilayer thin films for magnetic micro- and nanoparticles. *J. Appl. Phys.* **121**, 043908 (6pp) (2017).
149. Vemulkar, T., Welbourne, E. N., Mansell, R., Petit, D. C. M. C. & Cowburn, R. P. The mechanical response in a fluid of synthetic antiferromagnetic and ferrimagnetic microdiscs with perpendicular magnetic anisotropy. *Appl. Phys. Lett.* **110**, 042402 (4pp) (2017).
150. Vitol, E. A. *et al.* Optical transmission modulation by disk-shaped ferromagnetic particles. *J. Appl. Phys.* **111**, 07A945 (3pp) (2012).
151. Ball, D. K. *et al.* Out-of-plane magnetized cone-shaped magnetic nanoshells. *J. Phys. D. Appl. Phys.* **50**, 115004 (7pp) (2017).
152. Ball, D. K. *et al.* Magnetic properties of granular CoCrPt : SiO 2 thin films deposited on GaSb nanocones. *Nanotechnology* **25**, 085703 (6pp) (2014).
153. Bobek, B. T. *et al.* Self-Organized Hexagonal Patterns of Independent Magnetic Nanodots. *Adv. Mater.* **19**, 4375–4380 (2007).
154. Castro, M., Cuerno, R. & Va, L. Self-Organized Ordering of Nanostructures Produced by Ion-Beam Sputtering. *Phys. Rev. Lett.* **94**, 016102–4 (2005).
155. Zhang, W. & Krishnan, K. M. Direct release of synthetic antiferromagnetic nanoparticles fabricated by defect-free thermal imprinting. *J. Appl. Phys.* **111**, 07B509 (3pp) (2012).
156. Shore, D. *et al.* Electrodeposited Fe and Fe-Au nanowires as MRI contrast agents. *Chem. Commun.* **52**, 12634–12637 (2016).

157. Bañobre-López, M. *et al.* A colloidally stable water dispersion of Ni nanowires as an efficient: T 2-MRI contrast agent. *J. Mater. Chem. B* **5**, 3338–3347 (2017).
158. Burger, R. & Ducrée, J. Handling and analysis of cells and bioparticles on centrifugal microfluidic platforms. *Expert Rev. Mol. Diagn.* **12**, 407–421 (2012).
159. Ruffert, C. Magnetic bead-magic bullet. *Micromachines* **7**, (2016).
160. Microfluidics-Chp4.pdf.
161. Fu, A. *et al.* Protein-functionalized synthetic antiferromagnetic nanoparticles for biomolecule detection and magnetic manipulation. *Angew. Chemie - Int. Ed.* **48**, 1620–1624 (2009).
162. Van Roosbroeck, R. *et al.* Synthetic antiferromagnetic nanoparticles as potential contrast agents in MRI. *ACS Nano* **8**, 2269–2278 (2014).
163. Tudu, B., Tian, K. & Tiwari, A. Effect of Composition and Thickness on the Perpendicular Magnetic Anisotropy of (Co/Pd) Multilayers. *Sensors* **17**, 2743 (12pp) (2017).
164. Hellwig, O. *et al.* Coercivity tuning in Co/Pd multilayer based bit patterned media. *Appl. Phys. Lett.* **95**, 232505 (3pp) (2009).
165. Beaujour, J. M. L. *et al.* Ferromagnetic resonance study of sputtered Co|Ni multilayers. *Eur. Phys. J. B* **59**, 475–483 (2007).
166. Tudosa, I., Katine, J. A., Mangin, S. & Fullerton, E. E. Perpendicular spin-torque switching with a synthetic antiferromagnetic reference layer. *Appl. Phys. Lett.* **96**, (2010).
167. Lytvynenko, I., Deranlot, C., Andrieu, S. & Hauet, T. Magnetic tunnel junctions using Co/Ni multilayer electrodes with perpendicular magnetic anisotropy. *J. Appl. Phys.* **117**, (2015).
168. Mangin, S., Henry, Y., Ravelosona, D., Katine, J. A. & Fullerton, E. E. Reducing the critical current for spin-transfer switching of perpendicularly magnetized nanomagnets. *Appl. Phys. Lett.* **94**, 6–9 (2009).
169. Sbiaa, R., Ranjbar, M. & Åkerman, J. Domain structures and magnetization reversal in Co / Pd and CoFeB / Pd multilayers. *J. Appl. Phys.* **117**, 17C102 (2015).
170. Néel, L. Anisotropie magnétique superficielle et surstructures d'orientation. *J. Phys. le Radium* (1954) doi:10.1051/jphysrad:01954001504022500.

171. Müller, U. G. J. Flat Ferromagnetic, Epitaxial 48Ni/52Fe(111) Films of few Atomic Layers. *Phys. status solidi* **27**, 313–324 (1968).
172. Carcia, P. F., Meinhaldt, A. D. & Suna, A. Perpendicular magnetic anisotropy in Pd/Co thin film layered structures. *Appl. Phys. Lett.* **47**, 178–180 (1985).
173. Carcia, P. F. Perpendicular magnetic anisotropy in Pd/Co and Pt/Co thin-film layered structures. *J. Appl. Phys.* (1988) doi:10.1063/1.340404.
174. Den Broeder, F. J. A., Kuiper, D., Van De Mosselaer, A. P. & Hoving, W. Perpendicular magnetic anisotropy of Co-Au multilayers induced by interface sharpening. *Phys. Rev. Lett.* (1988) doi:10.1103/PhysRevLett.60.2769.
175. Xu, Y. B. *et al.* Magnetic and magneto-optical properties of Co Cu multilayers. *J. Magn. Magn. Mater.* **140**–**144**, 581–582 (1995).
176. Johnson, M. T., Bloemen, P. J. H., Den Broeder, F. J. A. & De Vries, J. J. Magnetic anisotropy in metallic multilayers. *Reports Prog. Phys.* (1996) doi:10.1088/0034-4885/59/11/002.
177. Daalderop, G. H. O., Kelly, P. J. & Den Broeder, F. J. A. Prediction and confirmation of perpendicular magnetic anisotropy in Co/Ni multilayers. *Phys. Rev. Lett.* **68**, 682–685 (1992).
178. Joo, H. W. *et al.* Enhancement of magnetoresistance in [Pd/Co]N//Cu/Co/[Pd/Co] N/FeMn spin valves. *J. Appl. Phys.* **99**, 8–11 (2006).
179. Tang, S. L., Carcia, P. F., Coulman, D. & McGhie, A. J. Scanning tunneling microscopy of Pt/Co multilayers on Pt buffer layers. *Appl. Phys. Lett.* **59**, 2898–2900 (1991).
180. Den Broeder, F. J. A., Kuiper, D., Donkersloot, H. C. & Hoving, W. A comparison of the magnetic anisotropy of [001] and [111] oriented Co/Pd Multilayers. *Appl. Phys. A Solids Surfaces* **49**, 507–512 (1989).
181. Tobari, K., Ohtake, M., Nagano, K. & Futamoto, M. Preparation and characterization of co/pd epitaxial multilayer films with different orientations. *Jpn. J. Appl. Phys.* **50**, 073001 (7pp) (2011).
182. Bandiera, S., Sousa, R. C., Rodmacq, B. & Dieny, B. Enhancement of perpendicular magnetic anisotropy through reduction of Co-Pt interdiffusion in (Co/Pt) multilayers. *Appl. Phys. Lett.* **100**, (2012).
183. Hashimoto, S., Ochiai, Y. & Aso, K. Perpendicular magnetic

anisotropy and magnetostriction of sputtered Co/Pd and Co/Pt multilayered films. *J. Appl. Phys.* **66**, 4909–4916 (1989).
184. Tang, M. H. *et al.* Interfacial exchange coupling and magnetization reversal in perpendicular [Co/Ni]N/TbCo composite structures. *Sci. Rep.* **5**, 1–7 (2015).
185. Song, H. S. *et al.* Observation of the intrinsic Gilbert damping constant in Co/Ni multilayers independent of the stack number with perpendicular anisotropy. *Appl. Phys. Lett.* **102**, (2013).
186. Wu, D., Chen, S., Zhang, Z., Ma, B. & Jin, Q. Y. Enhancement of perpendicular magnetic anisotropy in Co/Ni multilayers by in situ annealing the Ta/Cu under-layers. *Appl. Phys. Lett.* **103**, (2013).
187. Kurt, H., Venkatesan, M. & Coey, J. M. D. Enhanced perpendicular magnetic anisotropy in Co/Ni multilayers with a thin seed layer. *J. Appl. Phys.* **108**, (2010).
188. Tang, M. *et al.* Magnetic damping and perpendicular magnetic anisotropy in Pd-buffered [Co/Ni]5 and [Ni/Co]5 multilayers. *RSC Adv.* **7**, 5315–5321 (2017).
189. Miron, I. M. *et al.* Perpendicular switching of a single ferromagnetic layer induced by in-plane current injection. *Nature* **476**, 189–193 (2011).
190. Koopmans, B. *et al.* Field-free magnetization reversal by spin-Hall effect and exchange bias. *Nat. Commun.* **7**, 1–6 (2016).
191. Haazen, P. P. J. *et al.* Domain wall depinning governed by the spin Hall effect. *Nat. Mater.* **12**, 299–303 (2013).
192. Ohring. The Materials Science of Thin Films. *Acad. Press New York* (1992).
193. Al., C. et. Effect of sputter-deposition processes on the microstructure and magnetic properties of Pt/Co multilayers. *J. Magn. Magn. Mater.* **121**, (1993).
194. TAHMASEBI, T. Perpendicular magnetic anisotropy materials for magnetic random access memory applications. (2012).
195. Altissimo, M. E-beam lithography for micro-/nanofabrication. *Biomicrofluidics* **4**, (2010).
196. Franssila S., S. L. Reactive Ion Etching (RIE). (2008).
197. Pal, S., Polley, D., Mitra, R. K. & Barman, A. Ultrafast dynamics and THz oscillation in [Co/Pd]8 multilayers. *Solid State Commun.* **221**, 50–

54 (2015).
198. Pal, S. *et al.* Optically induced spin wave dynamics in [Co/Pd]8 antidot lattices with perpendicular magnetic anisotropy. *Appl. Phys. Lett.* **105**, (2014).
199. Yakushiji, K., Kubota, H., Fukushima, A. & Yuasa, S. Perpendicular magnetic tunnel junctions with strong antiferromagnetic interlayer exchange coupling at first oscillation peak. *Appl. Phys. Express* (2015) doi:10.7567/APEX.8.083003.
200. Arora, M., Hübner, R., Suess, D., Heinrich, B. & Girt, E. Origin of perpendicular magnetic anisotropy in Co/Ni multilayers. *Phys. Rev. B* **96**, 1–13 (2017).
201. Malinský, P., Slepička, P., Hnatowicz, V. & Švorčík, V. Early stages of growth of gold layers sputter deposited on glass and silicon substrates. *Nanoscale Res. Lett.* **7**, 1–7 (2012).
202. Donolato, M., Tollan, C., Porro, J. M., Berger, A. & Vavassori, P. Flexible and stretchable polymers with embedded magnetic nanostructures. *Adv. Mater.* **25**, 623–629 (2013).
203. Sbiaa, R. *et al.* Effect of film texture on magnetization reversal and switching field in continuous and patterned (Co/Pd) multilayers. *J. Appl. Phys.* **106**, (2009).
204. Ngo, D. T. *et al.* Perpendicular magnetic anisotropy and the magnetization process in CoFeB/Pd multilayer films. *J. Phys. D. Appl. Phys.* **47**, (2014).
205. Vemulkar, T., Mansell, R., Petit, D. C. M. C., Cowburn, R. P. & Lesniak, M. S. Highly tunable perpendicularly magnetized synthetic antiferromagnets for biotechnology applications. *Appl. Phys. Lett.* **107**, (2015).
206. Madou, M. J. Fundamentals of Microfabrication. *Fundam. Microfabr.* (2002) doi:10.1201/9781482274004.
207. Zhou, W., Apkarian, R., Wang, Z. L. & Joy, D. Fundamentals of scanning electron microscopy (SEM). in *Scanning Microscopy for Nanotechnology: Techniques and Applications* (2007). doi:10.1007/978-0-387-39620-0_1.
208. Wen, J. G. Transmission electron microscopy. in *Practical Materials Characterization* (2014). doi:10.1007/978-1-4614-9281-8_5.
209. Klug, H. & Alexander, L. X-ray Diffraction Procedures: For

Polycrystalline and Amorphous Materials, 2nd Edition. *Willey, New York, EUA* (1974).
210. Als-Nielsen, J. & McMorrow, D. Elements of modern X-ray physics. *Phys. Today* (2002) doi:10.1063/1.1472397.
211. Foner, S. Versatile and sensitive vibrating-sample magnetometer. *Rev. Sci. Instr.,* **30**, (1959).
212. The vibrating sample magnetometer: Experiences of a volunteer. *Appl., J. Phys.* **79**, (1996).
213. Foner, S. Versatile and sensitive vibrating-sample magnetometer. *Rev. Sci. Instrum.* (1959) doi:10.1063/1.1716679.
214. Clarke, J. & Braginski, A. H87412_v1.pdf. (2006).
215. Number, P. Quantum Design, MPMS ®SQUID VSM Brochure. (2010).
216. Pauw, L. J. Van der. A Method of Measuring Specific Resistivity and Hall Effect of Discs of Arbitrary Shape. *Philips Res. Reports* **13**, (1958).
217. Pandey, S. K. & Manivannan, A. A fully automated temperature-dependent resistance measurement setup using van der Pauw method. *Rev. Sci. Instrum.* **89**, 33906 (2018).
218. Bandiera, S., Sousa, R. C., Auffret, S., Rodmacq, B. & Dieny, B. Enhancement of perpendicular magnetic anisotropy thanks to Pt insertions in synthetic antiferromagnets. *Appl. Phys. Lett.* **101**, 072410 (4pp) (2012).
219. Lee, J. Bin *et al.* Thermally robust perpendicular Co/Pd-based synthetic antiferromagnetic coupling enabled by a W capping or buffer layer. *Sci. Rep.* **6**, 21324 (8pp) (2016).
220. Xiao, Y., Chen, S., Zhang, Z., Ma, B. & Jin, Q. Y. Magnetization reversal in antiferromagnetically coupled [Pt/CoFeB] N1 /Ru/[CoFeB/Pt] N2 structures with perpendicular anisotropy. *J. Appl. Phys.* **113**, 17A325 (3pp) (2013).
221. Hu, B. *et al.* Study of Co/Pd multilayers as a candidate material for next generation magnetic media. *J. Appl. Phys.* **109**, 1–5 (2011).
222. Desai, M., Misra, A. & Doyle, W. D. Effect of Interface Roughness on Exchange Coupling in Synthetic Antiferromagnetic Multilayers. *IEEE Trans. Magn.* **41**, 3151–3153 (2005).
223. Qiu, J. *et al.* Effect of roughness on perpendicular magnetic anisotropy in (Co90Fe10/Pt)n superlattices. *AIP Adv.* **6**, 056123 (1–

5) (2016).
224. Paul, A. Effect of interface roughness on magnetic multilayers of Fe/Tb and Fe/Cr. *J. Magn. Magn. Mater.* **240**, 497–500 (2017).
225. Chang, C. H. & Kryder, M. H. Effect of substrate roughness on microstructure, uniaxial anisotropy, and coercivity of Co/Pt multilayer thin films. *J. Appl. Phys.* **75**, 6864–6866 (1994).
226. Kim, J. H. & Shin, S. C. Interface roughness effects on the surface anisotropy in Co/Pt multilayer films. *J. Appl. Phys.* **80**, 3121–3123 (1996).
227. Chappert, C. & Bruno, P. Magnetic anisotropy in metallic ultrathin films and related experiments on cobalt films (invited). *J. Appl. Phys.* (1988) doi:10.1063/1.342243.
228. Shkurdoda, Y. O. *et al.* The giant magnetoresistance effect in Co/Cu/Co three-layer films. *J. Magn. Magn. Mater.* (2019) doi:10.1016/j.jmmm.2019.01.040.
229. Davies, J. E. *et al.* Reversal mode instability and magnetoresistance in perpendicular (Co/Pd)/Cu/(Co/Ni) pseudo-spin-valves. *Appl. Phys. Lett.* **103**, 022409 (2013).
230. Thiyagarajah, N. & Bae, S. Effects of engineered Cu spacer on the interlayer coupling and giant magnetoresistance behavior in Pd/[Pd/Co]2/Cu/ [Co/Pd]4 pseudo-spin-valves with perpendicular anisotropy. *J. Appl. Phys.* **104**, (2008).
231. ThiyagarajahI, N., LinI, L. & BaeI, S. Effects of NiFe/Co Insertion at the [Pd/Co] and Cu Interface on the Magnetic and GMR Properties in Perpendicularly Magnetized [Pd/Co]/Cu/[Co/Pd] Pseudo Spin-Valves. *IEEE Trans. Magn.* **46**, 968 (2010).
232. Publications, E. T., Tsymbal, E. Y. & Pettifor, D. G. Perspectives of Giant Magnetoresistance. (2001).
233. Kim, H. J. & Kim, D. E. Effect of surface roughness of top cover layer on the efficiency of dye-sensitized solar cell. *Sol. Energy* (2012) doi:10.1016/j.solener.2012.04.007.
234. Schaper, C. D. Patterned transfer of metallic thin film nanostructures by water-soluble polymer templates. *Nano Lett.* (2003) doi:10.1021/nl034412s.
235. Arnold, J. C. The effects of diffusion on environmental stress crack initiation in PMMA. *J. Mater. Sci.* (1998)

doi:10.1023/A:1004431920449.
236. Kwon, J. W., Yu, H. & Kim, E. S. Film transfer and bonding techniques for covering single-chip ejector array with microchannels and reservoirs. *J. Microelectromechanical Syst.* (2005) doi:10.1109/JMEMS.2005.859090.
237. Todeschini, M., Bastos, A., Jensen, F., Wagner, J. B. & Han, A. Influence of Ti and Cr Adhesion Layers on Ultrathin Au Films. *Appl. Mater. Interfaces* **9**, 37374–37385 (2017).
238. Leandro, L., Malureanu, R., Rozlosnik, N. & Lavrinenko, A. Ultrathin , Ultrasmooth Gold Layer on Dielectrics without the Use of Additional Metallic Adhesion Layers. *Appl. Mater. Interfaces* **7**, 5797−5802 (2015).
239. Lee, C. H. *et al.* Peel-and-Stick : Mechanism Study for Efficient Fabrication of Flexible/Transparent Thin-film Electronics. *Sci. Rep.* **3**, 2917 (1–6) (2013).
240. Tsymbal, E. Y. & Pettifor, D. G. Perspectives of Giant Magnetoresistance. in *Solid State Physics vol 56* (eds. Ehrenreich, H. & Spaepen, F.) 113–237 (New York: Academic, 2001).
241. Nakagawa, S. & Yoshikawa, H. Effect of roughness and continuity of Co layers to magnetic properties of Co/Pd multilayers. *J. Magn. Magn. Mater.* **287**, 193–198 (2005).
242. Oh, H. & Joo, S. Enhancement of Coercivity by Underlayer Control in Co/Pd and Co/Pt Multilayers. *IEEE Trans. Magn.* **32**, 4061–4063 (1996).
243. Al., M. A. et. Magnetic properties of Co/Ni multilayer structures for use in STT-RAM. *J. Phys. D. Appl. Phys.* **50**, (2017).
244. Hussain, R., Aakansha, Ravi, S. et al. Influence of substrate (Si and glass), Cu under-layer, in situ annealing of Ta/Cu and post-annealing on magnetic properties of [Co(0.3 nm)/Ni(0.6 nm)]4, 10 multilayer thin films. *J Mater Sci Mater Electron* **31**, (2020).
245. Lee-Hone, N. R. *et al.* Roughness-induced domain structure in perpendicular Co/Ni multilayers. *J. Magn. Magn. Mater.* **441**, 283–289 (2017).
246. Natarajarathinam, A. *et al.* Influence of capping layers on CoFeB anisotropy and damping. in *Journal of Applied Physics* (2012). doi:10.1063/1.4749412.

247. Gabor, M. S., Tiusan, C., Petrisor, T. & Petrisor, T. The influence of the capping layer on the perpendicular magnetic anisotropy in permalloy thin films. *IEEE Trans. Magn.* (2014) doi:10.1109/TMAG.2014.2320296.
248. Dieny, B. & Chshiev, M. Perpendicular magnetic anisotropy at transition metal/oxide interfaces and applications. *Rev. Mod. Phys.* **89**, (2017).
249. Mangin, S. *et al.* Current-induced magnetization reversal in nanopillars with perpendicular anisotropy. *Nat. Mater.* **5**, 210–215 (2006).
250. Fernández-Pacheco, A. *et al.* Magnetic State of Multilayered Synthetic Antiferromagnets during Soliton Nucleation and Propagation for Vertical Data Transfer. *Adv. Mater. Interfaces* **3**, 1–7 (2016).
251. Moritz, J., Garcia, F., Toussaint, J. C., Dieny, B. & Nozieres, J. P. Orange peel coupling in multilayers with perpendicular magnetic anisotropy : Application to (Co/Pt)-based exchange-biased spin-valves. *Europhys. Lett.* **65**, 123–129 (2004).
252. Kamata, Y., Kikitsu, A., Hieda, H., Sakurai, M. & Naito, K. Ar ion milling process for fabricating CoCrPt patterned media using a self-assembled PS- PMMA diblock copolymer mask. *J. Appl. Phys.* **95**, 6705–6707 (2015).
253. Rettner, C. T., Anders, S., Baglin, J. E. E., Thomson, T. & Terris, B. D. Characterization of the magnetic modification of Co/Pt multilayer films by He+, Ar+, and Ga+ and ion irradiation. *Appl. Phys. Lett.* **80**, 279 (2002).
254. Bhardwaj, R., Fang, X., Somasundaran, P. & Attinger, D. Self-assembly of colloidal particles from evaporating droplets: Role of DLVO interactions and proposition of a phase diagram. *Langmuir* **26**, 7833–7842 (2010).
255. Vogel, N., Goerres, S., Landfester, K. & Weiss, C. K. A convenient method to produce close- and non-close-packed monolayers using direct assembly at the air-water interface and subsequent plasma-induced size reduction. *Macromol. Chem. Phys.* **212**, 1719–1734 (2011).
256. Lotito, V. & Zambelli, T. Approaches to self-assembly of colloidal

monolayers: A guide for nanotechnologists. *Adv. Colloid Interface Sci.* **246**, 217–274 (2017).
257. von Freymann, G., Kitaev, V., Lotsch, B. V. & Ozin, G. A. Bottom-up assembly of photonic crystals. *Chem. Soc. Rev.* **42**, 2528–2554 (2013).
258. Galisteo-Lõpez, J. F. *et al.* Self-assembled photonic structures. *Adv. Mater.* **23**, 30–69 (2011).
259. Xia, Y., Gates, B., Yin, Y. & Lu, Y. Monodispersed colloidal spheres: Old materials with new applications. *Adv. Mater.* **12**, 693–713 (2000).
260. Cheung, C. L., Nikolić, R. J., Reinhardt, C. E. & Wang, T. F. Fabrication of nanopillars by nanosphere lithography. *Nanotechnology* **17**, 1339–1343 (2006).
261. Zhang, X. A., Elek, J. & Chang, C. H. Three-dimensional nanolithography using light scattering from colloidal particles. *ACS Nano* **7**, 6212–6218 (2013).
262. Wu, W., Katsnelson, A., Memis, O. G. & Mohseni, H. A deep sub-wavelength process for the formation of highly uniform arrays of nanoholes and nanopillars. *Nanotechnology* **18**, (2007).
263. Chen, Z., Taflove, A. & Backman, V. Photonic nanojet enhancement of backscattering of light by nanoparticles: a potential novel visible-light ultramicroscopy technique. *Opt. Express* **12**, 1214 (2004).
264. Cong, H., Yu, B., Tang, J., Li, Z. & Liua, X. Current status and future developments in preparation and application of colloidal crystals. *Chem. Soc. Rev.* **42**, 7774–7800 (2013).
265. Sowade, E., Blaudeck, T. & Baumann, R. R. Inkjet Printing of Colloidal Nanospheres: Engineering the Evaporation-Driven Self-Assembly Process to Form Defined Layer Morphologies. *Nanoscale Res. Lett.* **10**, 0–8 (2015).
266. Park, J. & Moon, J. Control of colloidal particle deposit patterns within picoliter droplets ejected by ink-jet printing. *Langmuir* **22**, 3506–3513 (2006).
267. Blättler, T. M., Senn, P., Textor, M., Vörös, J. & Reimhult, E. Microarray spotting of nanoparticles. *Colloids Surfaces A Physicochem. Eng. Asp.* **346**, 61–65 (2009).
268. Park, H. K., Yoon, S. W., Choi, D. Y. & Do, Y. R. Fabrication of wafer-

scale TiO2 nanobowl arrays via a scooping transfer of polystyrene nanospheres and atomic layer deposition for their application in photonic crystals. *J. Mater. Chem. C* **1**, 1732–1738 (2013).
269. Khanh, N. N. & Kyung, B. Y. Facile organization of colloidal particles into large, perfect one-and two-dimensional arrays by dry manual assembly on patterned substrates. *J. Am. Chem. Soc.* **131**, 14228–14230 (2009).
270. Bhardwaj, R., Fang, X. & Attinger, D. Pattern formation during the evaporation of a colloidal nanoliter drop: A numerical and experimental study. *New J. Phys.* **11**, (2009).
271. *Evaporative Self-Assembly of Ordered Complex Structures*. *Evaporative Self-Assembly of Ordered Complex Structures* (2012). doi:10.1142/9789814304696.
272. Oh, J. R., Moon, J. H., Yoon, S., Park, C. R. & Do, Y. R. Fabrication of wafer-scale polystyrene photonic crystal multilayers via the layer-by-layer scooping transfer technique. *J. Mater. Chem.* **21**, 14167–14172 (2011).
273. Retsch, M. *et al.* Fabrication of large-area, transferable colloidal monolayers utilizing self-assembly at the air/water interface. *Macromol. Chem. Phys.* (2009) doi:10.1002/macp.200800484.